1-1-2013

Osteon-Mimetic Nanocomposite Materials For Bone Regeneration

Ozan Karaman
University of South Carolina

OSTEON-MIMETIC NANOCOMPOSITE MATERIALS FOR BONE REGENERATION

by

Ozan Karaman

Bachelor of Science
Ege University, 2002

Master of Science
University of South Carolina, 2009

Submitted in Partial Fulfillment of the Requirements

For the Degree of Doctor of Philosophy in

Biomedical Engineering

College of Engineering and Computing

University of South Carolina

2013

Accepted by:

Esmaiel Jabbari, Major Professor

James O. Blanchette, Committee Member

Ehsan Jabbarzadeh, Committee Member

Yuh-Jin Chao, Committee Member

Lacy Ford, Vice Provost and Dean of Graduate Studies

DEDICATION

I dedicate this thesis to my lovely wife, Bedriye Karaman, who supported me with her big heart throughout my doctoral work. I would not be successful without your presence and encouragement.

ACKNOWLEDGEMENTS

First of all, I am deeply and sincerely grateful to my advisor, Professor Dr. Esmaiel Jabbari in the Biomedical and Chemical Engineering Department at the University of South Carolina. He helped me to broaden my knowledge and guided me throughout the whole research project. I wish to express my warm and sincere thanks to members of my research advisory committee, Biomedical Engineering Professor Dr. Ehsan Jabbarzadeh, James O. Blanchette and Mechanical Engineering Professor Dr. Yuh-Jin Chao. I also want to thank to my research group members Dr. Xuezhong He, Sina Moeinzadeh, Danial Barati, Samaneh Sarvestani as well as my dear friends Utku Kursat Ercan, Dr. Angel E Mercado, Lutfi Erden, Emrah Atilgan, Diego Padelford, Ahmad F. Ayna, and Suchit Sahai for their useful suggestions, support and encouragement during my PhD work. I also want to thank Biomedical Engineering secretary Carol Davis for her help during my study. I would like to express my sincere thanks to all of them. I would also want to thank all my family members for encouraging and supporting me to get my PhD degree thousands miles away from my country. Last, I want to express my sincere thanks to Turkish Educational Attache and Turkish Ministry of Education for the financial support and for taking care of all my problems during the period of my study. They never let me feel like I am alone in this big country. I am proud of being a Turkish citizen.

ABSTRACT

The limitations of large bone defect regeneration has brought the focus of Bone Tissue Engineering research on fabricating three-dimensional bone-mimetic grafts that could enhance osteogenesis and vascularization. Osteons composed of apatite-deposited aligned collagen nanofiber layers are the fundamental building blocks of cortical bone. In natural cortical bone, mineralization is mediated by extracellular matrix (ECM) proteins with amino acid sequences rich in glutamic acid. This dissertation is focused on the establishment of a novel biomimetic approach to engineer scaffolds for healing large bone defects.

In the first part, we investigated the effect of calcium phosphate (CaP) deposition on aligned surface-modified nanofibers (NF) with a glutamic acid peptide (GLU-NF) on osteogenic differentiation of marrow stromal cells (MSCs). In order to mimic the morphology of the bone ECM, the EEGGC peptide (GLU) with two glutamic acid residues was conjugated to a low molecular weight polylactide (PLA) macromer. The synthesized PLA-GLU polymer-peptide conjugate was blended with high molecular weight poly(lactide-co-glycolide) (PLGA) and electrospun to form GLU-NF. GLU-NF microsheets were incubated in a modified simulated body fluid (SBF) for nucleation and growth of CaP crystals on the fiber surface. To achieve a high CaP to fiber ratio, a layer-by-layer (LBL) approach was used to improve diffusion of calcium and phosphate ions inside the microsheets. Results demonstrate that surface modification of aligned synthetic

NF with EEGGC peptide significantly increased nucleation and growth of CaP crystals on the fibers, leading to increased mechanical properties and osteogenic differentiation of MSCs. In addition, CaP to fiber ratios as high as 200%, which lie between those of cancellous (160%) and cortical (310%) bone, were obtained with the LBL approach.

In the second part, the perforated CaP deposited NF microsheets were used to fabricate osteon-mimetic microtubes. The effect of the microtubular structure of CaP-deposited NF scaffolds on osteogenesis of MSCs and vascularization of endothelial progenitor cells (EPCs) and MSC co-cultures was investigated. It was found that microtubular scaffolds preferentially supported osteogenic and vasculogenic differentiation of MSCs and MSCs/EPCs as evidenced by elevated gene expression level of osteogenic and vasculogenic markers and enhanced calcium content, ALPase activity, and total collagen secretion. The osteon-mimetic scaffolds developed in this research are potentially useful as tissue engineered graft for regeneration of large bone defects.

TABLE OF CONTENTS

LIST OF FIGURES

.

CHAPTER 1

INTRODUCTION

Cranial, maxillofacial, oral fractures and large bone defects are currently being treated by using auto- and allografts. These techniques have limitations in the clinical usage such as immune response, donor-site morbidity, and lack of availability [1-3]. Therefore, the interest on tissue engineering applications for bone graft procedures has rapidly been growing. Among the 6 millions fractures occurring every year in the United States, there are more than 0.5 million skeletal injuries that require bone graft procedures [4]. Tissue engineering approach to bone graft application requires a cell supporting scaffold in order to maintain a 3- dimensional substrate for cells to function during the formation of bone tissue [5, 6]. The simple fractures in bone tissue can be treated by standard conservative or surgical therapy. However, in some cases, such as extended bone defects due to trauma or cancer resection bone grafting procedures are being performed with engineered biomimetic materials [7, 8].

Bone tissue engineering scaffolds needs to provide several criteria in order to be a successful candidate for bone graft procedures. An ideal scaffold should be completely integrated with the surrounding bone tissue, support sufficient mechanical strength, and function as a three dimensional framework for osteoprogenirator cells to fabricate bone

matrix. In order to integrate in bone defect site and provide adequate 3D structure, scaffolds should fulfill following requirements: (a) should mimic physical and chemical composition of the natural bone tissue, (b) should be biocompatible, (c) should be porous to allow bone tissue organization and vascular formation, (d) should provide appropriate surface chemistry and mechanical strength to support cellular attachment, proliferation and differentiation and (e) should degrade simultaneously with the newly grown bone tissue [9, 10].

The cortical bone composed of osteons that have microtubular structures with a central vascular channel inside for ensuring suitable nutrient/waste transport to the bone tissue [11]. The osteons are the structures form by laminated multilayers of apatite nucleated aligned collagen nanofibers (NF). Mineralization of collagen NF is a well-regulated process mediated by many extracellular matrix proteins, such as bone sialoprotein (BSP) and osteonectin (ON). These non-collagenous proteins contain a large amount of glutamic acid (Glu) residues, which act as frameworks for depositing apatite crystals on collagen fibers in nature bone [12-14]. The apatite crystals provide mechanical strength for bone formation [15], while the collagen fibers provide structural support and locations for cell adhesion and regulate cell functions such as cell adhesion, proliferation, differentiation, and mineralization [16].

In order to develop biologically functional engineered bone tissue, it is important to design scaffolds with micro- and nano-sized architecture similar to that of native bone. Nanofibers (NFs) produced by electrospinning (ES) have attracted much attention recently in tissue engineering applications [17]. Synthetic and natural polymers have been electrospun into NFs with diameters ranging from tens of nanometers to a few

micrometers. Due to their characteristics such as providing a large surface-to-volume ratio and mimicking the natural extracellular matrix structure (ECM) of bone tissue, NFs has been found to be a suitable scaffold for tissue engineering [18, 19]. However, poor mechanical properties and relatively 2-dimensional (2-D) formation of electrospun NFs limit their usage in bone tissue engineering applications. To overcome these limitations of electrospun nanofibers, 3-D ceramic/polymer composite materials have been identified for the preparation of bone tissue engineering scaffolds [20, 21]. The theory behind designing such scaffolds is based on the osteon-mimetic mechanism of the unique structure of HA/collagen in natural bone. Bone itself has a broad spectrum of mechanical properties, depending on its type, humidity, mineral content, density, porosity, and collagen fiber orientation [22]. The hierarchical organization between calcium phosphate crystals and collagen fibers allows bone to possess both excellent bioactivities and mechanical properties. Therefore, microtubular engineered 3-D biomaterials composed of apatite-nucleated aligned NF would potentially provide temporary structural support to the regenerating region, initiate osteogenic and vasculogenic differentiation, and degrade simultaneously with the production of bone ECM. Consequently, the biomimetic scaffolds aims to mimic the 3-D hydroxyapatite/collagen nanofibers structure of natural bone.

CHAPTER 2

BACKGROUND AND LITERATURE REVIEW

2.1 BONE TISSUE

Tissue is a group of cells which have similar functions in the body. Human body consists of approximately 200 different types of cells which organized into four main tissues: connective, epithelial, nervous and muscle tissues. Bones are composed of connective tissues, which have extracellular matrix (ECM) in addition to the cells. Most connective tissues have nerves and blood supply and consist of scattered cells submerged in the ECM. The matrix contains structural networks and solutions of non-living intracellular material. The matrix consists of different amount of fibers and ground substances, which identify the character of the matrix. Bones are considered as supporting connective tissues, which have a less diverse cell population compared to other connective tissues. Bones are composed of a composite fibrous network collagen encased within a hard matrix of calcium/phosphate. Mature bone matrix consist of approximately 35% organic (collagen fibers, glycoproteins and proteoglycans) and 65% inorganic material (hydroxyapatite, calcium carbonate and magnesium hydroxide). The organic materials and mineral salts give bone its major characteristic function. Collagen is responsible for the flexibility and resistance to being stretch, whereas the mineral salts give the matrix compression strength. For instance, if all the mineral salts are removed

from the bone matrix, bone becomes overflexible. On the contrary, if the collagen removed from the bone, the bone will be more breakable [23-26].

Connective tissue originates from mesenchymal cells. Mesenchymal stem cells (MSCs) have ability to diferentiate into more specialized cell arrays. Osteoprogenitor cells are basic stem cells of bone structure. They have ability to become osteoblasts or chondroplasts. Osteoprogenitor cells differentiate to osteoblasts if they are located close to capillaries where oxygen concentration is high; otherwise they become chondroplasts where they are far from capillaries. Bone cells can be categorized in four parts which have all different functions and origins: osteoblasts, osteocytes, osteoclasts, and osteoprogenitors. Osteoprogenitors are undifferentiated cells which will undergo mitosis and develop into osteoblasts. They are usually found on the surfaces of bones and bone cavities containing blood vessels and bone marrow. Osteoblasts grow from osteoprogenitor cells located in the periosteum and the bone marrow. Osteoprogenitors are induced to differentiate under the influence of growth factors, in particular the bone morphogenetic proteins (BMPs). Osteoblasts have a large endoplasmic reticulum and numerous ribosomes. They are derived from osteoprogenitor cells and produce collagen and proteoglycans, which are stored by the Golgi apparatus and released from the cell**.** The formation of bones by osteoblasts is called ossification or osteogenesis. The interaction between osteoblasts forms the bone extracellular matrix (ECM) which surrounds the cells. After an osteoblast starts to be surrounded by bone ECM, it becomes an octeocyte. The majority of the bone cells are osteocytes, which derive from osteoblasts, are found embedded in the bone matrix. Lacunae are the spaces that are occupied by the osteocyte cell bodies and canaliculi are the spaces occupied by the

osteocyte cell processes. Osteocytes do not secrete bone matrix. They only maintain the matrix surrounding them in good condition. Osteoclasts are large cells with more than one nuclei. They are responsible for resorption of bone. Osteoclasts produce some enzymes which help breaking down the bone ECM. This function of the osteoclasts is important in the development, growth, maintenance and repair of bone [23, 24, 26, 27].

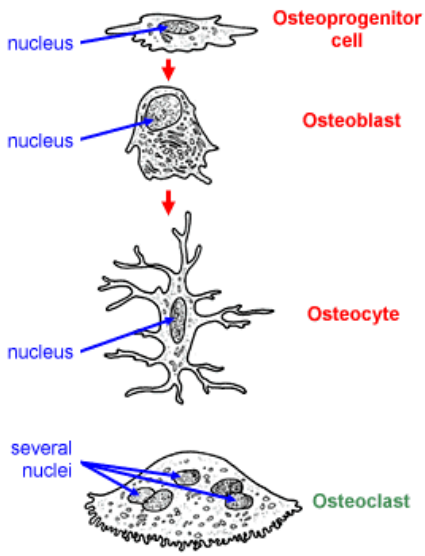

Figure 2.1 Bone Cells [24]

2.2 BONE STRUCTURE AND FUNCTIONS

Bone tissues consist of osteocytes scattered in a hard calcified matrix. Each bone in the skeleton has two different forms of osteon tissue: compact bone and spongy bone. Compact bone is relatively solid; however, spongy bone has a smooth structure. Compact bone consists of closely packed microscopic cylindrical structures called osteons. The matrix and osteocytes of the osteon are laid down in concentric rings around a central (Haversian) canal that contains blood vessels and nerves. Fine cellular extensions connect osteocytes within an osteon to each other and to the Haversian canal. Nutrients and

wastes are exchanged between the osteocytes and the blood vessels through these cellular extensions. Blood vessels which run through the central canals are connected to the blood vessels in the periosteum that surrounds the bone by perforating canals called Volkmann's canals. Compact bone tissues make up the shaft of long bones and are located at the outside surface of other bones. Spongy bone consists of an irregular latticework of thin plates of bone called trabeculae. Blood vessels and red marrow, which produces blood cells, fill the spaces between trabeculae. These blood vessels are connected to blood vessels found in the Volkmann's and Haversian canals. In contrast to compact bone, spongy bone does not contain osteons and is found inside the bones. Compact bones are located on the surface of a bone to protect the bone structure, whereas spongy bones are located inner part of the bone. Bones are the framework for supporting the attachment of muscles and other tissues. Besides, bone protect internal organs from outside effects such as the skull protecting the brain or the ribs protecting the heart and lungs. Bones work together with skeletal muscles, tendons, ligaments and joints for body movement. The red marrow which is within the medullar cavity of long bones produces red blood cells. Bones are storage of several essential minerals such as calcium and phosphorus, and help kidney for arranging acid-base balance by absorbing or releasing alkaline salts [23, 26, 27].

2.3 BONE TYPES

There are five types of bones in the human body: long, short, flat, irregular, sesamoid, and sutural bones. Long bones are much greater in length than width such as limbs, fingers and toes. Long bones consist of a shaft (diaphysis) and two extended ends (epiphysis). The diaphysis is made out of compact tissue surrounding a central cavity

which is called medullar cavity. Epiphysis contains spongy bones and red marrow and it is covered by thin layer of compact tissue. Hyaline cartilage overlaps the epiphysis on its outer surface. The periosteum covers the outside of the long bone. Short bones have a structure similar to long bones. Examples of short bones include carpal bones and tarsal bones. Flat bones, which form the roof of the skull, the sternum, the ribs and the scapula, have thin, severally parallel surfaces. Protection of underlying soft tissues and providing the surface area for muscles attachment are basic functions of flat bones. Irregular bones have complex shapes. They are located at several skull and spinal vertebra. Sesamoid bones are small, flat, and shaped like sesame seeds. They are located near joints on the knees, the hands and the feet. Sutural bones are small, flat, irregularly shaped bones between the flat bones of the skull [23, 26].

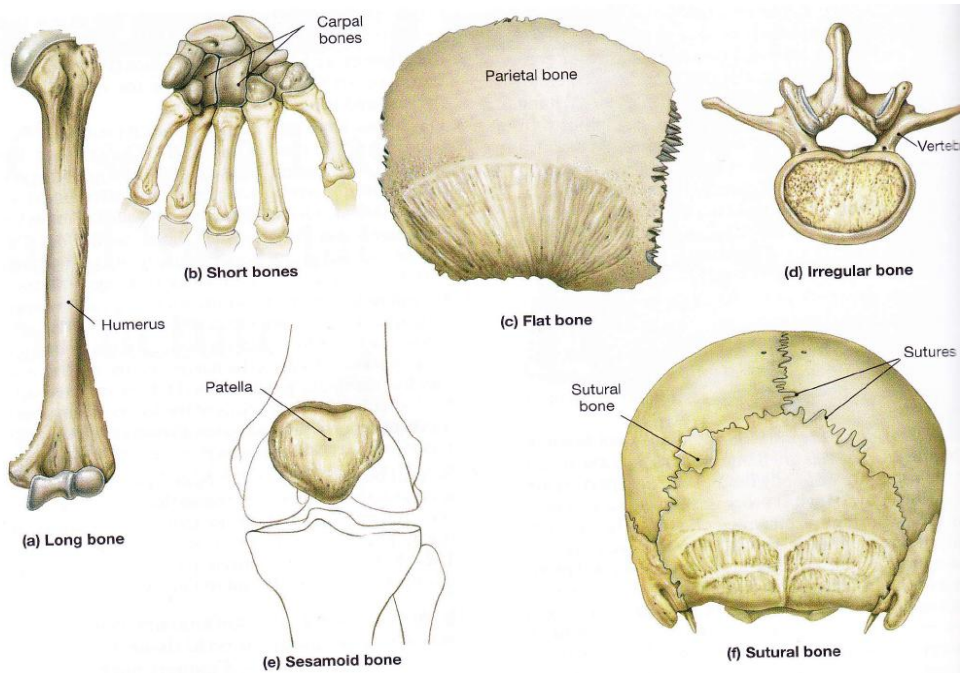

Figure 2.2 Classification of Bones [23].

2.4 BONE DEVELOPMENT AND GROWTH

The size and proportions of our body are determined by the growth of the skeleton. After 6 weeks from fertilization, the bone skeleton starts forming. Bones keep growing through adolescence until age 25. Bone might develop from mesenchymal cells or by the replacement of cartilage. Ossification, which refers to the formation of bone, is the process of replacement from other tissues to bone tissue. Calcification is the deposition of the calcium salts. There are two forms of ossification: intramembranous and endochondral ossification. In intramembranous ossification, mesenchymal cells and fibrous connective tissue are the major source of bone tissue. In endochondral ossification, bone differentiates from existing cartilage [23, 26].

Intramembranous ossification starts when osteoblasts differentiate within a mesenchymal or fibrous connective tissue and occurs in the deeper layers of the dermis. Embryonic mesenchyme condenses around the developing brain to form a membrane of connective tissue with oriented, delicate fibers. Osteoprogenitor cells differentiate to osteoblasts, which produce bone matrix to surround the aligned collagen fibers. After that process, many trabeculae of woven bone are formed. The rest of osteoblasts gather close to the surface of the trabeculae and produce larger trabeculae. Trabeculae join together to be able to develop cancellous bone. The cells, which are located in the inner part of cancellous bone, develop red bone marrow. After cancellous bone is developed, the cells that surround the outer part of the bone form periosteum. Osteoblasts develop the periosteum and bone matrix to form the outer surface of the compact bone. Endochondral ossification begins with the formation of hyaline cartilage at the end of the fourth week of development. The mesenchymal cells differentiate to chondroplasts. Chondroplasts

develops a hyaline cartilage having the original shape of the bone. After chondroplasts are surrounded with cartilage matrix they become chondrocytes, which is surrounded with perichondrium. After blood vessels are connected to perichondrium, osteoprogenitor cells become osteoblasts and begin producing the bone structure. As osteoblasts keep producing bones, perichondrium turns out to periosteum [23, 26, 27].

2.5 BONE SUBSTITUTES

Bone graft substitutes are required to repair the injuries that are extremely hard for the body to cure by using the bone repair process. Approximately 500.000 bone grafts operations are made annually in the United States. There are basically three major methods of bone substitute usage in medical applications. Autografting, which comprises 58% of the current bone substitutes, is a graft made of bone from the patient's own body. An example for one of the most commonly performed bone autograft is being used in spinal fusion. In a fusion procedure, bone graft from the patient's hip is implanted in disc spaces between spinal vertebrae or along the back of the spine. The grafted bone fuses the vertebrae together over several months. Allografting, which represents about 34% of the current bone substitutes, contains harvesting and processing bone from a cadaver then transplanting it to the patient. Allogenic implants are acellular and are less successful than autografts for immunogenicity and the absence of viable cells that become osteoblasts. Another disadvantage of allografting is high risk of transmitted diseases. Man-made materials such as metals, plastics, and ceramics represent approximately 8% of bone substitutes. These materials, however, are subject to fatigue, fracture, toxicity, and wear, and do not remodel with time, such as a metal bone implant, which cannot grow with the patient and it cannot change shape in response to the loads placed upon the

implant. For all these reasons, there is an increasing need for alternative bone substitutes and better wound healing therapies. The numerous research have been done on engineering natural or synthetic scaffolds to make them suitable for bone regeneration applications. The main idea of bone tissue engineering is to develop similar structural and functional properties of the bone ECM [26-28].

2.6 BONE TISSUE ENGINEERING

Tissue Engineering is an interdisciplinary field that combines the principles of biology and engineering to mimic human tissues. The general requirements for developed scaffolds are easy handling and applying, being readily adherent, having appropriate mechanical and physical properties, being non-toxic, non-antigenic, sterile, osteoconductive, cost effective, and undergoing controlled degradation. Tissue engineering techniques involve mimicking the natural bone structure by placing the cells and growth factors in synthetic scaffolds that act as temporary bone ECM [26, 28]. The major function of a degradable scaffold is to support the transplanted tissues. There are many kinds of biomaterials being used for bone tissue engineering applications such as natural and synthetic polymers, ceramics, and composites [26, 29].

2.7 BIOMATERIALS FOR SCAFFOLD FABRICATION

Natural and synthetic materials have been investigated as a matrix for biomimetic scaffold fabrication in bone tissue engineering [30]. Natural materials provide a conductive matrix for cell migration and adhesion since they include the biological cues but they are lack of sufficient mechanical strength to prevent soft tissue compression [31]. Synthetic materials could be designed with defined physical and mechanical properties, but they lack bioactive cues to support cell−matrix interactions

required for adhesion, proliferation, and differentiation. Therefore, an ideal scaffold must provide the optimum structural parameters, conductivity to the cellular activities; these include cell penetration and migration into the scaffold, cell attachment onto the scaffold substrate, cell spreading and proliferation.

One of the first considerations when designing a scaffold for bone tissue engineering is the choice of material [32, 33]. In order to mimic the mineralized nanofibrous structure of natural bone tissue, two main material types; natural polymers and synthetic polymers, and their composite structures with hydroxyapatite have been successfully investigated for biomimetic scaffold fabrication.

2.8 NATURAL POLYMERS

Natural polymers, which commonly derived from protein or carbohydrate polymers, can be considered as the first biodegradable scaffolds used clinically in bone tissue engineering applications [34]. These polymers have a number of advantages such as outstanding biocompatibility, relative abundance, and biodegradability. However, the batch-to-batch variations in the structure, insufficient mechanical strength and risk of immunogenic effect when implanted require using natural polymers with some modifications. Here, we focus on most widely used natural polymers; collagens, chitosan and gelatin, which can be fabricated in fibrous structure and their composite structures by incorporating calcium phosphate crystal for bone tissue engineering applications [35].

Since collagen is the major protein in bone extracellular matrix, it is considered by many researchers as an ideal scaffold for tissue engineering applications [35]. Twenty-seven types of collagens have been identified so far, but collagen type I is the

most investigated one since it is the most abundant collagen in bone tissue [36]. The functions of collagen are providing support to connective tissues such as skin, tendons, bones, cartilage, blood vessels, and ligaments [37, 38], transduces essential signals for the regulation of cell anchorage, migration, proliferation, differentiation, and survival [39]. Bone tissue engineering scaffolds requires high mechanical strength for in vivo applications of the scaffolds. Therefore, scaffolds for bone tissue engineering require hardening of a collagen biomaterial by mineralization [22, 40] or combining with hydroxyapatite crystals [41, 42]. Recently, a broad range of bone tissue engineering products based on collagen scaffolds have been developed. For example, Xiao et al. fabricated three-dimensional type I collagen based scaffolds and seeded with osteoprogenitor cells and implanted into critical-size bone defects in skulls of immunodeficient (SCID) mice. They have shown new bone formation at the critical defect site after 28 days [43]. Chan et al. developed a collagen microencapsulation technology by encapsulating bone marrow–derived mesenchymal stem cells (MSCs) in a biomimetic collagen fiber meshwork and investigate the differentiation capacity of the MSCs. The differentiation of MSCs was confirmed with significantly increased calcium content and alkaline phosphatase activity in the collagen microspheres [44]. In addition, there are some developed collagen based scaffolds in the market that have been used as bone grafts. For example, a mixture of porous hydroxylapatite and tricalcium phosphate and collagen I was fabricated by Angiotech Pharmaceuticals, Inc. and have been used clinically for healing large bone defects. Furthermore, hydroxyapatite coated collagen fibers developed by DePuy Orthopaedics has been approved for clinical use as a bone graft substitute in spinal fusions [39].

Chitosan the second most abundant natural polymer is produced from chitin, which is a natural polysaccharide found in crab, shrimp, lobster, coral, jellyfish, butterfly, ladybug, mushroom and fungi [45]. Chitosan can be easily modified into various forms such as films, fibers, and more complex shapes for bone tissue engineering applications [46]. However, chitosan based scaffold by itself cannot support load bearing bone grafts. Developing composite matrix by combining calcium phosphate crystals with chitosan based scaffolds improve the mechanical properties of chitosan and make it suitable for bone tissue engineering applications [46, 47]. For example, Zhang et al. developd a novel biomimetic nanocomposite nanofibers of hydroxyapatite/chitosan (HAp/CTS) and seeded with human fetal osteoblast (hFOB) cells for up to 15 days. The results demonstrated that incorporation of HAp nanoparticles into chitosan nanofibrous scaffolds shows significant higher mineral deposition compared to pure electrospun CTS scaffolds [48]. Thein-Han et al. and Teng et al. prepared biomimetic CTS/HA composite membranes and seeded with pre-osteoblasts (MC 3T3-E1) cells. Cell culture experiments demonstrated that CTS/HA composite scaffolds are potential candidate materials for bone regeneration [49, 50].

Gelatin is a natural polymer that is derived from collagen by hydrolysis, and is commonly used for pharmaceutical and tissue engineering applications because of its biodegradability and biocompatibility in physiological environments [51, 52]. Since gelatin is a denatured format of collagen, it has relatively low antigenicity compared to other natural polymers [38]. Gelatin-based composites with incorporation of calcium phosphate crystals, therefore, provide an alternative scaffold for bone tissue engineering applications. For example, Takahashi et al. fabricated biodegradable gelatin sponges

incorporating β-tricalcium phosphate (βTCP) (gelatin-βTCP) and investigated the in vitro osteogenic differentiation of MSCs isolated from the rat bone marrow. The alkaline phosphatase activity and osteocalcin content results demonstrated that osteogenic differentiation of MSCs occured when seeded on gelatin-βTCP sponges [53]. Xia et al. investigated the potential application of bone marrow stromal cells (BMSCs) and an injectable sodium alginate/ gelatin scaffold for bone tissue engineering (BTE). The phenotype of osteogenic BMSCs was examined by mineralized nodules formation and type I collagen expression. They showed that sodium alginate/ gelatin scaffold promoted the bone formation and bone healing when implanted in the rabbit calvarial critical-sized defect [54]. He et al. fabricated three-dimensional mineralized (3-D) porous gelatin scaffolds and seeded with MC3T3-E1 pre-osteoblastic cells. The results inticated that the MC3T3-E1 cells grown on the mineralized gelatin scaffolds showed higher levels of ALP activity and osteocalcin expression than that on the neat gelatin scaffold [55]. Liu et al. fabricated nanofibrous gelatin/apatite (NF-gelatin/apatite) composite and seeded with pre-soteoblastic cells. They were demonstrated that the expression of bone sialoprotein and osteocalcin in the osteoblast–(NF-gelatin/apatite composite) constructs was about 5 times and 2 times higher than in the neat gelatin constructs after four weeks of cell culture [56]. Besides the direct implantation into bone defect site, gelatin has also been used as controlled-release devices of basic fibroblast growth factor (bFGF), transforming growth factor-h1 (TGF-β1), bone morphogeneticprotein-2 (BMP-2) growth factors which have specific function on enhancing bone formation [57, 58].

Overall, as the previous studies indicated the disadvantage of using insufficient mechanical strength natural polymers could be improved by combining with calcium-

phosphate (CaP) based crystals and make them suitable for bone tissue engineering applications.

2.9 SYNTHETIC POLYMERS

Synthetic polymers based scaffolds have some advantages compared to natural polymers such as reproducibility, unlimited supply, relative lack of immunogenic effect, and tunable properties such as degradation rates and mechanical strength. Synthetic polymers used for bone regeneration include poly(lactic acid) (PLA), poly(glycolic acid) (PGA), poly(lactic-co-glycolic) acid (PLGA), polypropylene fumarate (PPF), and the polyhydroxyalkanoates (PHAs) [59]. Combining polymers with hydroxyapatite creates biomimetic scaffolds that enhance bone tissue formation.

Poly lactic acid (PLA) is a biodegradable polyester synthesized by poly-condensation of lactic acid, and amonomeric precursor that can be obtained from renewable resources. Lactic acid is a chiral molecule available in the L and D stereoisomer forms. Since L-lactic acid occurs in the metabolism of all animals and microorganism, it's degradation products are completely non-toxic [60, 61]. PLA based scaffolds are biodegradabile, biocompatibile, and have suitable mechanical properties, and ability to be dissolved in common solvents for processing. Due to these features, PLA has been successfully used for bone tissue engineering applications [61]. For example, Liao et al. fabricated a composite scaffold consisting of nano-HA/collagen and seeded with osteoblasts isolated from rat. Then, the composite scaffold was implanted into critical size defect in rabbit. The results showed that osteoblasts adhered, spread, and proliferated throughout the pores of the scaffold within a week and the implanted composite was partially substituted by new bone tissue after 12 weeks [62]. Our group

also produced random and aligned PLA nanofibers via electrospinning technique and seeded with rat MSCs. We investigate the effect of fiber alignment on osteogenic differentiation of MSCs. The results indicated that BMS cells aligned in the direction of PLLA fibers to form long cell extensions, and fiber orientation affected the extent of mineralization, but it had no effect on cell proliferation or mRNA expression of osteogenic markers.

Poly (glycolic acid) (PGA) and poly (lactic acid) (PLA) are biodegradable synthetic polymers, which can react to form the copolymer poly (lactic-co-glycolic acid) (PLGA). The main advantage of PLGA is that the ester bonds that make up the backbone of the polymer can be hydrolyzed, causing the scaffold to degrade into metabolite nontoxic by-products. These by-products can be absorbed by the body and may cause pH changes around the implantation site. In addition, the degradation profile of PLGA can be controlled by changing the ratio of PGA to PLA in the scaffold [63]. These feature make PLGA based scaffolds a good candidate for bone tissue engineering applications. For example, Lao et al. fabricated PLGA/HA nanofibers composite by electrospinning and seeded with neonatal mouse calvaria-derived MC3T3-E1 osteoblasts. The results showed that composite scaffolds could support cell adhesion and proliferation [64].

Polycaprolactone (PCL) has low melting point of around 60°C and a glass transition temperature of about −60°C. PCL can be degraded by hydrolysis of its ester linkages in physiological conditions and has high mechanical strength compared to most of the synthetic polymers. Due to these features, PCL has been widely used in bone tissue engineering applications [65]. For example, Shin et al. produced highly porous, degradable PCL scaffold by electrospinning, seeded with rat MSCs, and cultured in a

rotating bioreactor for 4 weeks. The scaffold then implanted into the omenta of rats for 4 weeks. The results showed bone like tissue formation on the implant site [66]. In another study, Venugopol et al. fabricated (PCL/nHA/Col) biocomposite nanofibrous scaffolds to provide mechanical support and seeded with human fetal osteoblasts (hFOB). They indicated that the nanoscale biocomposite scaffold supported hFOB adhesion, migration, proliferation and mineralization to form a bone tissue for the regeneration of bone defects [67].

2.10 CALCIUM PHOSPHATE CERAMICS

Calcium phosphate (CaP) ceramics have also been used to synthesize biomimetic scaffolds for bone tissue engineering. The main purpose to use CaP ceramic is that CaP is abundantly found in bone tissue and it shows biocompatibility, and osteoconductivity. However, the major drawbacks for using CaP ceramics are low mechanical stability and the inability to control the pore size and chemical composition. The most widely studied CaP ceramics are tricalcium phosphate (TCP), hydroxyapatite (HA, $Ca10(PO_4)6(OH)_2$), and tetracalcium phosphate [68]. Although several studies have shown bone regeneration with CaP based scaffold implantation, the feature of being highly brittle prevents using CaP ceramics for bone defects [21, 69]. In order to overcome these drawbacks of using CaP ceramics by itself as a scaffold, combination of natural or synthetic polymers with CaP ceramics have been used for bone tissue engineering applications.

2.11 FABRICATION TECHNIQUES OF BIOMIMETIC FIBROUS SCAFFOLDS

In order to mimic the three-dimensional structure of natural bone tissue, biomimetic scaffolds must facilitate the cell distribution and guide their growth into

three-dimensional space. Collagen nanofibers in natural bone tissue have fibrous structure with diameter range of from 50 to 500 nm [70, 71]. The ideal biomimetic scaffolding techniques should allow fabricating the nanofibrous structure of collagen nanofibers in natural bone. Several methods have been developed to fabricate nanofibers, such as self-assembly [72], phase separation [73], and electrospinning [74, 75].

Self assembly is the organization of the molecule into an ordered structure required for specific function (Zhang, 2003). The structure of the self assembled molecules are maintained by non-covalent bonds such as hydrogen bonds, ionic bonds, and hydrophobic interactions [76] . Peptides and proteins can be self assembled to form nanofibrous well-defined functional structures [77, 78]. The advantage of the self aseembly technique over phase separation and electrospinning is producing much smaller nanofibers. However, the drawbacks of low mechanical strength and limited macroporous structure of self assembled peptides prevents them to be ideal biomimetic scaffold for bone tissue engineering applications.

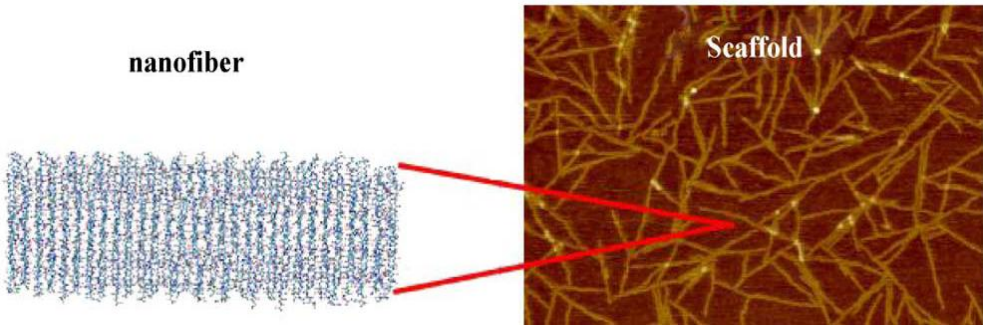

Figure 2.3 Molecular models of self-assembling peptides [79]

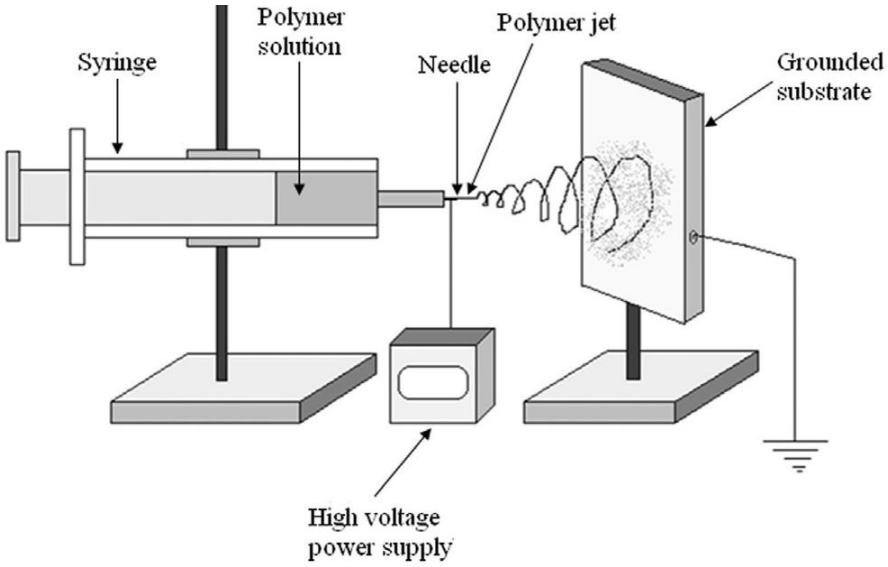

Figure 2.4 Schematic of the electrospinning process [80]

The electrospinning technique for the scaffold fabrication uses the electrostatic force for the production of polymeric fiber ranging from nanoscale to microscale. In the electrospinning process, the use of a high voltage electrostatic field to charge the surface of a polymer solution droplet induces the ejection of a liquid jet through a spinneret. Applied electrical field between a droplet of a polymer solution, which is held in the syringe, and a grounded target makes the polymer solution to be ejected when the applied electric field overcomes the surface tension of the polymer solution. During the ejection, solvent in the polymer solution evaporates, and electrospun nanofibers are collected on the grounded collector [80-85]. System and process parameters are the two sets of parameters that affect the process of electrospinning. System parameters such as polymer molecular weight and distribution determine the rate of nanofiber degredation. Polymer solution properties such as viscosity, surface tension, and conductivity, determine the nanofiber diameter. Process parameters such as orifice diameter, flow rate of polymer, and electric potential also have significant influence on fiber diameter. Process

parameters such as distance between syringe and metal collector determine the extent of evaporation of solvent from the nanofibers and deposition on the collector [80, 85, 86]. Electrospinning has been used to produce nanofibers (NFs) [17] from natural biopolymers, like collagen and chitosan, or synthetic polymers such as poly(L-lactide) (PLLA) and poly(ε-caprolactone) (PCL) [78, 87-89]. Among these fabrication techniques of fibrous biomimetic scaffolds, electrospinning has been regarded as the most promising approach to fabricate nanofibers with adjustable fiber diameter from nanometer to micrometer [87].The advantages of this technique is that it can produce nanofibers that can provide high surface-area-to-volume ratio, similar morphology to the collagen nanofiber in natural bone, degradability, biocompatibility, and high mechanical strength for cell adhesion, proliferation and differentiation [90, 91]. These characteristics are favorable for better cellular growth and tissue organization for *in vitro* and *in vivo* bone tissue engineering applications [18, 92].

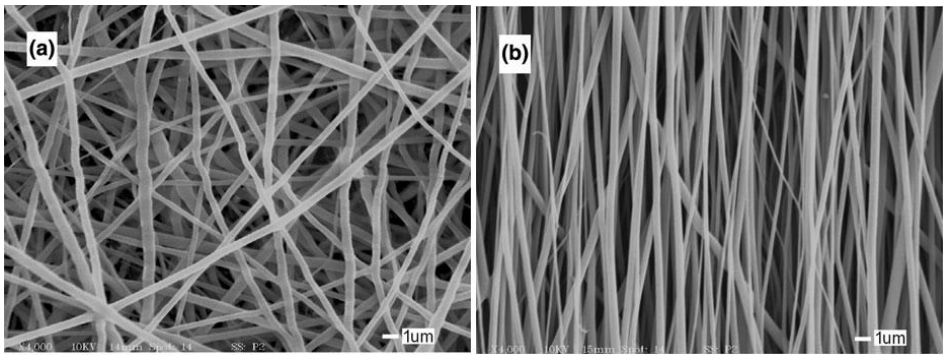

Figure 2.5 SEM micrographs of (a) random and (b) aligned fibers, electrospun from 9.0 wt % PLLA in HFIP solvent. The diameter and rotation speed of the collecting wheel were 20 cm and 1200 rpm, respectively [93].

Phase separation technique for fibrous scaffolds fabrication relays on temperature change that separates the polymeric solution in two phases, one having low

polymer concentration (polymer lean phase) and other having the high polymer concentration (polymer rich phase) [94]. Phase separation process for nanofiber formation consists of five steps: polymer dissolution, phase separation and gelation, solvent extraction, freezing, and freeze-drying under vacuum [70]. The fiber network formation depends on the solvent of the polymer solution and the gelation temperature. The fibers formed in this manner have diameters ranging from 50–500 nm, and have a porosity in excess of 98% [56, 70]. The advantage of the phase separation technique is that it can be combined with other processing techniques such as particulate leaching to fabricate biomimetic scaffolds with well-defined pore morphologies [95].

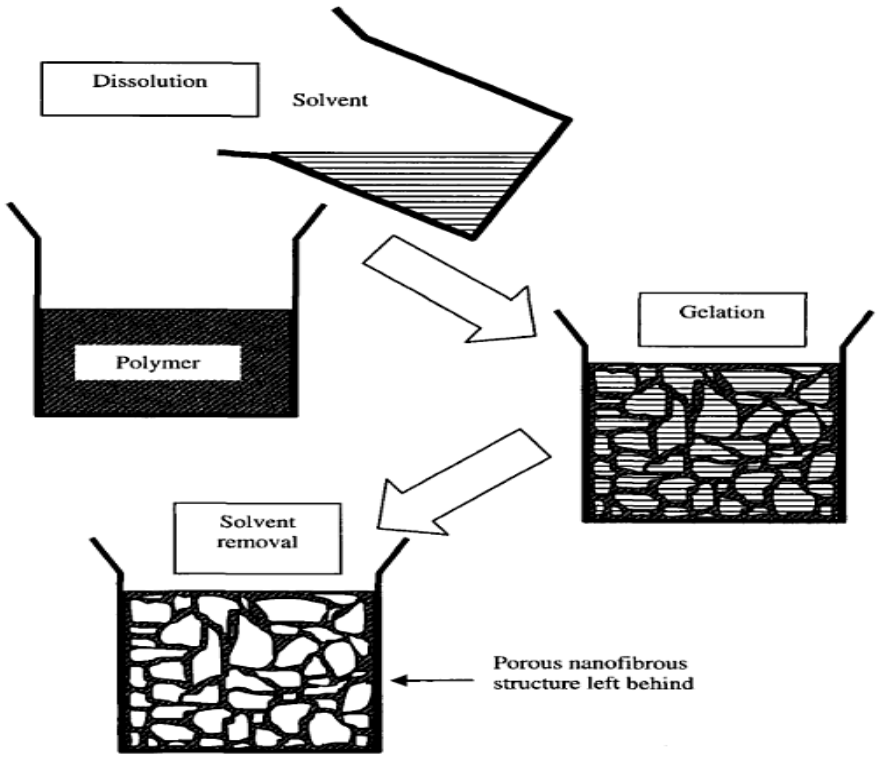

Figure 2.6 Schematics of phase separation for obtaining nanofibers structure [96].

2.12 DESIGNING OF BIOMIMETIC SCAFFOLDS

The limitation of using synthetic biodegradable polymers as biomimetic scaffolds is that they cannot promote cell adhesion, proliferation, and differentiation as much as natural polymer because they often lack of biological cues. Although growing hydroxyapatite on synthetic scaffold improves osteoconductivity and cellular interactions, further surface modifications should be done to completely overcome the problem of limited cell recognition points. For example, Langer et al. synthesized poly(L-lactic acid-co-L-lysine) and conjugated Arg-Gly-Asp (RGD) peptide to the lysine residue of the copolymer to enhance cell adhesion. The RGD peptides of ECM proteins interact with MSCs through integrin surface receptors to facilitate cell spreading and adhesion. The results demonstrated that cell spreading mean area was significantly increased on scaffolds with RGD peptide [97, 98]. Hu et al. fabricated RGD peptide attached porous poly(lactic acid) (PLA) scaffolds and seeded with osteogenic precursor cells to investigate the RGD peptide attachment on cell proliferation and differentiation. The results of this study indicated that RGD peptide attachment to the surface of PLA polymer scaffolds enhances cell attachment and differentiation [99]. Our group recently produced RGD and bone morhogenic peptide-2 (BMP-2) grafeted Poly (lactide-*co*-ethylene oxide-*co*-fumarate) (PLEOF) based hydrogels and investigate the effects of RGD and BMP peptide on osteogenic differentiation and mineralization of MSCs. Our results demonstrated that RGD and BMP peptides, grafted to a hydrogel substrate, act synergistically to enhance osteogenic differentiation and mineralization of MSCs [100].

The function of calcium phosphate crystals (mainly hydroxyapatite) in a composite scaffold is providing good osteoconductivity while the fibrous structure of natural or synthetic polymer supports design flexibility to achieve the high porosity and high surface area for cell survival and differentiation [56, 70]. Zhang et al. and Ma et al. developed highly porous poly(L-lactic acid) (PLLA) and PLLA/hydroxyapatite (HAP) composite scaffolds with a thermally induced phase separation technique and seeded with osteoblastic cells. The proliferation of osteogenic cells and expression of bone sialoprotein and osteocalcin were significantly higher in the PLLA/HAP composite scaffold than in the PLLA scaffolds [98, 101]. Marra et al. fabricated hydroxyapatite incorporated biodegradable poly(caprolactone) and poly(D,L-lactic-co-glycolic acid) scaffolds by solvent-casting followed by particulate-leaching technique and seeded with rabbit bone marrow stromal cells . They have shown bone extracellular matrix formation (approximately 20% tissue ingrowth) after 8 weeks of in vitro culture [102]. In particulate leaching technique, defined shape salt particules are poured into a mold with hydroxyapatite crystals and polymer solution. Polymer solution is then cast into the salt-filled mold. After the evaporation of the solvent, the salt crystals are leached away using water to form the pores of the scaffold [103].

Many biomimetic approaches to mineralization involve soaking a polymer construct in simulated body fluid (SBF), a type of medium with ion concentrations approximately similar to human plasma. Different composition of SBF such as 1xSBF, 5xSBF, and 10xSBF, indicating the molar ratio of the components relative to body fluid, have been developed in order to deposit different structure of CaP crystals and reduce the duration of biomineralization [104-106]. For example, Cowan et al. fabricated

mineralized poly(lactic-co-glycolic acid) (PLGA) scaffolds by soaking the scaffold into 5xSBF and seeded with BMS cells. They have shown that mineralized PLGA scaffolds produced new bone formation after 4 weeks; however, the non-mineralized scaffolds did not show any bone formation at the same time point [107].

Most of the fabricated scaffolds have inert surface that does not allow biomineralization when incubating in the SBF. Therefore, research in the area of biomimetic mineralization has been mainly focused on the surface modification of the scaffolds. Several surface modification methods have been developed for enhancing CaP deposition [108, 109]. For example, Kim et al. functionalized the surface of Titanium (Ti) by hydroxylation which forms Ti-OH groups on the surface and immered into SBF to investigate the surface modification on bone-like apatite deposition. The results indicated that the Ti-OH groups enhanced the formation of apatite on the Ti alloys [110]. Yang et al. fabricated electrospun polycaprolactone (PCL) scaffold and functionalized with plasma surface treatment to replace the weak chemical bonding of PCL with highly reactive carbonyl (–CO–), carboxyl (–COOH) and hydroxyl (–OH) groups. They demonstrated that there was significantly higher CaP nucleation on the surface functionalized PCL scaffolds [109, 111]. Murphy et al. functionalized the surface of PLGA by hydrolysis, which increases the amount of surface carboxyl and hydroxyl groups due to scission of polyester chains. The availability of carboxyl and hydroxyl groups enhanced the apatite growth [112] .The functionalized surfaces of the biomimetic scaffolds act as an anologus template of osteonectin and bone sialoprotein, which have highly glutamic acid and aspartic acid residues and function on mineralization in natural bone. Therefore, in order to mimic the biomineralization occurs in natural bone tissue

our group has done several studies. We synthesized osteonectin-derived peptide containing 6-glutamic acid sequence by solid phase peptide synthesis. In order to covalently attach the peptide to in situ crosslinkable PLEOF hydrogel, one end of the synthesized peptide was functionalized with an acrylate group. We investigated the effect of osteonectin derived peptide on the viscoelastic properties of PLEOF/apatite composite. The results demonstrated that the osteonectin derived peptide significantly affects the shear modulus of the scaffold because of ionic interactions between the peptide and HA crystals [12, 13].

CHAPTER 3. EFFECT OF SURFACE MODIFICATION OF NANOFIBERS WITH GLUTAMIC ACID PEPTIDE ON CALCIUM PHOSPHATE NUCLEATION AND OSTEOGENIC DIFFERANTIATION OF MARROW STROMAL CELLS

Ozan Karaman, Ankur Kumar, Seyedsina Moeinzadeh, Xuezhong He, Tong Cui, Esmaiel Jabbari. Effect of Surface Modification of Nanofibers with Glutamic Acid Peptide on Calcium Phosphate Nucleation and Osteogenic Differentiation of Marrow Stromal Cells. Submitted to Journal of Tissue Engineering and Regenerative Medicine

CHAPTER 3

EFFECT OF SURFACE MODIFICATION OF NANOFIBERS WITH GLUTAMIC ACID PEPTIDE ON CALCIUM PHOSPHATE NUCLEATION AND OSTEOGENIC DIFFERANTIATION OF MARROW STROMAL CELLS

Ozan Karaman, Ankur Kumar, Seyedsina Moeinzadeh, Xuezhong He, Tong Cui, Esmaiel Jabbari

3.1 INTRODUCTION

Bone is a composite matrix composed of mineralized aligned collagen nanofibers [113]. Combination of inorganic apatite nanocrystals and organic collagen fibers provides bone with unique mechanical and biological properties [15, 114]. The apatite nanocrystals provide osteoconductivity and stiffness while the collagen fibers provide elasticity and a template for mineralization and maturation of osteoprogenitor cells. Unique factors that contribute to bone toughness are the aligned network of collagen fibers, apatite nanocrystals, and proteins in the bone extracellular matrix (ECM) that link the apatite crystals to the collagen fibers. In an effort to mimic the morphology of the ECM, electrospinning has been used to produce aligned nanofibers (NFs) [17] from natural biopolymers, like collagen and chitosan, or synthetic polymers such as poly(L-lactide) (PLLA) and poly(ε-caprolactone) (PCL) [78, 87-89]. Due to their nano-scale size and

alignment, electrospun NFs provide enormous surface area for cell adhesion, migration, and differentiation [115].

Different methods are used to create a composite of nanofibers reinforced with calcium phosphate (CaP) crystals to improve mechanical strength and provide a conductive matrix for osteoprogenitor cells [116, 117]. In one approach, CaP nanocrystals were mixed with the spinning solution and the solution was electrospun to form CaP composite NFs [118, 119]. In that approach, CaP loading and strength of the composite were limited by viscosity of the spinning solution. In another approach, electrospun nanofibers were laminated with a CaP paste to form a composite sheet [120]. This approach was limited to CaP pastes and toughness of the composite depended on the extent of penetration of the paste in the fiber mesh. In a biomimetic approach, NFs were coated with CaP crystals by incubation in a modified simulated body fluid [106, 121-123]. The latter approach mimicked the morphology of the mineralized bone matrix but drawbacks included diffusion-limited penetration of calcium and phosphate ions in the central part of the fiber sheet and crystal nucleation on the fiber surface.

Nucleation, growth, and stabilization of CaP nanocrystals on collagen fibers in the bone matrix is mediated by ECM non-collagenous proteins such as bone sialoprotein (BSP), osteonectin (ON), osteopontin (OP) and osteocalcin (OC) [12, 78, 124]. GLU sequences ranging from 2-10 residues in those proteins regulate nucleation and growth of CaP crystals on collagen fibers [124]. The objective of this study was to investigate the effect of calcium phosphate (CaP) deposition on aligned nanofibers surface-modified with a glutamic acid peptide (GLU) on osteogenic differentiation of rat marrow stromal cells (MSCs). In that regard, the peptide EEGGC consisting of two glutamic acids

terminated with a cysteine functional group at one end and two glycine residues at the other end was conjugated to low molecular weight polylactide macromer. The synthesized PLA-GLU polymer-peptide conjugate was blended with high molecular weight poly(lactide-co-glycolide) (PLGA) polymer and the blend was electrospun to form aligned nanofibers surface-modified with GLU peptide (GLU-NF). The GLU-NF microsheets were incubated in a modified simulated body fluid (SBF) for GLU-mediated nucleation and growth of CaP crystals on the fiber surface. To achieve a high CaP to fiber ratio, a layer-by-layer approach was used to improve the diffusion of calcium and phosphate ions inside the microsheets. The effect of GLU-mediated CaP deposition on aligned nanofibers on osteogenic differentiation of rat MSCs was investigated by cytochemical, mRNA expression, and immunocytochemical analysis. Results demonstrate that surface modification of nanofibers with GLU peptide dramatically increased nucleation and growth of CaP nanocrystals on the fiber surface, leading to significantly higher differentiation of MSCs and mineralized matrix formation.

3.2 MATERIALS AND METHODS

3.2.1. SYNTHESIS AND CHARACTERIZATION OF PLA-GLU CONJUGATE

Cysteine-terminated EEGGC peptide was synthesized manually on Rink Amide NovaGel^{TM} resin (EMD Biosciences, San Diego, CA) in the solid phase and functionalized by the addition of a cysteine residue at the glycine end using a previously described procedure [125-127]. Briefly, the Fmoc-protected amino acid (6 equiv), *N*,*N*′-di-isopropylcarbodiimide (6.6 equiv, DIC, Acros, Pittsburgh, PA) and hydroxybenzotriazole (12 equiv, HOBt, Acros) were added to 100 mg resin and swelled in *N*,*N*-Dimethylformamide (DMF, Acros). Next, 0.2 mL of 0.05 M *N*,*N*-

dimethylaminopyridine (DMAP, Acros) was added to the mixture and the coupling reaction was allowed to proceed for 4-6 h at 30ºC with orbital shaking. The resin was tested for the presence of unreacted amines using the Kaiser reagent [128]. After coupling the last amino acid, the EEGGC peptide was cleaved from the resin and precipitated in cold ether. The peptide was purified by preparative HPLC and characterized by Finnigan 4500 Electro Spray Ionization (ESI) spectrometry (Thermo Electron, Waltham, MA) as described [127]. A similar procedure was used to synthesize EEGGKC peptide.

L-lactide (LA; >99.5% purity; Ortec, Easely, SC) monomer was dried under vacuum at 40°C for at least 12 h prior to the reaction. Low molecular weight poly(L-lactide) (LMW-PLA) was synthesized by ring-opening polymerization of LA monomer as previously described [125, 129]. Diethylene glycol (DEG, Fisher, Waltham, MA) and tin (II) 2-ethylhexanoate (TOC, Sigma-Aldrich) were used as the polymerization initiator and catalyst, respectively. The molar ratios of DEG:TOC and LA:DEG were 20:1 and 10:1, respectively. After the reaction, double precipitation in two non-solvents, diethyl ether and hexane, was used to fractionate and isolate the LMW-PLA [125]. The synthesized polymer was characterized by gel permeation chromatography (GPC) and ^{1}H-NMR as described [125]. Next, the LMW-PLA chain was terminated with an acrylamide group by reaction with acryloyl chloride (Ac, Sigma-Aldrich). In a typical reaction, 20 g LMW-PLA was dissolved in 150 mL dichloromethane (DCM, Acros) under dry nitrogen atmosphere. After cooling to 5°C, 0.6 mL Ac and 1.55 mL triethylamine (TEA, Sigma-Aldrich), each dissolved in DCM, were added drop-wise to the reaction with stirring. The reaction continued for 6 h on ice followed by 12 h under ambient conditions. After the reaction, solvent was removed and residue was dissolved in

anhydrous ethyl acetate to precipitate and remove the byproduct triethylamine hydrochloride. The Ac-PLA product was precipitated twice in hexane and cold ether, and dried in vacuum. The $\bar{M}_n$ and polydispersity index of the Ac-PLA were 5.3 kDa and 1.2, respectively.

EEGGC peptide was conjugated to Ac-PLA by Michael addition reaction between the cysteine's sulfhydryl group on the peptide and the acrylate group on the polymer to produce the PLA-GLU conjugate. Briefly, the peptide dissolved in sodium borate buffer (pH 8.5), was added to a solution of Ac-PLA in DMF (2:1 peptide:Ac-PLA molar ratio) and allowed to react for 12 h at 30°C in an orbital shaker. The solution was then dialyzed (MW cutoff 3.5 kDa, Spectrum Laboratories, Rancho Dominquez, CA) against distilled deionized (DI) water and lyophilized to obtain the dry PLA-GLU conjugate. The chemical structure of the conjugate was characterized by ^{1}H-NMR.

3.2.2 PLGA/PLA-GLU FIBER SPINNING

PLGA sample (*Durect, Pelham,* AL) was a 50/50 copolymer of D,L-lactide and glycolide monomers with intrinsic viscosity of 1.1 dL/g and weight average molecular weight of 105 kDa. A blend of 10 wt% high molecular weight PLGA and 1.5 wt% PLA-GLU was dissolved in 1, 1, 1, 3, 3, 3-hexafluoro-2-propanol (HFIP, VWR, West Chester, PA) solvent. A programmable KDS100 syringe pump (KD Scientific, Holliston, MA) was used to transfer and inject the polymer solution from a 1 mL syringe through a 21-gauge needle. The needle was connected to the positively charged Pt electrode of a high voltage power supply (ES40P-5W/DAM, Gamma High Voltage Research). A custom-built aluminum rotating wheel (20 cm diameter and 5 mm thickness), powered by a high-speed DC motor ((2M0578, Dayton Electric, Niles, IL) and connected to the ground

electrode of the power source, was used to collect the aligned fibers [17, 130]. The rotating collector was placed 7.5 cm below the needle, with the edge of the wheel facing the needle. The previously optimized electrospinning conditions of 1.0 mL/h injection rate, 20 kV electrical potential, and needle-to-collector distance of 7.5 cm were used [93]. A rotation speed of 1200 rpm was used to produce aligned PLGA/PLA-GLU fibers, hereafter denoted by GLU-NF.

3.2.3 CHARACTERIZATION OF GLU-CONJUGATED NANOFIBERS

Scanning electron microscopy (SEM) was used to image the nanofibers. After coating with gold (Polaron sputter coater, Quorum Technologies, New Haven, UK) at 20 mA for 45 sec, the fiber mesh was attached to a SEM stub and imaged with a Field Emission Scanning Electron Microscope (FESEM, Carl Zeiss Microscopy, Hillsboro, OR) at an accelerating voltage of 8 kV. SEM images were analyzed with ImageJ software (National Institutes of Health, Bethesda, MD) to determine the average fiber size.

To determine surface coverage of GLU peptide on aligned nanofibers, EEGGKC peptide (GLUK) containing a lysine residue between the glycine and cysteine residues was synthesized and conjugated to LMW-PLA. After electrospinning, the fibers were fluorescently labeled with fluorescein isothiocyanate (FITC, Sigma-Aldrich) in 5 mg/mL Dulbecco's phosphate-buffered saline (PBS, Cellgro, Herndon, VA) for 4 h at ambient conditions. FITC, due to its size, reacts only with free lysine amine group of GLUK on the fiber surface. Therefore, assuming addition of lysine to EEGGC peptide did not significantly change the peptide surface density, the FITC fluorescent intensity was related to GLU density on the fiber surface. FITC-labeled GLUK-conjugated nanofibers were imaged with an inverted fluorescent microscope (Nikon Eclipse Ti-ε, Nikon,

Melville, NY). Next, the labeled nanofibers were dissolved in DMSO and fluorescent intensity was quantified with a Synergy HT plate reader (Bio-Tek, Winooski, VT) at emission and excitation wavelengths of 520 and 495 nm, respectively. Knowing mass and average size of the fibers, the intensities were converted into mass per unit surface area using a calibration curve generated by measuring the fluorescent intensity of solutions with known concentration of FITC in dimethylsulfoxide (DMSO, Sigma-Aldrich). PLGA nanofibers without EEGGKC peptide dissolved in DMSO were used as negative control.

3.2.4 CaP NUCLEATION AND GROWTH ON GLU-NF MICROSHEETS

GLU-NF microsheets, approximately 25 μm thick, were incubated in a modified 10-fold concentrated simulated body fluid (m10SBF) [106]. Briefly, the stock solution of 10SBF was prepared by dissolving sodium chloride (NaCl), potassium chloride (KCl), calcium chloride monohydrate (CaCl2• H2O), magnesium chloride hexahydrate (MgCl2• 6H2O), sodium bicarbonate (NaHCO3), and monosodium phosphate (NaH2PO4), all purchased from Fisher, in DDI water. The final pH of 10SBF solution was 4.2. Next, 60 mM solution of $NaHCO_3$ was added to 10SBF stock solution to reach physiological pH of 7.4. Then, the suspension was centrifuged and filtered (220 nm pore-size) prior to incubation. The modified-10SBF (m10SBF) solution was transparent after filtration, containing no CaP crystals when incubated with GLU-NF microsheets. During incubation, the containers were sealed with Parafilm to prevent a change in solution pH by CO_2 diffusion. The incubation solution was changed every 6 h to replenish calcium and phosphate components. At each time point, fiber sheets were washed with DI water and dried at ambient conditions.

In the layer-by-layer approach, the first GLU-NF microsheet, approximately 5 μm

thick, was electrospun on a 12 mm circular glass coverslip (VWR, Bristol, CT). Next, the microsheet was incubated in m10SBF for the prescribed time, washed with DI, and dried. After drying, the second GLU-NF layer was electrospun directly on the first layer. The bilayer sheet was incubated in m10SBF for a prescribed time, washed with DI, and dried. This layer-by-layer process was repeated five times to produce a 26±2 μm thick mineralized multilayer GLU-NF circular sheet (12 mm diameter). The multilayer approach improved diffusion of calcium and phosphate ions inside the fiber sheet when incubated in m10SBF solution.

The mineralized microsheets were imaged with FESEM as described above. The calcium to phosphate ratio of the microsheets was measured by an energy-dispersive X-ray spectrometer (EDS) connected to FESEM at an accelerating voltage of 15 kV. The structure of CaP crystals on GLU-NF microsheets was determined by Wide-Angle X-Ray Diffraction (XRD) using a Philips diffractometer with CuKα radiation source at 30 kV (Model 405S5, Rigaku, Japan). The scanning range was from 10 to 50^{o} with a step size of 0.05^{o}. The water wettability of GLU-NF microsheets before and after mineralization was measured with a contact angle goniometer (Model DSA-20E, Kruss, Germany). A 10 μl drop of DI water was applied to the fiber surface, photographed immediately and contact angle (θ) was calculated from the height (*h*) and breadth (*b*) of the drop according to θ=arctan (2h/b) [131].

The amount of CaP nucleation on the microsheets was measured using a QuantiChrom calcium assay (Bioassay Systems, Hayward, CA) according to manufacturer's instructions. Calcium content of the microsheets (0.3 mg) was dissolved in 0.4 mL of 1M HCl. Next, 5 μL aliquot of the suspension was added to 200 μL of the

kit working solution. After 3 min incubation, absorbance was measured on a Synergy HT plate reader at a wavelength of 612 nm. Measured intensities were correlated to the equivalent amount of Ca^{2+} using a calibration curve constructed with reference $CaCl_2$ solutions (zero to 200 μg/mL concentration). Total mineralized deposit of each sample was determined from the measured calcium contents at each time point (2, 4, 6, 12, and 24 hours) and the CaP ratios from EDS measurements, and divided by the fiber mass to find percent CaP. Tensile modulus of the samples was measured with a Rheometrics Dynamic Mechanical Analyzer (RSA III DMA, Piscataway, NJ) with a strain rate of 0.033/s at ambient conditions. Samples were cut to dimensions of 20 x 5 mm and the maximum allowed strain was set at 160%. Thickness and width of the samples were measured with a micro-caliper (Mitutoyo, Aurora, IL) and modulus was calculated as the slope of the linear region of the stress-strain curve.

3.2.5 CELL ISOLATION AND SEEDING

MSCs were isolated from the bone marrow of 6-8 weeks-old male Wistar rats as described [125, 127, 132]. Cell isolations were performed under a protocol approved by the Institutional Animal Care and Use Committee of the University of South Carolina. The marrow was flushed with 20 mL of cell isolation medium which consisted of Dulbecco's Modified Eagle's Medium (DMEM; 4.5 g/L glucose with L-glutamine and without sodium pyruvate, Cellgro, Herndon, VA) and 10% Fetal bovine serum (FBS, Atlas Biologicals, Fort Collins, CO) supplemented with 100 units/mL penicillin (PN), 100 μg/mL streptomycin (SP), 20 μg /mL fungizone (FG), and 50 μg /mL gentamicin sulfate (GS), all purchased from Sigma-Aldrich. The cell suspension was cultured in basal medium (DMEM supplemented with 10% FBS, 100 units/mL PN, 100 μg/mL SP,

50 µg/mL GS, and 250 ng/mL FG). Cultures were replaced with fresh medium at 3 and 7 days to remove unattached cells. Cells were enzymatically lifted and used for cell culture experiments. For cell seeding, edges of the microsheets on 12 mm circular glass coverslip were coated with a medical-grade silicone sealant (Dow Corning, MI) to prevent separation of the mesh from coverslip. The construct was sterilized by ultraviolet (UV) radiation followed by immersion in 70% ethanol for 30 min and washing three times with sterile PBS. We and others have demonstrated that UV radiation followed by immersion in ethanol is an effective procedure for sterilizing nanofibers [89, 93, 133]. SEM images (a) and (b) in Figure 3.7 show the morphology of GLU-NF nanofibers before and after ethanol incubation and washing steps during sterilization, respectively; images (c) and (d) show the morphology GLU-NF/CaP50 nanofibers before and after sterilization. The images in Figure 3.7 indicate that the sterilization procedure had no visible effect on the alignment or size of the fibers (images a and b) and attachment of CaP deposits to the fiber surface (images c and d). After conditioning the fiber mesh in basal medium for 1 h, each sample was seeded with 60 µL MSC cell suspension ($1.7x10^6$ cells/mL; $1x10^5$ cells/cm^2) in basal medium. After incubation for 24 h for cell attachment, the medium was replaced with osteogenic medium (basal medium supplemented with 100 nM dexamethasone, 50 µg/mL ascorbic acid, 10 mM ß-glycerophosphate) and cultured in a humidified 5% CO_2 incubator for up to 28 days. MSCs seeded on GLU-NF/LBL/CaP200 microsheets and incubated in basal medium without osteogenic factors (GLU-NF/LBL/CaP200-BM group) were used as the negative control group. To determine cell viability, MSCs seeded on the microsheets were stained with Acetomethoxy derivative of calcein (cAM, Life Technologies, Grand Island, NY) and ethidium homodimer (EthD,

Life Technologies) to image live and dead cells, respectively. Stained samples were imaged with a Nikon Eclipse Ti-ε inverted fluorescent microscope. Cell viability was quantified by dividing the image into smaller squares and counting the number of live and dead cells manually.

3.2.6 OSTEOGENIC DIFFERENTIATION OF MSCs ON CaP-DEPOSITED GLU-NF MICROSHEETS

At each time point (7, 14, 21, and 28 days), cell-seeded nanofibers were washed with serum-free DMEM for 8 h to remove serum proteins, followed by washing with PBS and lysed with 10 mM Tris supplemented with 0.2% triton in PBS. The lysed samples were used for measurement of DNA content, ALPase activity and calcium content. Double-stranded DNA content, ALPase activity and calcium content of the samples were measured with Quant-it PicoGreen assay (Invitrogen), QuantiChrom ALPase assay (Bioassay Systems) and QuantiChrom Calcium Assay (Bioassay Systems), respectively, as described [134]. To determine extent of mineralization of the samples, the measured intensities at time zero, used as baseline, were subtracted from those at days 7-28 to account for the deposited CaP prior to cell seeding. The measured ALPase activities and calcium contents were normalized to cell numbers by dividing to DNA contents at each time point.

3.2.7 IMMUNOFLUORESCENT STAINING

For immunofluorescent staining, cell-seeded microsheets were washed twice in PBS and fixed with 4% paraformaldehyde (Sigma-Aldrich) at 4°C for 12 h. Next, samples were permeabilized with 0.1% Triton X-100 and 100 mM glycine in PBS for 1 h and blocked with 1.5% BSA and 0.5 mM glycine in PBS for 2 h. Then, samples were

incubated with primary antibodies in PBS containing 1% BSA for 24 h at 4°C according to manufacturer's instructions. Primary antibodies from Santa Cruz Biotechnology (Santa Cruz, CA) included mouse anti-rat OP (1:100 dilution), rabbit anti-rat OC (1:100 dilution), and goat anti-rat Pecam-1 (1:50 dilution). After washing with PBS, samples were incubated with the secondary antibody (1:100 dilution) in blocking buffer for 2 h at ambient conditions. Secondary antibodies from Santa Cruz Biotechnology included donkey anti-mouse FITC-conjugated IgG, donkey anti-rabbit Texas-red conjugated IgG, and donkey anti-goat Texas-red conjugated IgG. It should be noted that each sample was stained with 4,6-diamidino-2-phenylindole (DAPI, Sigma-Aldrich) to image the cell nuclei and one of the antibodies for OC, OP, or Pecam-1. Secondary antibodies without the primaries were used as negative controls. For observation of cell morphology, cell-seeded GLU-NF microsheets were incubated with 0.16 μM Alexa Fluor® 594 phalloidin (Invitrogen) and 300 nM DAPI for 30 min at ambient conditions to stain the cell actin filaments and nuclei, respectively. The stained samples were imaged with a Nikon Eclipse Ti-ε inverted fluorescent microscope to observe cell morphology or expression pattern of the proteins with the same exposure time and light intensity.

3.2.8 mRNA ANALYSIS OF MSCs ON CaP-DEPOSITED GLU-NF MICROSHEETS

At each time point (7, 14, 21, and 28 days), total cellular RNA was isolated using TRIzol (Invitrogen) as described [134]. 1μg of the extracted purified RNA was subjected to cDNA conversion using Promega Reverse Transcription System (Madison, WI). The obtained cDNA was subjected to real time quantitative polymerase chain reaction (rt-qPCR) amplification with appropriate gene specific primers. The expression level of ribosomal protein S16 was used as the endogenous control. Primers for real-time PCR

analysis were designed and selected using Primer3 web-based software as described [125, 135]. Real-time PCR (RT-qPCR) was performed to analyze differential expression of OP, ALPase, OC, Collagen type I (Col-1), Pecam-1 and Flk-1 genes with SYBR green RealMasterMix (Eppendorf, Hamburg, Germany) using Bio-Rad CXF96 machine (Bio-Rad, Hercules, CA). Forward and reverse primers, shown in Table 1, were synthesized by Integrated DNA technologies (Coralville, IA). The designed primer sequences corresponded closely to the previously reported sequences for OP, ALPase, OC, Col-1, Pecam-1 and Flk-1 genes in rat MSCs [136, 137]. Relative gene expression levels were quantified by the 2^–ddCT method as described [138, 139]. Relative gene expressions were expressed as fold difference compared with that at time zero.

Table 1 Forward and reverse sequences of the PCR primers.

Genes	Forward Primer	Reverse Primer
ALPase	5′-CCT TGA AAA ATG CCC TGA AA-3′	5′-CTT GGA GAG AGC CAC AAA GG-3′
Osteocalcin	5′-AAA GCC CAG CGA CTC T-3′	5′-CTA AAC GGT GGT GCC ATA GAT-3′
Osteopontin	5′-GAC GGC CGA GGT GAT AGC TT-3′	5′-CAT GGC TGG TCT TCC CGT TGC-3′
Col-I	5′-TGC CGA TGG CGC TAT C-3′	5′-CAA GGG CCG GGG TGA CGC GGG-3′
PECAM-1	5′-CGA AAT CTA GGC CTC AGC AC-3′	5′-CTT TTT GTC CAC GGT CAC CT-3′
Flk-1	5′-TAG CGG GAT GAA ATC TTT GG -3′	5′-GGG GTG AGG ATG ACC GTG TA-3′
S16	5′-AGT CTT CGG ACG CAA GAA AA-3′	5′-AGC CAC CAG AGC TTT TGA GA-3′

3.2.9 STATISTICAL ANALYSIS

Data are expressed as means±standard deviation. All experiments were done in triplicate. Significant differences between groups were evaluated using a two-tailed Student's t-test. A value of $p<0.05$ was considered statistically significant.

3.3 SIMULATION METHOD

Dissipative Particle Dynamics (DPD) method was used to simulate surface and bulk distribution of PLGA and PLA-GLU in the nanofibers by course-graining the

macromers into different set of atoms or beads as described [140, 141]. Bead types included lactide, glycolide, acrylate, amino acid backbone chain, cysteine side group, and glutamic acid side group. The position and velocity of the beads at each time point were determined by solving equations of motion of the beads using the DPD force function. The force acting on each bead (f_i) is given by [142, 143]

$$f_{ij} = \sum_{i \neq j} F_{ij}^{C} + F_{ij}^{D} + F_{ij}^{R} + F_{ij}^{S} \quad (1)$$

where F_{ij}^{C}, F_{ij}^{D}, F_{ij}^{R} and F_{ij}^{S} are the conservative, dissipative, random and spring components of the force, respectively. F_{ij}^{D}, F_{ij}^{R} and F_{ij}^{S} were calculated as described [140, 141]. The interaction force F_{ij}^{C} between non-bonded beads is given by [143]

$$F_{ij}^{C} = \begin{cases} \alpha_{ij} (1 - r_{ij}) e_{ij} & |r_{ij}| < 1 \\ 0 & |r_{ij}| \geq 1 \end{cases} \quad (2)$$

where r_{ij} is the vector joining bead i to j, e_{ij} and $|r_{ij}|$ are the unit vector in the direction of r_{ij} and the magnitude of r_{ij} in DPD units, respectively. DPD length scale r_c was 7.87 Å and the values of α_{ij} were determined from the Flory-Huggins interaction parameters (χ_{ij}) as described [140, 144]. The Flory−Huggins parameters were calculated via atomistic molecular dynamics simulation (Forcite and Amorphous Cell modules, Materials Studio v5.5, Accelrys) using COMPASS, which is an *ab initio* force field optimized for condensed-phase systems [145]. The randomly seeded macromers in a cylindrical template were simulated with dimensionless time step of 0.05 and over 200000 time

steps. The repulsive boundary condition applied on the fiber surface to maintain cylindrical geometry was equal for all beads, which did not affect bead distribution. DPD simulations were performed using Mesocite module (Materials Studio v5.5).

3.4. RESULTS

3.4.1 CHARACTERIZATION OF CaP-DEPOSITED GLU-NF MICROSHEETS

GLU peptide was covalently attached to Ac-PLA by the reaction between the acrylate group of Ac-PLA and cysteine residue of the peptide, as shown in Figure 3.1a. ^{1}H-NMR spectrum of Ac-PLA (inset) and PLA-GLU are shown in Figure 3.1b. Chemical shifts with peak positions at 2.14, 2.32 and 4.57 were attributed to methylene and methine hydrogens of glutamate residues; that at 4.16 was attributed to methylene hydrogens of glycine residues; those at 5.19 and 8.03 were attributed to amine and amide hydrogens, respectively; and those at 3.11 and 3.77 were attributed to methylene and methine hydrogens of cysteine residue, respectively. Chemical shifts with peak positions at 1.78 and 5.35 ppm were attributed to methyl and methine hydrogens of lactide units, respectively; that at 3.64 ppm was attributed to methylene hydrogens of DEG in Ac-PLA. Chemical shifts with peak positions in the 6.04-6.48 ppm range were attributed to vinyl hydrogens of the acrylate end groups of Ac-PLA. Ratio of the peaks at 6.04-6.48 ppm (due to hydrogens of acrylate) to that at 5.35 ppm (due to hydrogens of lactide) was related to acrylate/LA molar ratio in Ac-PLA macromer. Number of peptides in the conjugate was determined using the acrylate/LA molar ratio before and after conjugation. Average number of peptides per conjugate was 1.3.

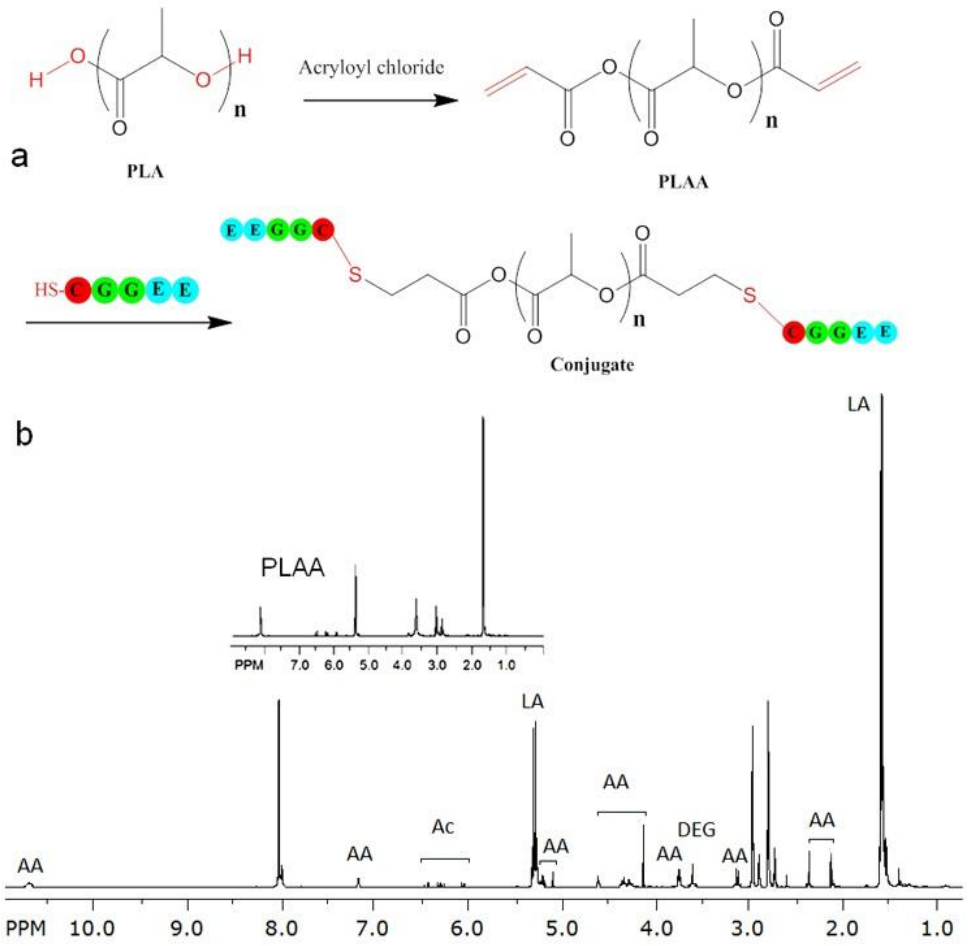

Figure 3.1 (a) Reaction scheme for synthesis of PLA-CGGEE (PLA-GLU) conjugate. (b) ^{1}H-NMR spectrum of PLA-GLU macromer; the inset in (b) is NMR spectrum of Ac-PLA. NMR peaks labeled with LA, AA, and Ac represent lactide, amino acid, and acrylate peaks, respectively.

Concentration of PLA-GLU in the fibers ranged from zero to 2.5 mM. Average size of the aligned fibers was 200 ±60 nm. Image of PLGA/PLA-GLUK fibers, shown in Figure 3.2a, showed intense fluorescent emission from FITC conjugation to the fiber surface. FITC-labeled fibers were dissolved in DMSO and fluorescent intensity was quantified and related to GLU peptide concentration, as shown in Figure 3.2b. GLU density on the fiber surface increased linearly with PLA-GLU concentration up to 2 mM, followed by a slight, statistically not significant increase for higher concentrations. As

PLA-GLU concentration was increased from 0.6 mM to 1.2, 2.0, 2.3 and 2.5 mM, GLU surface density increased from 5.4±1.2 to 12.3±0.9, 20.3±2.5, 20.7±2.7, and 21.1±2.3 nmol/cm^2, respectively. DPD simulation of PLGA/PLA-GLU nanofibers to predict GLU distribution on the fiber surface in a 30 x 20 x 20 r_c simulation box without HFIP electrospinning solvent is shown in Figure 3.2c. In the figure, beads other than GLU (red color) are shown with grey color for clarity. The percentage of GLU groups on the fiber surface without and with 5% HFIP solvent was 82% and 83%, respectively, and the average number of GLU peptides on the surface was 0.16 GLU/nm^2.

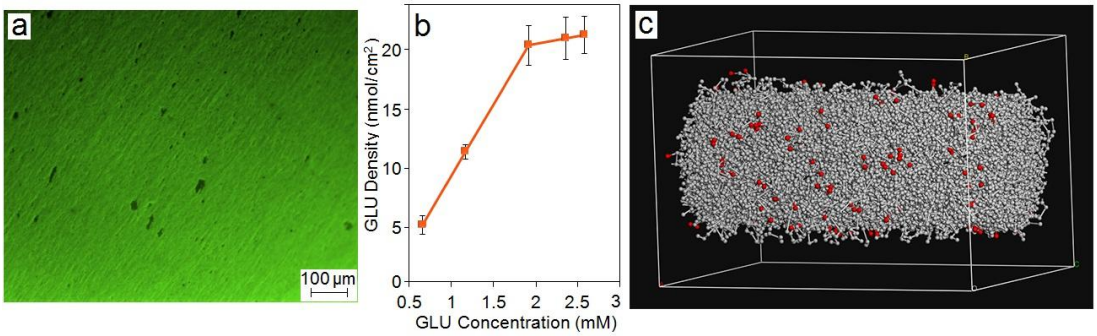

Figure 3.2 (a) Fluorescent image of FITC conjugated PLA-GLUK nanofibers with 20 nmol/cm^2 GLUK peptide surface density. (b) Effect of PLA-GLUK peptide concentration in the electrospinning solution on GLUK peptide surface density on aligned nanofibers. (c) DPD simulation of PLGA/PLA-GLU showing localization of GLU groups (red) on the surface of nanofibers (grey) within the simulation box. Error bars in (a) and (b) correspond to mean ±1 SD for n = 3.

The schematic diagram of apatite deposition on 2-mer Glutamic acid peptide conjugated nanofibers in simulated body fluid is represented in Figure 3.3. Typical low magnification images of nanofibers (without GLU conjugation) and GLU-NF after incubation in m10SBF for 24 h are shown in Figures 3.4a and 3.4b, respectively. Figures 3.4c-f show higher magnification images of GLU-NF after incubation in m10SBF for 6,

24, 48 h, and LBL 24 h, respectively. CaP crystals nucleated from the fiber surface after 6 h incubation can be seen in Figure 3.4c. As incubation time increased to 24 and 48 h, number of CaP crystals increased significantly, as shown in Figures 3.4d and 3.4e, respectively. Figure 3f shows uniform distribution of CaP crystals on fibers within as well as on the surface of microsheets. However, average size of the crystals did not change with incubation time and remained below 100 nm. The schematic diagram of apatite deposited GLU-NF fabrication by layer-by-layer approach can be seen in Figure 3.5a. In addition, Figure 3.5b and 3.5c shows the low and high magnification image of 5 layers apatite/GLU-NF cross-section, respectively. The average thickness of CaP nucleated 5 layers GLU-NF is 25±1 μm.

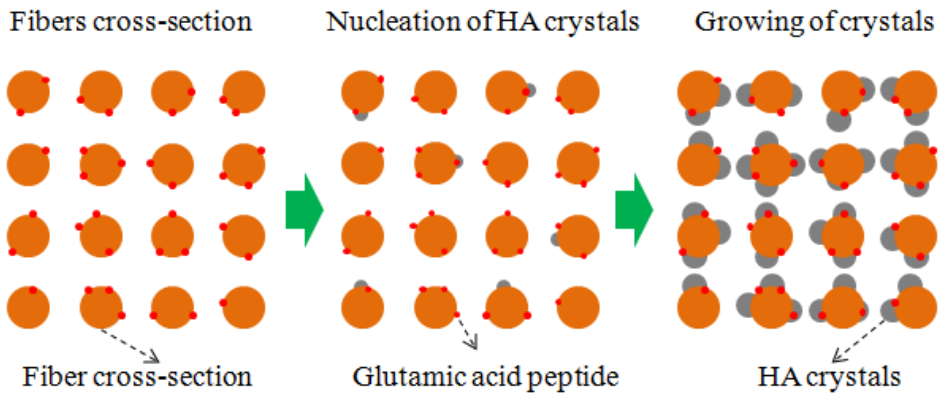

Figure 3.3 The schematic diagram of apatite deposition on 2-mer Glutamic acid peptide conjugated nanofibers in simulated body fluid.

The effect of GLU conjugation and CaP deposition on water wettability of the microsheets is shown in Figure 4a-c. Water contact angel decreased to 85±3º (Figure 3.6b) from 112±3º (Figure 3.6a) after blending PLGA with PLA-GLU. The mineralized microsheets were completely wetted by water (zero contact angle, Figure 3.6c). The

measured contact angles were consistent with previously reported values for PCL modified with carboxylic acid groups [146, 147]. The amount of CaP crystals (based on fiber mass) deposited on NF (burgundy), GLU-NF (blue), and GLU-NF/LBL (brown) microsheets with incubation time is shown in Figure 3.6d. As incubation time increased from 2 to 4, 6, 12, and 24 h, amount of CaP deposited on NF microsheets changed from 2.8±2.2% to 8.7±0.9, 8.6±2.5, 11.6 ±1.0, and 12.1±2.5%, respectively, while the amount deposited on GLU-NF microsheets increased from 13.3±0.7% to 28.0±3.8, 29.4±4.5, 37.0±5.1, and 50.0±5.6%. Amount of CaP deposited on NF microsheets did not increase significantly with incubation time while CaP deposition on GLU-NF sheets increased significantly (indicated by one star). Interestingly, amount of CaP deposited with the LBL approach (24 h incubation in each layer) increased to 203±5% compared to 50.0±5.6% for a single 25 μm layer. These results indicated that the GLU peptide provides sites for nucleation of CaP crystals [148] and CaP deposition is limited by the diffusion of calcium/phosphate ions to the interior part of GLU-NF microsheets.

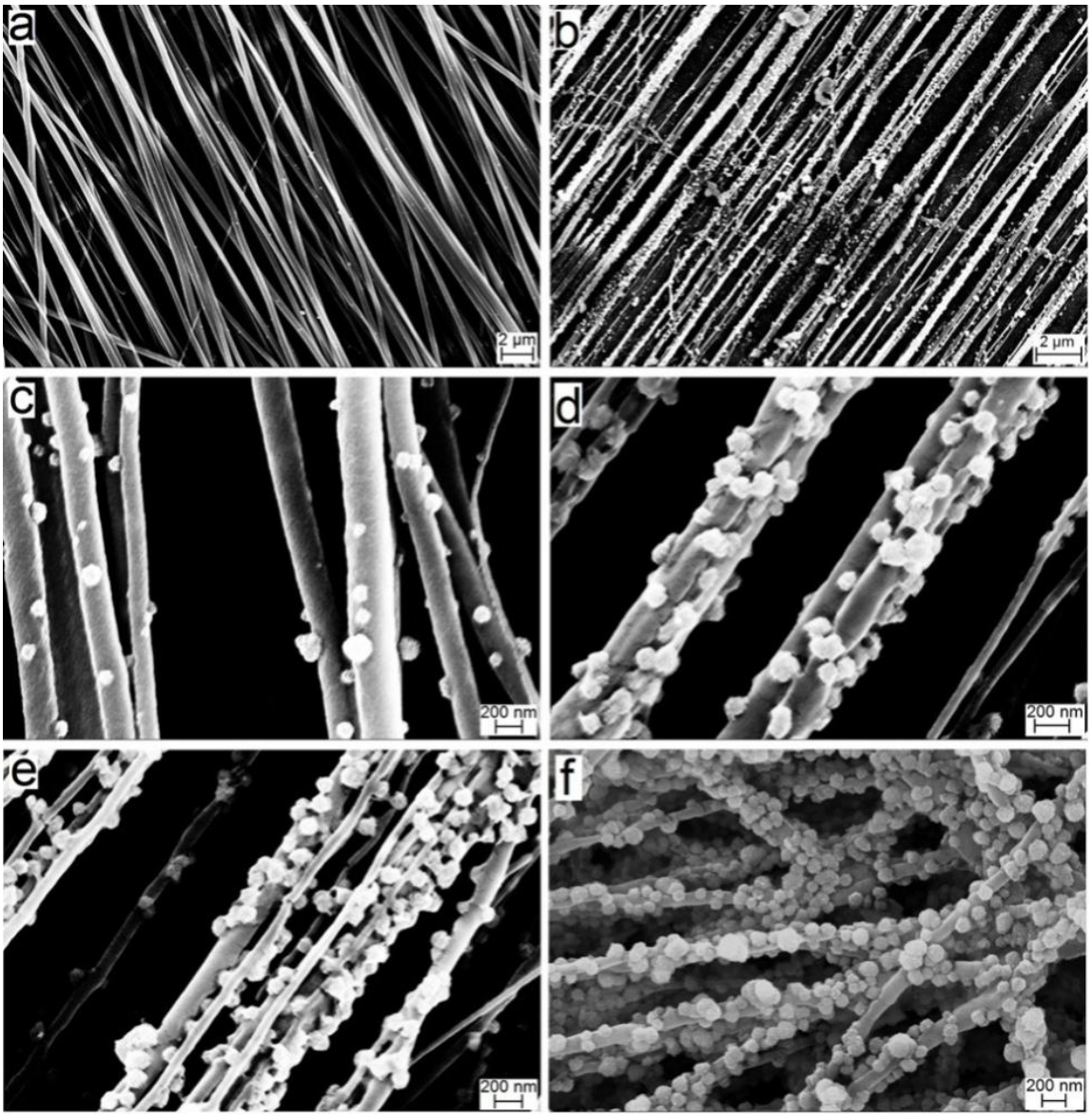

Figure 3.4 SEM images of the microsheets after incubation in m10SBF medium. Images (a) and (b) are low magnification images of PLGA and PLGA/PLA-GLU microsheets after incubation in m10SBF for 24 h, respectively. Images (c), (d), and (e) are for PLGA/PLA-GLU microsheets after 6, 24, and 48 h incubation in m10SBF, respectively. Image (f) is for PLGA/PLA-GLU microsheets deposited with CaP crystals in a layer-by-layer (LBL) approach. Scale bars in (a-b) and (c-f) represent 2 µm and 200 nm, respectively.

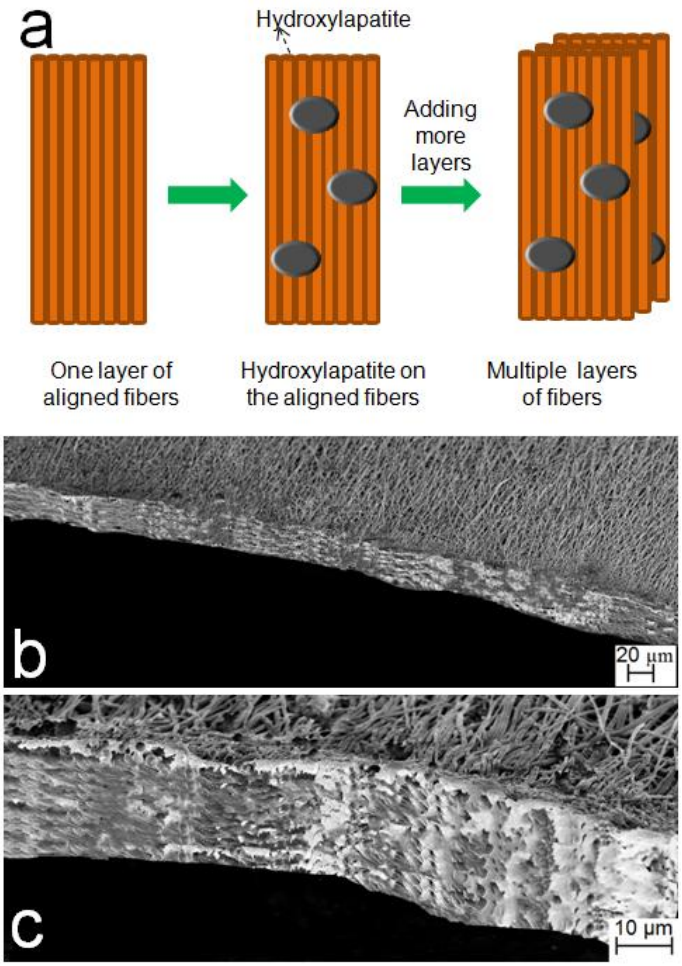

Figure 3.5. Schematic diagram of apatite deposited GLU-NF fabrication by layer-by-layer approach (a), low magnification image of 5 layers apatite/GLU-NF cross-section (b), high magnification image of 5 layers apatite/GLU-NF cross-section.

Tensile modulus and toughness of GLU-NF microsheets are given in Figures 3.6e and 3.6f, respectively. Tensile modulus increased significantly with extent of CaP deposition on the fibers, especially in the LBL approach. Tensile modulus increased from 260±10 MPa for GLU-NF to 330±17, 540±15, and 880±40 MPa for GLU-NF with 30% (6 h incubation), 50% (24 h incubation), and 200% (LBL) CaP deposition. There was a sharp increase in toughness when CaP deposition was increased to 50% and 200%, indicating overlap/fusion of crystals on the fibers and formation of a CaP-NF network.

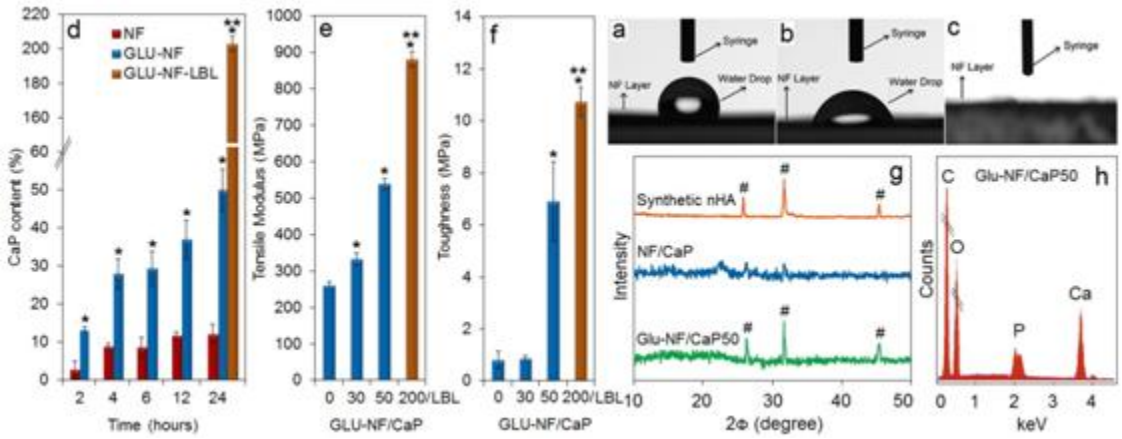

Figure 3.6 Shape of a water droplet on PLGA NF (a), PLGA/PLA-GLU NF before (b) and after incubation in m10SBF (c). All PLGA/PLA-GLU NF microsheets had zero water contact angle after incubation in m10SBF, irrespective of incubation time. The contact angles in (a), (b), and (c) were 112±3º, 85±3º, and zero, respectively. (d) Amount of CaP nucleation and growth (based on fiber mass) on PLGA fibers without GLU conjugation (NF, burgundy, 25 µm thick layer) and PLGA/PLA-GLU fibers (GLU-NF, blue, 25 µm thick layer) with incubation time in m10SBF. (e) and (f) are tensile modulus and toughness of PLGA/PLA-GLU fibers as a function of CaP amount deposited on the fibers, respectively. The brown bar in (d-f) is for PLGA/PLA-GLU microsheets produced in a 5-layer LBL approach (each layer 5 µm thick) incubated in m10SBF for 24 h. (g) Comparison of x-ray diffraction spectra of CaP crystals deposited on PLGA NF (NF/CaP, blue) and CaP crystals deposited on PLGA/PLA-GLU microsheets (GLU-NF/CaP50, green) after 24 h incubation in m10SBF with that of commercial HA nanocrystals (nHA, orange). Peaks centered at 25.8°, 31.8°, and 47° are characteristic diffraction peaks of apatite crystals. (h) EDS spectrum of CaP crystals nucleated and grown on GLU-NF/CaP50 fibers (Ca:P =1.58). In (d-f), one star indicates statistically significant difference (s.d.; $p<0.05$) between the test group and control [NF in (d) and GLU-NF/CaP0 in (e) and (f)]; two stars between multilayer and monolayer GLU-NF/CaP. Error bars in (d-f) correspond to means ± 1 SD for n = 3.

The mechanical measurements are consistent with previous results for CaP-deposited PCL NFs, surface modified with carboxylic acid groups [149]. XRD spectra of NF (blue) and GLU-NF (green) microsheets after 24 h incubation in m10SBF are compared in Figure 4g with that of synthetic apatite nanocrystals (red, Berkeley Biomaterials, Berkeley, CA). CaP crystals deposited on GLU-NF microsheets showed the characteristic

apatite peaks centered at 31.8^{o}, 25.8^{o,} and 47^{o} [150] while NF sheets without GLU did not show those peaks. Ca/P ratio of the crystals was 1.58±0.1, based on the EDS spectrum of GLU-NF microsheets after 24 h incubation in m10SBF in Figure 4h, which was in the reported range of 1.4-1.7 for CaP crystals in the natural bone and close to 1.67 for synthetic apatite crystals [116]. Similar results were obtained for GLU-NF microsheets incubated in m10SBF for different times.

3.4.2 DIFFERENTIATION OF MSCs ON CaP-DEPOSITED GLU-NF MICROSHEETS

MSCs were seeded on GLU-NF, GLU-NF with 30% (GLU-NF/CaP30), 50% (GLU-NF/CaP50), and 200% (GLU-NF/LBL/CaP200) CaP content, and cultured in osteogenic medium for 28 days. MSCs seeded on GLU-NF/LBL/CaP200 with highest CaP content of 200% and incubated in basal medium was used as the negative control group (GLU-NG/LBL/CaP200-BM) for biochemical, mRNA and immunocytochemical analysis. To observe the morphology of individual cells, MSCs were seeded on the microsheets at low density of 1500 cells/cm^2 and incubated in osteogenic medium. Fluorescent images (a-d) of cell nuclei (blue) and cytoskeletal actin filaments (red) in Figure 3.9 show morphology of the MSCs seeded on GLU-NF (a), GLU-NF/CaP30 (b), GLU-NF/CaP50 (c), and GLU-NF/LBL/CaP200 (d) microsheets after two days of incubation. The images indicate that the seeded cells completely aligned with fiber direction even after CaP deposition. Inset images in Figure 3.9 show the corresponding morphology of MSCs with initial seeding density of 1x10^5 cells/cm^2 after 7 days of incubation in osteogenic medium. The seeded MSCs displayed an elongated morphology in the direction of the fibers for all CaP contents at higher density and longer incubation time. Images of live (green, cAM stained) and dead (red, EthD stained) MSCs two days after cell seeding at high density on

the microsheets, displayed in Supplementary Figure 3.8, showed >90% cell viability two days after cell seeding ($1x10^5$ cells/cm^2) and incubation in osteogenic medium.

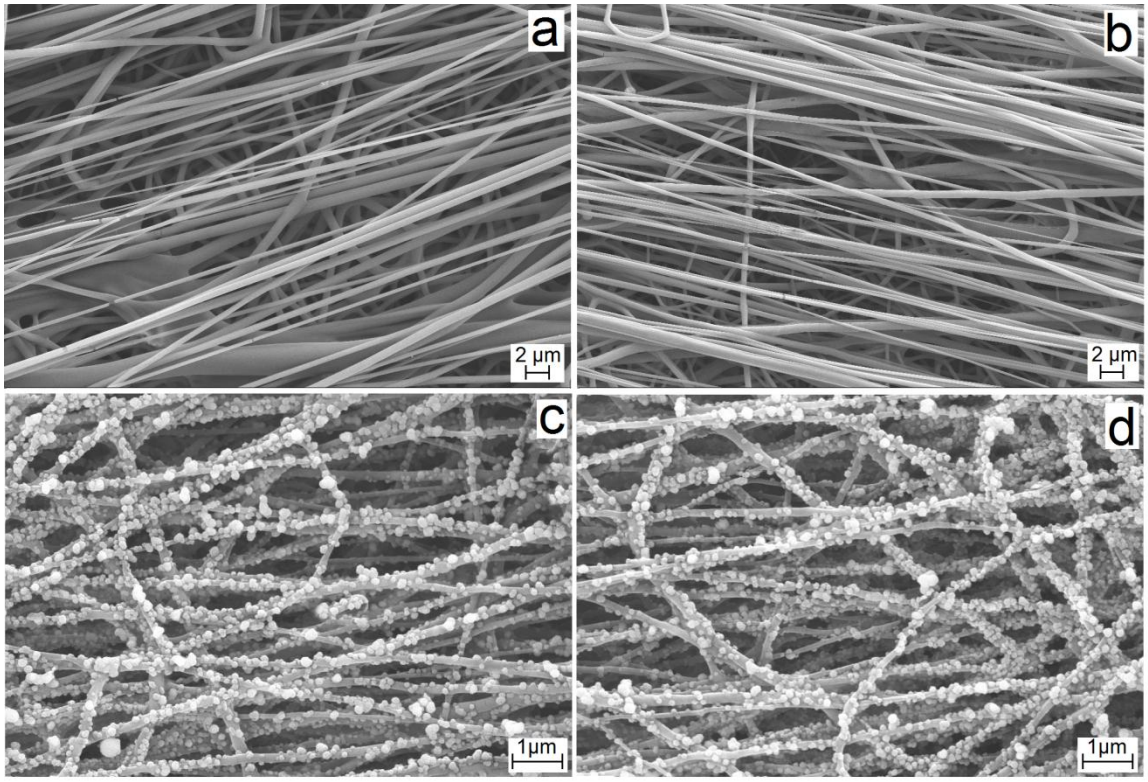

Figure 3.7 SEM images of the microsheets after sterilization with by ultraviolet (UV) radiation followed by immersion in 70% ethanol for 30 min and washing three times with sterile PBS. Images (a) and (b) are PLGA/PLA-GLU microsheets before sterilization and after sterilization procedure. Images (c) and (d) are for PLGA/PLA-GLU microsheets after 24hincubation in m10SBF before sterilization and after sterilization, respectively. Scale bars in (a-b) and (c-f) represent 2 µm and 2 µm, respectively.

DNA content of MSCs cultured on GLU-NF/CaP microsheets is shown in Figure 3.10a. DNA content of GLU-NF/LBL/CaP200-BM (light blue) incubated in basal medium, in the absence of osteogenic differentiation factors, increased slightly with incubation time while those incubated in osteogenic medium decreased significantly with time. The cell density for CaP deposited microsheets on day 7 was significantly higher than that of GLU-NF, as indicated by a star in Figure 3.10a, consistent with previous

results for cell adhesion on mineralized nanofibers [116]. Cell number results suggested that the CaP deposited microsheets did not have a toxic effect on the seeded cells and the decrease in DNA content of MSC-seeded microsheets incubated in osteogenic medium was related to cell differentiation or the initial seeding density (see Discussion).

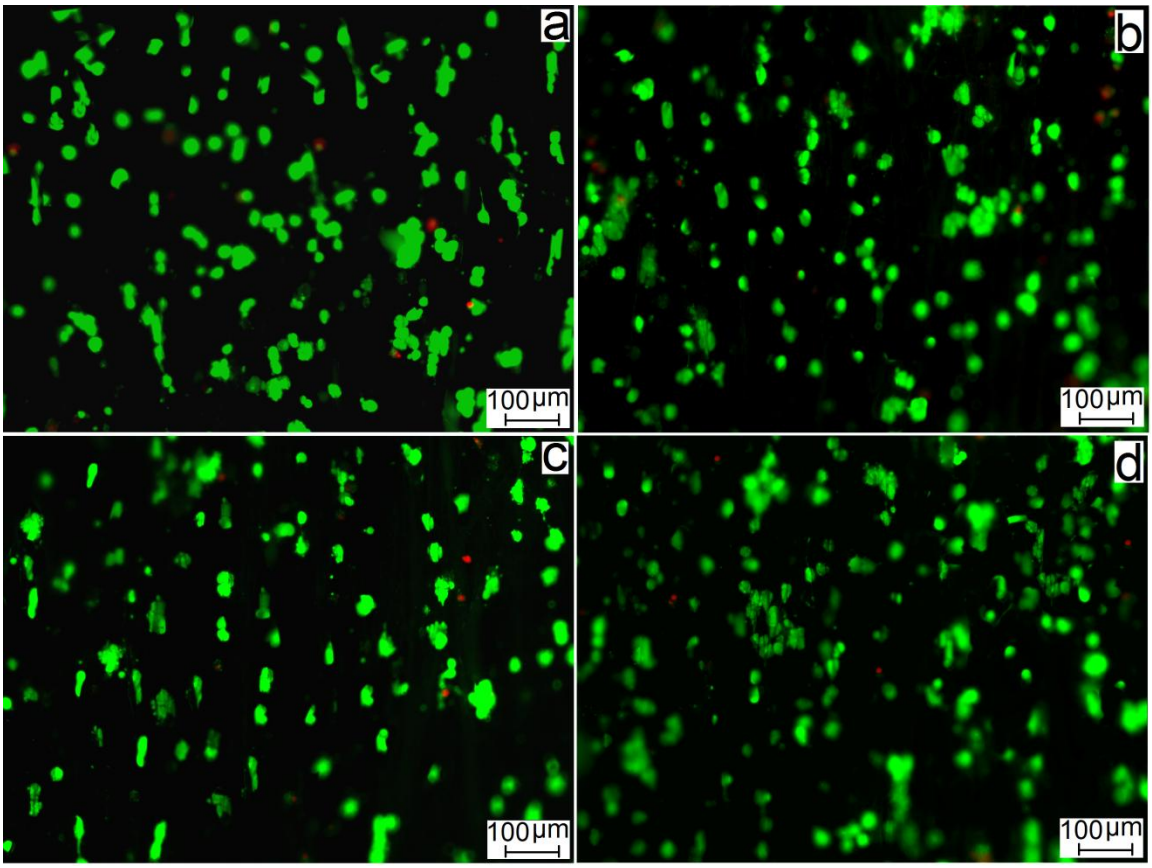

Figure 3.8 Live (green) and dead (red) image of MSCs (1500 cells/cm^2 initial density) seeded on GLU-NF (a), GLU-NF/CaP30 (b), GLU-NF/CaP50 (c), and GLU-NF/LBL/CaP200 (d) microsheets after two days of incubation in osteogenic medium (scale bar is 100 µm).

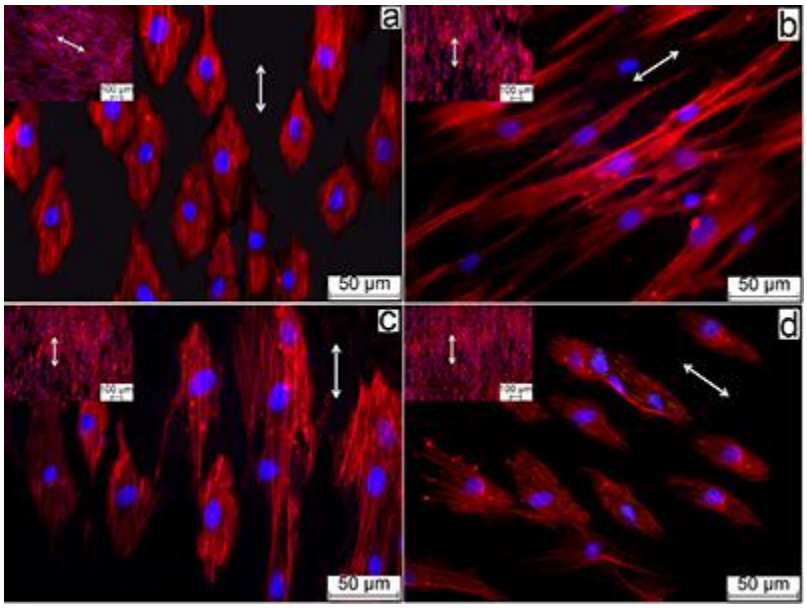

Figure 3.9 Morphology of MSCs (1500 cells/cm^2 initial density) seeded on GLU-NF (a), GLU-NF/CaP30 (b), GLU-NF/CaP50 (c), and GLU-NF/LBL/CaP200 (d) microsheets after two days of incubation in osteogenic medium (scale bar is 50 µm). The inset in each image shows the corresponding image of MSCs seeded on GLU-NF microsheets at 1x10^5 cells/cm^2 density after 7 days of incubation in osteogenic medium (scale bar in the insets is 100 µm). In the images, cell nuclei and cytoskeletal actin are stained with DAPI (blue) and phalloidin (red), respectively. The arrow in the images shows direction of the aligned nanofibers.

ALPase activity of MSCs seeded on GLU-NF/CaP microsheets is shown in Figure 3.10b. ALPase activity of MSCs seeded on GLU-NF/LBL/CaP200-BM microsheets incubated in basal medium did not increase with time (light blue curve). ALPase activity of all other groups, incubated in osteogenic medium, peaked after 14 days and returned to baseline level at day 28, consistent with previous reports [151]. ALPase activity increased significantly with amount of CaP deposition on the fibers. For example, peak ALPase activity of GLU-NF/CaP30, GLU-NF/CaP50, and GLU-NF/LBL/CaP200 increased from 2400±200 to 3200±600 and 5100±400 IU/mg DNA, respectively, while that of GLU-NF was 1600±100 IU/mg. Mavis and collaborators

reported that MC3T3-E1 pre-osteoblasts seeded on apatite-coated PCL fibers had higher ALPase activity compared to uncoated fibers [123]. Calcium content of MSCs seeded on CaP-deposited microsheets is shown in Figure 3.10c. All calcium measurements were subtracted from the amount at day 4 to remove the calcium due to CaP deposition prior to cell seeding. For all groups, extent of mineralization of the MSCs increased gradually from day 14 to 28 with GLU-NF/LBL/CaP200 having the highest mineralization after 28 days of incubation in osteogenic medium. Mineral content of the MSCs seeded on GLU-NF/LBL/CaP200-BM incubated in basal medium increased slightly with time, which could be related to the osteogenic effect of deposited CaP prior to cell seeding. For example, calcium content of MSC-seeded GLU-NF/LBL/CaP200 microsheets after 28 days was 960±110 mg/mg DNA, while those of GLU-NF/LBL/CaP200-BM, GLU-NF, GLU-NF/CaP30, and GLU-NF/CaP50 were 130±20, 460±40, 580±40, and 760±80 mg/mg DNA, respectively.

Expression of osteogenic markers OP, ALPase, OC, Col-1, and vasculogenic markers Pecam-1 and Flk-1 with incubation time for MSC-seeded GLU-NF/CaP microsheets is shown in Figures 3.11a through 3.11f, respectively. For GLU-NF/LBL/CaP200-BM control group incubated in basal medium, expression of OP, ALPase, OC, Pecam-1, and Flk-1 did not change significantly with time, while there was a significant increase in Col-1 expression. However, the increase was significantly less than those microsheets incubated in osteogenic medium (see Figure 3.11d). ALPase mRNA expressions for all groups followed their corresponding ALPase activity shown in Figure 3.10b, peaking at day 14 and returning to baseline level at day 28 [152]. mRNA expression of OP, OC, and Col-1 increased gradually with incubation time. Expression of

osteogenic marker OP was was highest for GLU-NF/LBL/CaP200, as shown in Figure 3.11a. For example, OP expression of GLU-NF/LBL/CaP200 at day 28 was 68±4 while those of GLU-NF, GLU-NF/CaP30, and GLU-NF/CaP50 was 16±2 and 25±3, 48±3, respectively. Expression of osteogenic markers OC and Col-1 followed a similar trend with GLU-NF/LBL/CaP200 having the highest expression (420±30). For example, OC expression of GLU-NF, GLU-NF/CaP30, GLU-NF/CaP50, and GLU-NF/LBL/CaP200 at day 28 was 180±10, 250±30, 300±20, and 420±30, respectively, while that of Col-1 was 6±1, 11±2, 14±1, and 16±1. Expression of Pecam-1 and Flk-1 of the MSCs did not change significantly with incubation time and CaP deposition, which indicated that CaP deposition on the fibers mainly affected osteogenic expression. Pecam-1 and Flk-1 expression for GLU-NF/LBL/CaP200 was slightly higher than the other groups at day 28 (see Figures 3.11e and 3.11f).

Figure 3.12 shows immunostained images of MSCs seeded on GLU-NF/CaP microsheets. Columns a through c in Figure 3.12 are for OC (red), OP (green), and Pecam-1 (red), respectively, and rows 1-5 are for GLU-NF/LBL/CaP200-BM incubated in basal medium as negative control, GLU-NF, GLU-NF/CaP30, GLU-NF/CaP50 and GLU-NF/LBL/CaP200 after 28 days of incubation in osteogenic medium. GLU-NF/LBL/CaP200-BM did not stain for OC, OP, or Pecam-1 markers (see first row). GLU-NF group showed weak staining for all three markers while the CaP deposited GLU-NF groups showed moderate to strong staining for osteogenic markers OC and OP. There was a slight increase in Pecam-1 staining for GLU-NF/LBL/CaP200 group, consistent with the slight increase in mRNA expression in Figure 3.11e. Overall, GLU-NF/LBL/CaP200 group showed highest staining for OC, OP, and Pecam-1. Taken

together, results in Figures 3.10-3.12 demonstrate that the extent of osteogenic differentiation of MSCs seeded on GLU-NF microsheets depended strongly on the amount of deposited CaP on the fibers prior to cell seeding.

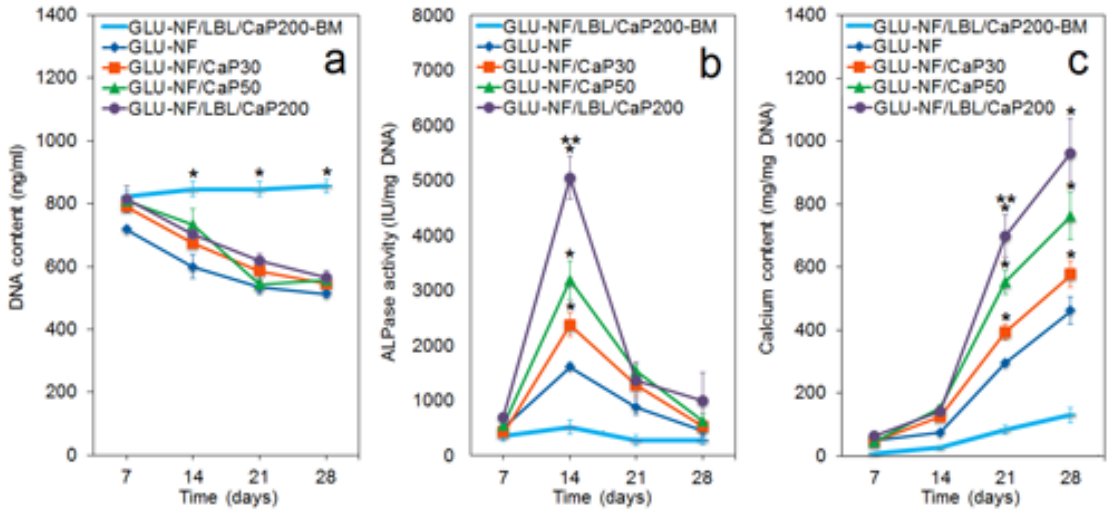

Figure 3.10 DNA content (a), ALPase activity (b), and calcium content (c) of MSCs seeded on GLU-NF/CaP microsheets and incubated in osteogenic medium for up to 28 days. Experimental groups include GLU-NF without incubation in m10SBF (control, blue), GLU-NF/CaP30 (red), GLU-NF/CaP50 (green), and GLU-NF/LBL/CaP200 (purple) incubated in osteogenic medium. GLU-NF/LBL/CaP200-BM group was incubated in basal medium as the negative control (light blue). In the figures, one star indicates statistically significant difference (s.d.; $p<0.05$) between the test group and GLU-NF for the same time point; two stars between the test time point and the previous time in the same group; three stars between GLU-NF/LBL/CaP200 and other GLU-NF/CaP groups for the same time point. Error bars correspond to means ± 1 SD for n = 3.

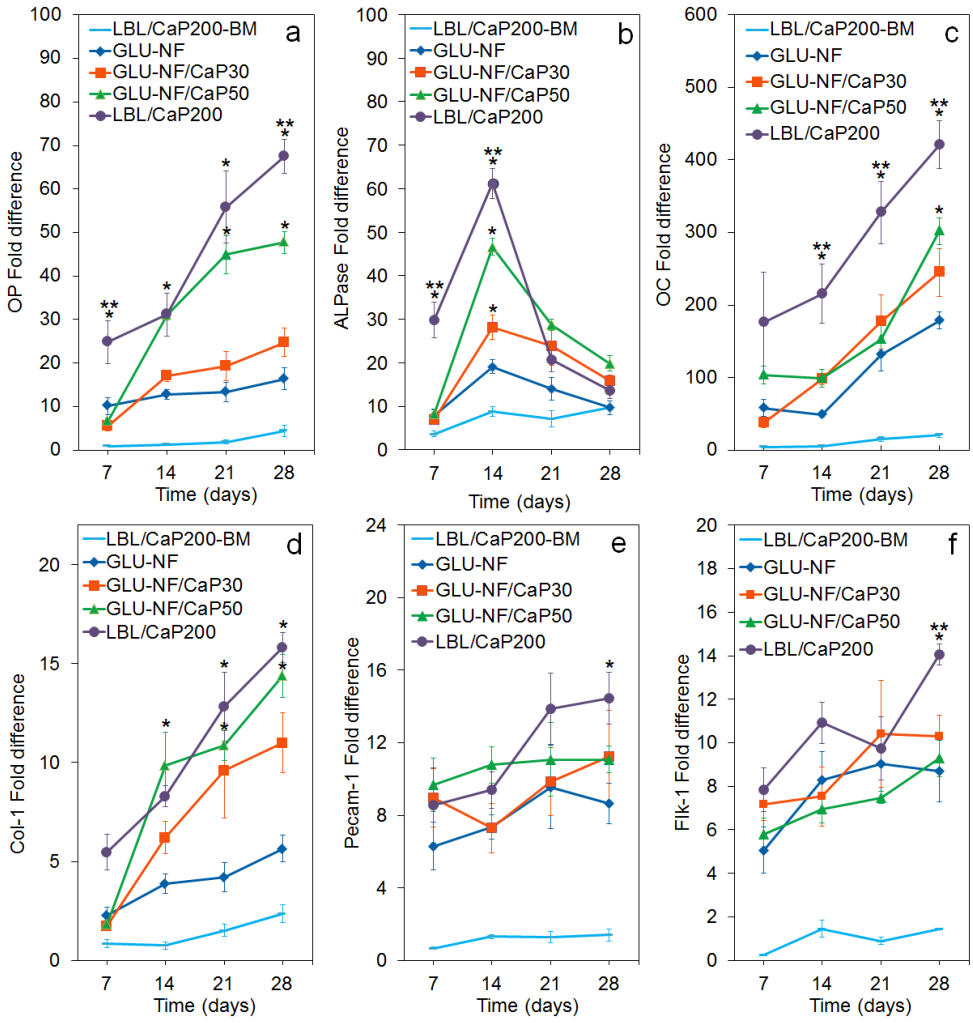

Figure 3.11 mRNA expression levels (as fold difference) of osteopontin (a, OP), alkaline phosphatase (b, ALPase), osteocalcin (c, OC), collagen type-1 (d, Col-1), platelet endothelial cell adhesion molecule (e, Pecam-1), and Flk-1 (f) for MSCs seeded on GLU-NF/CaP microsheets and incubated in osteogenic medium for up to 28 days. Experimental groups include GLU-NF without incubation in m10SBF (blue), GLU-NF/CaP30 (red), GLU-NF/CaP50 (green), and GLU-NF/LBL/CaP200 (purple). GLU-NF/LBL/CaP200-BM group was incubated in basal medium as the negative control (light blue). In the figures, one star indicates statistically significant difference (s.d.; $p<0.05$) between the test group and GLU-NF for the same time point; two stars between the test time point and the previous time in the same group; three stars between GLU-NF/LBL/CaP200 and other GLU-NF/CaP groups for the same time point. Error bars correspond to means ± 1 SD for n = 3.

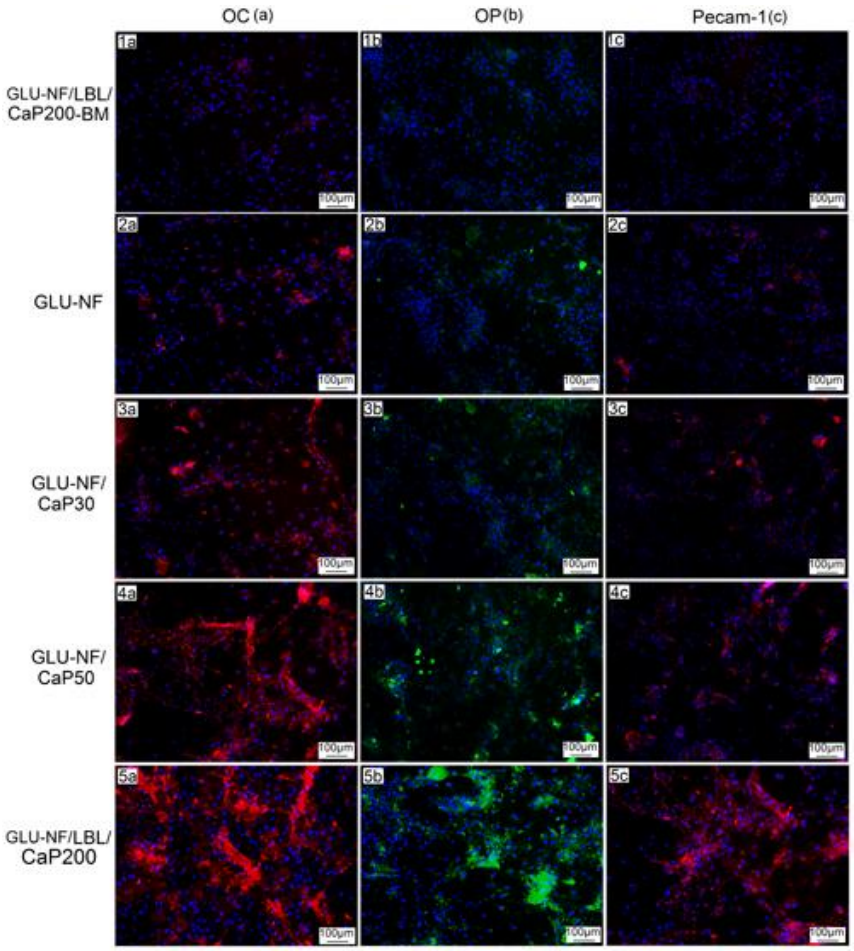

Figure 3.12 Expression pattern of osteogenic markers osteocalcin (a, OC, red, first column), osteopontin (b, OP, green, second column), and vasculogenic marker Pecam-1 (c, red, third column) for MSCs seeded on GLU-NF/CaP microsheets after 28 days incubation in osteogenic medium. Experimental groups include GLU-NF without incubation in m10SBF (control), GLU-NF/CaP30, GLU-NF/CaP50, and GLU-NF/LBL/CaP200. Expression pattern of MSCs in GLU-NF/LBL/CaP200-BM negative control group, which was incubated in basal medium, is shown in the first row. Cell nuclei in the images are stained with DAPI (blue).

3.5 DISCUSSION

The simulated percentage of GLU groups on the fiber surface was >80%. Although diameter of the simulated fibers was significantly less than the actual fiber diameter, simulation results indicated that a major fraction of GLU peptides localized to the fiber surface. Consistent with simulation results, Gentsch and collaborators

functionalized PLGA electrospun nanofibers by blending with poly(lactic acid)-block-CGGRGDS conjugate and reported a decrease in water contact angle on the fiber surface with increasing concentration of the conjugate [153]. It should be noted that the simulations were performed in the absence of electric field, thus the actual GLU percentages on the fiber surface may be higher than the predicted values. Sun and collaborators used the electric field applied during electrospinning to induce segregation of peptides to the fiber surface with poly(ethylene oxide)-peptide conjugates [154]. The simulation results taken together with contact angle measurements in Figure 3.6a and fluorescence measurements of FITC labeled PLA-GLUK fibers in Figure 3.2b provide evidence for localization of a significant fraction of PLA-GLU to the fiber surface when blended with PLGA, to serve as nucleating sites for CaP deposition.

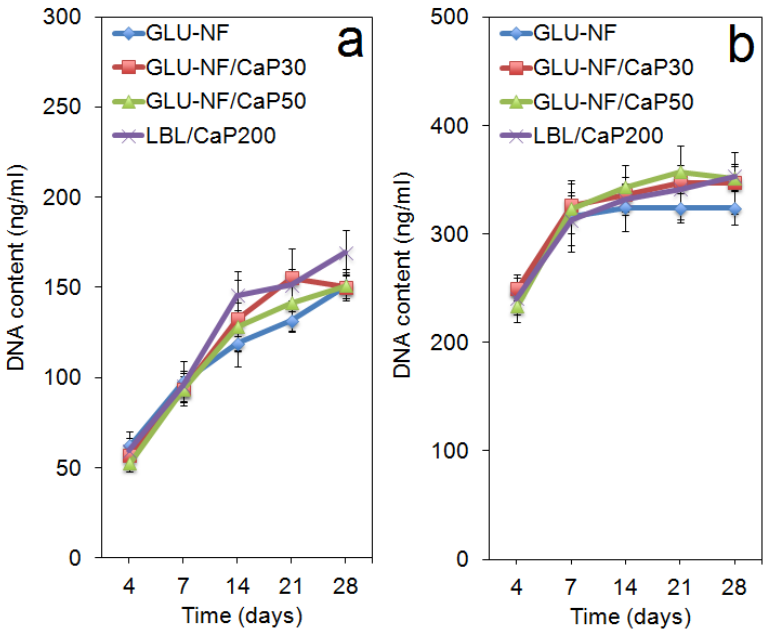

Figure 3.13 The effect of initial seeding densities of $3x10^3$ (a) and $2.5x10^4$ cells/cm^2 (b) on the microsheets on DNA content with incubation time in osteogenic medium.

Conjugation of GLU sequence reduced water contact angle on the fiber surface, as shown in Figure 3.6a-c, with zero contact angle after CaP deposition on the fibers. The finite water contact angle of <90° on GLU-NF fibers allowed nucleation and growth of CaP crystals on layers near the fiber surface but it limited penetration of water, calcium, and phosphate ions inside the microsheets. Consequently, when incubation time of GLU-NF microsheets in m10SBF was increased from 24 to 48 h, there was little change in CaP content and tensile modulus (data not shown). When the LBL approach was used to produce CaP-deposited microsheets, there was a dramatic increase in CaP content from 50±6 to 200±5%, as shown in Figure 3.6d, indicating that CaP nucleation and growth on GLU-NF fibers was controlled by diffusion of calcium/phosphate ions from the medium to inside the microsheets. It should be noted that the CaP content of LBL microsheets was between those of cancellous (160%) and cortical (310%) bone [155, 156] demonstrating that CaP contents as high as that of cortical bone can be achieved by reducing layer thickness. The LBL approach has been used to increase filler loading and stiffness of composites or fabricate highly ductile oppositely charged multilayered films [157, 158]. Li and collaborators observed increased CaP deposition on PCL microfibers by increasing the density of carboxylic acid groups on the surface by plasma treatment [159]. They also observed that CaP deposition increased by coating the surface of PCL microfibers with gelatin, presumably due to the carboxylic acid content of gelatin [87]. Our work demonstrates for the first time that the extent of CaP nucleation and growth on synthetic fibers, and in turn the fiber mechanical strength, can be controlled by incubation time in SBF or by GLU density on the fiber surface.

The tensile modulus and toughness of the microsheets dramatically increased with higher CaP contents of 50 and 200%, as shown in Figures 3.6e and 3.6f, respectively. Zhang *et al.* reported a decrease in tensile strength and elastic modulus of chitosan composite microfibers with the addition of HA nanocrystals (nHA) and collagen to the electrospinning solution [89]. Our results indicate that fiber size, CaP crystal size, and nucleation and growth of CaP crystals on the fiber surface contribute to the higher modulus and toughness of the microsheets. The GLU peptide initiateed nucleation of CaP crystals on the fiber surface. The nucleated CaP crystals continue to grow with incubation time and start to merge and fuse to form a network of fibers cross-linked with CaP crystals. We speculate that the higher toughness and modulus of microsheets with 50 and 200% CaP content is related to the formation of CaP cross-linked network of fibers.

DNA content of the MSCs seeded on GLU-NF/LBL/CaP200 microsheets incubated in osteogenic medium decreased significantly with time, as shown in Figure 3.10a. However, the slight increase in DNA content of MSCs on GLU-NF/LBL/CaP200 microsheets incubated in basal medium (light blue in Figure 3.10a) indicated that the microsheets did not have toxic effect on the seeded cells. We speculated that the decrease in cell number with incubation time in osteogenic medium was related to cell differentiation as well as the initial cell seeding density. The effect of initial seeding densities of $3x10^3$ and $2.5x10^4$ cells/cm^2 on the microsheets on DNA content with incubation time in osteogenic medium is shown in Figures 3.13a and 3.13b, respectively. At relatively low initial density of 3000 cells/cm^2 (Figure 3.13a), DNA content of the MSCs on the microsheets increased significantly for all time points in osteogenic medium and DNA content was relatively independent of the extent of CaP deposition prior to cell

seeding. As the initial cell density was increased to $2.5x10^4$ cells/cm^2 (Figure 3.13b), DNA content increased in the first 7 days and then remained relatively constant (or increased slightly) for times between 7 and 28 days as the cells differentiated in osteogenic medium. With further increase in initial cell density to $1x10^5$ cells/cm^2 (Figure 6a), DNA content of the MSCs on the microsheets decreased significantly for all time points with incubation in osteogenic medium, but remained relatively unchanged in basal medium (light blue curve in Figure 3.10a). Images of live and dead MSCs two days after cell seeding on the microsheets, displayed in Figure 3.8, show >90% cell viability two days after seeding in osteogenic medium, implying that the microsheets did not have a significant toxic effect on the seeded cells. The other possible reason for the decrease on DNA content might be the increasing cell surface area after cell adhesion and spread on the apatite nucleated aligned nanofibers. Figure 9 clearly shows that cells were completely spread along the fibers even after 7 days of culture in osteogenic media. The required surface area for proliferated cells adhesion is limited after cells completely cover the surface of the aligned nanofibers. Therefore, the proliferation slows down and the death of unattached cells becomes dominant due to the limited surface area. Taken together, these results demonstrate that the change in DNA content of the MSCs seeded on the microsheets with incubation time depended on the initial cell seeding density, culture medium (osteogenic versus basal medium) and increase on the cell surface area after spreading on the fibers. Kim et al. investigated the effect of initial cell seeding density on poly(propylene fumarate) substrates on osteogenic expression of rat MSCs [160]. They reported higher level of mineralization and osteocalcin expression at higher cell densities of $7.5x10^4$ and $1.5x10^5$ cells/cm^2. Zhou et al. investigated osteogenic

differentiation of umbilical cord stem cells on fiber-reinforced calcium phosphate scaffolds [161]. They reported increased osteogenic differentiation and mineral deposition on the scaffolds with increasing cell density from $1.5x10^4$ to $1x10^5$ cells/cm^2. It appears that cell-cell contact plays a significant role in osteogenic differentiation of MSCs and other stem cells. Based on previous results, a relatively high seeding density of $1x10^5$ cells/cm^2 was used to investigate osteognic differentiation of rat MSCs on GLU-NF microsheets.

Biochemical, mRNA, and immunocytochemical results show that the extent of osteogenic differentiation and maturation of MSCs seeded on the microsheets increased with CaP deposition. This increase can be explained by the higher modulus as well as higher CaP content of GLU-NF microsheets prior to cell seeding.

These findings are consistent with prior results that matrix stiffness directs stem cell differentiation [162] and CaP content of the substrate affects osteogenesis [163]. Chaterjee *et al.* reported that ALPase activity and extent of mineralization of osteoblasts encapsulated in a polyethylene glycol hydrogel was modulated by matrix stiffness with 400-fold increase in mineralized volume fraction as the matrix stiffness increased by 30 fold [164]. Engler *et al.* demonstrated that MSCs seeded on stiffest gel matrices (34 kPa elastic modulus) showed 4-fold greater osteocalcin and the early transcriptional factor CBFa1 expression [165]. Lee *et al.* and Chen *et al.* observed an increase in ALPase activity and extent of mineralization of MSCs seeded on PCL/nHA nanofibers with HA content [116, 166]. Similarly, a significant increase in ALPase activity with HA addition was reported for MC3T3-E1 preosteoblasts seeded on PCL or PLLA fibers [88, 123, 167]. Zhang *et al.* on the other hand did not observe an increase in osteogenic

differentiation of human fetal osteoblasts seeded on chitosan fibers with HA addition to the electrospinning solution [89]. Our results show that osteogenic differentiation of MSCs depends directly on the extent of CaP deposition on the nanofibers prior to cell seeding. The extent of osteogenic differentiation of MSCs may also depend on the connectivity of crystals with increasing CaP deposition. Bhumiratana et al. investigated nucleation and growth of mineralized matrix on silk-hydroxyapatite (HA) composite scaffolds seeded with human MSCs [168]. He reported that the initial HA content and its distribution acted as nucleation sites for new mineral formation, which in turn affected the connectivity of mineral deposition by MSCs. Although the effect of substrate modulus and CaP content on differentiation and mineralization MSCs has been studied extensively, there has been very few reports on the effect of CaP connectivity on the extent of mineralization by MSCs.

The findings of this work demonstrate that GLU conjugation coupled with an LBL approach dramatically increase nucleation and growth of apatite-like nanocrystals on the surface of nanofibers, leading to CaP to fiber ratios >200%, tensile moduli close to 1 GPa, and higher osteogenic differentiation of MSCs. CaP content of the nanofibers can be further increased to reach that of cortical bone by reducing the thickness of individual fiber layers in the LBL approach or by reducing porosity of the fiber sheets. The CaP deposited GLU-NF composites are potentially useful as a biomimetic matrix in regeneration of skeletal tissues.

3.6 CONCLUSION

In this work, the effect of calcium phosphate (CaP) deposition on aligned nanofibers surface-modified with EEGGC glutamic acid peptide on osteogenic

differentiation of rat marrow stromal cells was investigated. In an effort to increase CaP to fiber ratio, a layer-by-layer approach was used to improve the diffusion of calcium and phosphate ions inside the microsheets. Based on Dissipative Particle Dynamics simulation of PLGA/PLA-GLU fibers, >80% of GLU peptide was localized to the fiber surface. X-ray diffraction results showed the characteristic apatite peaks in CaP crystals grown on GLU-NF microsheets. CaP to fiber ratio of the microsheets increased from 50% for a single fiber layer to 200% for the LBL microsheet with the same overall thickness when incubated in a modified SBF medium. Tensile modulus increased from 550 MPa for a single fiber layer to 880 MPa for the LBL microsheet. MSCs seeded on GLU-NF microsheets after CaP deposition spread along the direction of fiber alignment, irrespective of the extent of CaP deposition. Osteogenic differentiation of MSCs seeded on GLU-NF microsheets increased significantly with CaP deposition on the fibers prior to cell seeding. For example, peak ALPase activity increased from 1600 IU/mg DNA for GLU-NF without CaP deposition to 5200 IU/mg DNA for CaP-deposited LBL microsheet, and calcium content after 28 days increased from 460 to 960 mg/mg DNA. Expression of osteogenic markers OP, ALPase, OC, and Col-1 increased gradually with increasing CaP deposition on GLU-NF microsheets. The findings of this work demonstrate that surface modification of nanofibers with GLU peptide by blending PLGA with PLA-GLU dramatically affects nucleation and growth of calcium phosphate crystals leading to increased osteogenic differentiation of MSCs and mineralization.

CHAPTER 4 OSTEOGENIC DIFFERENTIATION OF MARROW STROMAL CELLS IN OSTEON-MIMETIC MINERALIZED NANOFIBROUS MICROTUBES

Ozan Karaman and Esmaiel Jabbari. Osteogenic Differentiation of Marrow Stromal Cells (MSCs) in Osteon-mimetic Mineralized Nanofibrous Microtubes. To be submitted to Advanced Functional Materials.

CHAPTER 4

OSTEOGENIC DIFFERENTIATION OF MARROW STROMAL CELLS IN OSTEON-MIMETIC MINERALIZED NANOFIBROUS MICROTUBES

4.1 INTRODUCTION

Cranial, maxillofacial, oral fractures and large bone defects are currently being treated by using auto- and allografts. These techniques have limitations in the clinical usage such as immune response, donor-site morbidity, and lack of availability [1, 3, 169]. Therefore, the interest on tissue engineering applications for bone graft procedures has rapidly been growing. Tissue engineering approach requires a cell supporting scaffold in order to maintain a 3- dimensional substrate for cells to function during the formation of bone tissue [5, 6]. Electrospinning has been widely used to fabricate nanofibrous matrices to mimic the morphology of the collagen fibers in the bone extracellular matrix [16, 170]. Since electrospun nanofibers provide a large surface-to-volume ratio and mimic the natural extracellular matrix of bone tissue, it has been found to be a suitable scaffold for bone tissue engineering [18, 19]. Nanofibers has been fabricated from natural biopolymers, like collagen and chitosan, or synthetic polymers such as poly(L-lactide) (PLLA) and poly(ε-caprolactone) (PCL)[78, 87-89]. Due to the low mechanical properties of NFs, composite nanfibrous scaffolds with calcium-phosphate(CaP) crystals can provide adequate mechanical properties and support for cell attachment, proliferation, and differentiation of mesenchymal stem cells[116, 171]. Nucleation of CaP nanocrystals

on collagen fibers in the bone matrix is mediated by ECM non-collagenous proteins such as bone sialoprotein (BSP), osteonectin (ON), osteopontin (OP), and osteocalcin (OC).[124, 172, 173] Glutamic acid (GLU) sequences ranging from 2-10 residues in those proteins regulate nucleation and growth of CaP crystals on collagen fibers [124]. Therefore, 2mer GLU was conjugated on the PLGA nanofiber microsheets to induce CaP nucleation. In addition, a layer-by-layer approach was used to improve the diffusion of calcium and phosphate ions inside the microsheets in order to achieve a high CaP to fiber ratio.

The cortical bone composed of osteons that have microtubular structures with a central vascular channel inside for ensuring suitable nutrient/waste transport to the bone tissue [11]. Laminated multilayers of CaP deposited collagen fibers forms the osteon microtubes. Therefore, engineered bone grafts that can mimic the microstructure of bone would be a strong candidate for bone tissue engineering applications. The physical configuration of the scaffolds, which mediate the cell-cell and cell-scaffold interactions, exert strong influence on the success of osteogenic processes in vitro [174, 175]. The success of engineered scaffold mostly depends on how closely the cell-scaffold relationship mimics that natural tissue in vivo. Both in vitro and in vivo studies have demonstrated the organic/inorganic composite fibrous scaffolds support attachment, differentiation, and proliferation of osteoblasts or mesenchymal stem cells (MSCs) and facilitate bone healing [116]. However, investigations regarding the effect of osteon-mimetic tubular scaffolds size (inner diameter) with 3-D morphology on osteogenic differentiation of MSCs are still limited. To this end, we hypothesized that three dimensional structure of microtubes with well-defined pores could potentially mimic the

microstructure of osteons in cortical bone and induce osteogenesis of MSCs. In order to test this hypothesis, we investigated the osteogenic differentiation potential of MSCs when seeded into different diameter microtubes engineered from CaP deposited aligned nanofiber microsheets that have an array of macropores to enhance diffusion of nutrients. The microtube structure fabricated by wrapping perforated microsheets around the stainless steel needles upon annealing above glass transation temperature (T_g) of PLGA. The effect of tubular formation and the inner diameter of CaP deposited microsheets on osteogenic differentiation of rat MSCs was investigated by cytochemicalanalysis. Our results indicate that the 3-D microtubes provide a promising microenvironment that enhances osteogenesis. However, changing the inner diameter of the osteon-mimetic microtubes did not change the cytochemical analysis significantly.

4.2 MATERIALS AND METHODS

4.2.1 FABRICATION OF MINERALIZED GLUTAMIC ACID TEMPLATED PEPTIDE CONJUGATED PLGA NANOFIBERS MICROSHEETS AND MICROTUBES

The CaP nucleated microsheets in Chapter 3 were used for fabricating the osteon-mimetic microtubes. Beriefly, the EEGGC peptide was synthesized manually on Rink Amide NovaGel^{TM} resins as described [100, 125, 126]. Briefly, rink amide NovaGel^{TM} resin (100g) was incubated in DMF (3 ml) for 30 min to swell completely. Then, the resin was washed with DMF (2×3 ml). Fmoc-protected amino acid derivative (6 eq.) and HOBt (12 eq.) were dissolved in dry DMF (3 ml). Next, DIC (6.6 eq.) as an accelerator was added to the mixture. Then, the resulting mixture was shaken 5-10 min and added to the resins. Next, 0.2 ml DMAP (0.05 M) was added to the mixture. The mixture was placed in an orbit shaker for 4-6 hr at 30°C. The reaction was tested using Kaiser reagents. If the

test result was positive, the above coupling reaction would be repeated until a negative result was reached. After the reaction, the resins were washed with DMF (5×3 ml) and treated with 20% piperidine in DMF for 2 × 15 min in order to deprotect the F-moc groups of the amino acids. The subsequent amino acids were coupled using the same method. After peptide chain elongation, the resins were washed with 5 × DMF and 5 × DCM. The EEGGC peptide was cleaved from the resin by treating with 95% TFA/2.5% TIPS/2.5% water and precipitated in cold ether. After drying, the EEGGC peptide was conjugated to poly (lactide) acrylate (PLAA, MW=4000 Da) macromer by Michael's addition reaction between the acrylate group on the macromer and the cysteine's sulfhydryl group on the peptide to produce a PLAA-EEGGC conjugate. A mixture of the peptide and PLAA macromer (2:1 molar ratio) was dissolved in a 1:1 mixture of DMF:water, and allowed to react at 30°C overnight in an orbital shaker. The mixture was dialyzed against DI water and lyophilized to obtain the dry product.

Electrospinning solutions of high molecular weight PLGA (10 wt%) and mixtures of PLAA conjugated EEGGC peptide (1.5% of PLGA amount) were prepared in hexafluoro-2-propanol (HFIP). A programmable KDS100 syringe pump (KD Scientific, Holliston, MA) was used to pump the polymer solution, which was inside a 1 ml syringe (Norm-Ject, Henke Sass Wolf GmbH, Tuttingen, Germany) to the end of a 21 GTW needle (PrecisionGlide, 0.81 mm O.D., Becton-Dickinson, Franklin, NJ) at a specified flow rate of 1.0 ml/h. The 20 kV positively charged Pt electrode of a high voltage supply (ES40P-5W/DAM, Gamma High Voltage Research) was connected to the needle. A high-speed rotational wheel collector (custom built in the Machine Shop at University of South Carolina) was used to prepare glutamic acid template aligned nanofiber

microsheets (GLU-NF). A grounded aluminum wheel (20 cm diameter and 5 mm thickness) powered by a high speed DC motor (2M0578, up to 5000 rpm, Dayton Electric, Niles, IL) was used to collect nanofibers and placed at 7.5 cm underneath the needle. The force generated by the high electric field between the needle and the rotating wheel overcame the surface tension of the polymer solution and stretched the accelerating jet as fibers toward the collector while the solvent evaporated during the process. The polymer jet, after deposition on the collector, was further stretched by the tangential force produced by the rotation of the wheel and formed aligned fibers on the edge of the wheel.

Mineralization of nanofiber microsheets was occurred by depositing the apatite crystals on nanofiber microsheets via using Lie et al.'s modified 10-fold-concentrated simulated body fluid (m10SBF(1). Briefly, the stock solution of 10SBF was prepared by dissolving NaCl, KCl, $CaCl_2 \bullet H_2O$, $MgCl_2 \bullet 6H_2O$ and NaH_2PO_4 in distilled deionized (DDI) water (10SBF stock solution pH=4.2). Next, in order to reach physiological pH of 7.4, 60 mM of $NaHCO_3$ was dissolved in the 10SBF stock solution prior to mineralization process. The impurities and formed large CaP crystals in the pH range of 5.9 to 7.4 were removed by filtering the solution through a 0.22 μm pore size filter system. Nanofiber microsheets were then immersed in m10SBF filled plastic beaker and kept at room temperature for 6h and 24h. The m10SBF was replaced with fresh m10SBF every 6 h over apatite growth cycle. After removal from m10SBF, the nanofiber microsheets were washed with DDI water three times and then dried at room temperature. In the layer-by-layer approach, the first GLU-NF microsheet, approximately 5 μm thick, was electrospun on a 12 mm circular glass coverslip (VWR, Bristol, CT). Next, the microsheet was incubated in m10SBF for the prescribed time, washed with DI, and dried.

After drying, the second GLU-NF layer was electrospun directly on the first layer. The bilayer sheet was incubated in m10SBF for a prescribed time, washed with DI, and dried. This layer-by-layer process was repeated five times to produce a 26±2 μm thick mineralized multilayer GLU-NF circular sheet (12 mm diameter). The multilayer approach improved diffusion of calcium and phosphate ions inside the fiber sheet when incubated in m10SBF solution. Scanning electron microscope (SEM) was used to image the nanofibers microsheets with different CaP content. After coating the samples with gold (Poloron sputter coater, Quorum Technologies, New Haven, UK) at 20 mA for 45 sec, the microsheets was attached to a SEM stub with double-sided conductive tape and imaged with a Field Emission Scanning Electron Microscope (FESEM, Carl Zeiss Microscopy, Hillsboro, OR) at an accelerating voltage of 8kV. SEM images were analyzed with Image J software (National Institutes of Health, Bethesda, MD) to measure the size of the nanofibers and CaP crystals.

CaP nucleated elctrospun microsheets (5 cm length*1 cm witdh) wrapped around the 21 GTW needle (PrecisionGlide, 0.81 mm O.D., Becton-Dickinson, Franklin, NJ) and placed in pre-heated 80 C^o oven for 10 min to anneal the structure of the microsheets and keep it's microtubalar structure by shape memory effect. Prior to wrapping the microsheets around the needle, uniform micropores were created by 29 GTV needle (PrecisionGlide, 0.34 mm O.D., Becton-Dickinson, Franklin, NJ) on the microsheets to induce diffusion of nutrients and oxygen during the cell culture period. Different diameter microtubes were fabricated by using different size of needles by following the explained procedure above. The porosity and density of the CaP nucleated NF microsheets before and after heat treatment were calculated using Eq. (1) and Eq. (2).

The thickness and size of the microsheets were measured using a micrometer caliper (VWR, Atlanta, GA). The tensile modulus of the samples before and after heat treatment was measured with a Rheometrics Dynamic Mechanical Analyzer (RSA III DMA, Piscataway, NJ) with a strain rate of 0.033/s. Samples were cut to dimensions of 20x5 mm and mounted in the standard vertical clamps of the DMA. The maximum allowed strain was set at 160% and measurements were made at ambient conditions. The thickness and width of the samples were measured with a micro-caliper (Mitutoyo, Aurora, IL). The modulus was calculated as the slope of the linear region of the stress-strain curve.

$$Appeareant\ Density\ \left({}^{mg}/_{mm^3}\right) = \frac{microsheet\ mass\ (mg)}{thickness \times surface\ area\ (mm^2)} \quad (1)$$

$$Porosity\ (\%) = \left(1 - \frac{density\ of\ microsheets\ \left({}^{mg}/_{mm^3}\right)}{density\ of\ PLGA\ \left({}^{mg}/_{mm^3}\right)}\right) \times 100\% \quad (2)$$

MSCs were isolated from the bone marrow of young adult male Wistar rats (6-8 weeks) [93, 100, 125, 176]. Cell isolations were performed under a protocol approved by the Institutional Animal Care and Use Committee of the University of South Carolina. Wistar rats were sacrificed, and femurs and tibias were aseptically removed. The marrow was flushed out with 20 ml of cell isolation medium which consisted of DMEM supplemented with 10% FBS, 100 µg/µL streptomycin, 100 units/mL penicillin, 20 µg/mL fungizone, and 50 µg/mL GS. The cell suspension was centrifuged at 200g for 5 min and the cell pellets were re-suspended in 12 ml of primary medium (DMEM

supplemented with 10% FBS, 100 units/mL penicillin, 100 µg/mL streptomycin, 50 µg/mL GS, and 250 ng/mL fungizone), aliquoted into T-75 flasks and maintained in a humidified 5% CO_2 incubator at 37 °C. Cultures were washed with PBS and replaced with fresh media at 3 and 7 days to remove unattached cells. Cells were rinsed with PBS, enzymatically lifted with 25 µL/cm^2 0.05% trypsin/ 0.53 mM EDTA and centrifuged at 200g for 5 min. The third passage cells were used for cell culture experiments. Cell attachment to the nanofiber mesh was done with undifferentiated MSCs cultured in the primary medium.

MSCs were characterized by immunostaining of specific surface markers. Isolated MSCs were fixed with 4% paraformdehyde for 30 min, permeabilized with 0.1% Triton X-100 and 100 mM glycine in PBS (pH 7.4) for 1 h and blocked with blocking solution including 1.5% BSA and 0.5 mM glycine in PBS for 2 h. The primary antibodies used for MSCs characterization are CD73, CD90, VE-cadherin, and CD-31 (Pecam-1). The primary antibodies diluted in blocking solution for 1:100 and incubated with cells for 12–16 h at 4 °C. Secondary antibodies (Alexa fluor® 488, 593 obtained from Molecular Probes, Invitrogen) were used at 1:100 dilutions in blocking buffer for 2 h at room temperature in the dark. Nuclei were stained with DAPI (4, 6-diamidino-2-phenylindole, 100 ng/ml). Images of the cells visualized using a fluorescence microscope (Zeiss LSM 510 Meta CSLM).

The 0.8 mm and 0.35 mm diameter microtubes were sterilized by ultraviolet radiation for 12 h with a mercury UV lamp (Black-Ray, 365 nm, 100 W; UVP, Upland, CA), followed by immersing in 70% ethanol for 30 min and washing three times with sterile PBS. The microtubes and microsheets were conditioned by immersion in primary

culture media for 1 h prior to cell seeding. Each sample was seeded with 5 µL of the MSCs cell suspension (5 x 10^6 cells/mL) in primary media at 1 x 10^5 cells/cm^2 seeding density by using syringe which has 0.25 mm diameter sterile needle. After 24 h incubation for cell attachment, the media were replaced with osteogenic media (primary media supplemented with 100 nM dexamethasone, 50 µg/mL ascorbic acid, 10 mM ß-glycerophosphate) and cultured in a humidified 5% CO_2 incubator for up to 28 days. MSCs seeded GLU-NF, GLU-NF/CaP30, and GLU-NF/CaP50 microsheets were incubated with 0.16 µM Alexa Fluor® 594 phalloidin (Invitrogen) and 300 nM DAPI for 30 min at ambient conditions to stain the cell actin filaments and nuclei, respectively. The cell morphology on each sample was imaged with a Nikon Eclipse Ti-ε inverted fluorescent microscope.

4.2.2 OSTEOGENIC DIFFERENTIATION OF MSCs SEEDED IN MICROTUBES AND ON MICROSHEETS

At each time point (7, 14, and 28 days), cell-seeded microtubes were washed with serum-free DMEM for 8 h to remove serum components, then washed with PBS, lysed with 10 mM Tris supplemented with 0.2% triton in PBS and used for the measurement of DNA content, ALPase activity, calcium content, and total collagen content. The double-stranded DNA content of the samples was determined by using a Quant-it PicoGreen assay (Invitrogen, Carlsbad, CA) according to the manufacturer's instruction. An aliquot (100 µl) of the working solution was added to 100 µl of the cell lysate and incubated for 4 min at ambient conditions. The fluorescence was measured with a Synergy HT plate reader (Bio-Tek; Winooski, VT) at emission and excitation wavelengths of 485 and 528 nm, respectively. ALPase activity was assessed using a QuantiChrom ALPase Assay Kit

(BioAssay Systems, Hayward, CA) according to the manufacturer's instruction. A 10 µl aliquot of the cell lysate was added to 190 µl of the reagent solution containing 10 mM p-nitrophenyl phosphate and 5 mM magnesium acetate, and the absorbance was recorded at time zero and again after 4min. ALPase activity was calculated using the equation [($A_{t=4}$ – $A_{t=0}$)/ ($A_{calibrator}$ – A_{ddH2O}) x 808] expressed as IU/L. The absorbance was measured on a Synergy HT plate reader at 405 nm. The calcium content was measured using a QuantiChrom Calcium Assay Kit (BioAssay Systems) according to the manufacturer's instruction. A 0.2 ml aliquot of 2 M HCl was added to 0.2 ml of the cell lysate to dissolve the calcium content of the mineralized matrix. Next, a 5 µl aliquot of the supernatant was added to 200 µl of the working solution. After incubation for 3 min, the absorbance was measured with a plate reader at 612 nm. Measured intensities were correlated to equivalent amounts of Ca^{2+} using a calibration curve constructed with calcium chloride solutions of known concentration ranging from 0 to 200 µg/mL. For CaP deposited samples, the measured intensities after incubating with cell lysing solution at day 0 were used as the baseline, and subtracted from the measured intensities at days 7–28. Alkaline phosphatase activity and calcium content were normalized to the DNA amount at specific time point. Collagen production was analyzed by SIRCOL collagen assay kit protocol (Biocolor, Newtownabbey, UK) in the supernatants after 7, 14 and 28 days of cell culture in microtubes. The collagen containing supernatant from the culture was mixed with 1 mL of Sircol dye for 30 min and centrifuged at 10,000 rpm for 5 min to precipitate the collagen–dye complex. After decanting the suspension, pellets were dissolved in 1 mL Sircol alkali reagent and vortexed. Subsequently, 100 µl of the acquired solution was read at 555 nm. The amount of collagen was calculated based on a standard curve of

Sircol Rat Collagen Reference Standard (Biocolor). Cell lysate solution was used as a negative control.

4.3 RESULTS AND DISCUSSION

4.3.1 PROPERTIES OF OSTEON-MIMETIC MICROTUBES

The ideal three dimensional bone tissue engineering scaffolds must be porous enough to support nutrients and oxygen transfer, mimic the micro and nanoscale features of the cortical bone, and composed of biodegradable and biocompatible material [177]. Although numerous different types of three-dimensional scaffolds have been fabricated, none of them completely mimics the micro- and nano structure of the natural bone tissue. For this purpose, in this study we used CaP nucleated PLGA based perforated nanofiber microsheets to fabricate microtubular scaffolds by using heat treatment. In order to enhance porosity of the tubular scaffolds, array of 180 μm diameter perforated holes were made on microtubular scaffolds.

In this study, NF microsheets were fabricated by electrospinning of 10 wt% PLGA concentration, 1.0 μL/h injection rate, 20 kV electric potential, needle-to-wheel distance, wheel diameter, and rotation speed of the wheel 7.5 cm, 20 cm, and 1200 rpm, respectively [93, 173, 178]. The solution concentration (viscosity) has a major effect on NF morphology. For example, we have previously shown that the minimum polymer concentration to produce bead-free fibers, in HFIP was 9 wt.% [93]. Below that critical concentration, surface tension breaks the accelerating jet of fibers into droplets. Morphological structure of GLU-NF in this work indicates that formed NF have diameters similar to collagen fibers (50-500 nm), a major bone extracellular matrix component [119]. It was reported that nanofibrous scaffolds enhanced osteogenic

differentiation. For example, Smith et al. compared the osteogenic ability of nanofibrous matrix to solid films by seeding mouse embryonic stem cells and culturing in osteogenic media for 26 days. They showed significantly higher osteocalcin and bone sialoprotein expression on the nanofibrous matrix compared to those on the solid films [179]. In addition, Hu et al. cultured MC3T3-E1 cells on flat and nanofibrous PLLA films to test the ability of the matrix to support osteogenesis. They demonstrated that the cells on the nanofibrous showed higher levels of osteocalcin and bone sialoprotein expression compared to flat films after 6 days [180].

In our previous study (Chapter 3), the calcium and phosphate crystals content of GLU-NF microsheets after incubation in mSBF at different time points were measured. The results shows that 30% (GLU-NF/CaP30), 50% (GLU-NF/CaP50) and 200% (LBL/CaP200) CaP content based on the CaP to fiber weight ratio were fabricated after incubation GLU-NF microsshets in mSBF for 6h and 24h, respectively (Chapter 3). The SEM images of GLU-NF (a), GLU-NF/CaP30 (b), GLU-NF/CaP50 (c), and LBL/CaP200 microsheets are shown in Figure 4.1, respectively. CaP crystals nucleated from the fiber surface after 6 h incubation can be seen in Figure 4.1b. As incubation time increased to 24 h, the amount of CaP crystals increased significantly, as shown in Figures 4.1c, respectively. Figure 4.1d shows CaP nucleated nanofibers by layer-by-layer application, as it is seen in the image the content of CaP crystals with the average size of 100 nm increased significantly with layer-by-layer method (The procedure for fabrication of LBL-CaP200 microsheets is explained in Chapter 3.2). We have shown that, LBL approach resulted with a dramatic increase in CaP content from 50±6 to 200±5%, indicating that CaP nucleation and growth on GLU-NF fibers was controlled by diffusion

of calcium/phosphate ions from the medium to inside the microsheets. The image of GLU-NF microsheets before and after heat treatment is shown in Figure 4.2a and Figure 4.2b, respectively. The average size of the microsheets before and after heat treatment was 8.7x10.7x0.05 mm, 9.7x13.2x0.04 mm, respectively. The heat treatment resulted with the significantly shrinkage of the nanofiber microsheets.

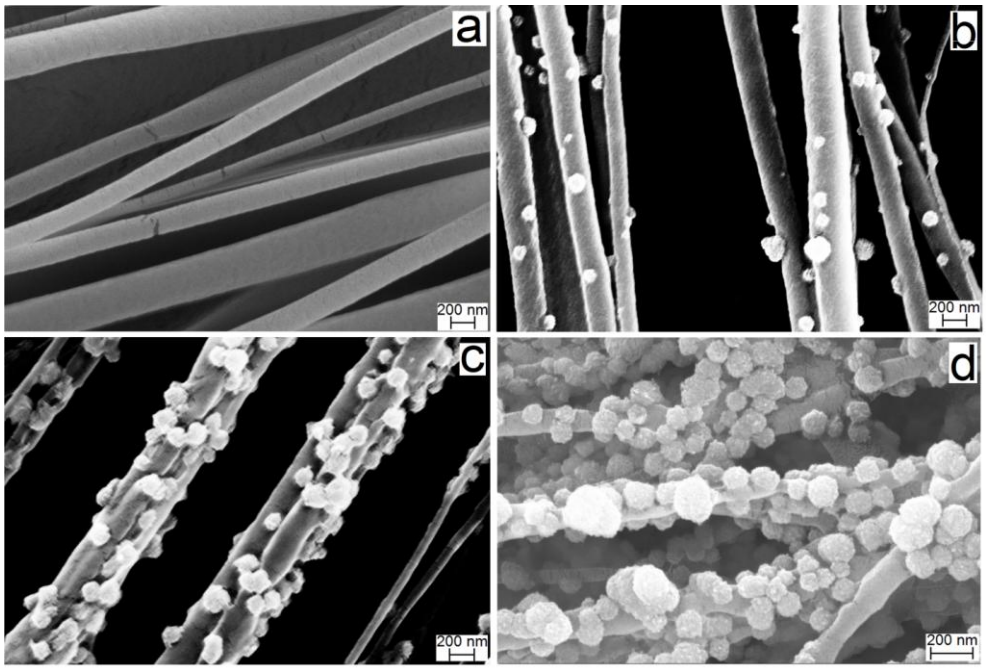

Figure 4.1 SEM images of the microsheets after incubation in m10SBF medium. Images (a) and (b) are low magnification images of PLGA and PLGA/PLA-GLU microsheets after incubation in m10SBF for 24 h, respectively. Images (b) and (c) are for PLGA/PLA-GLU microsheets after 6, and 24 h incubation in m10SBF, respectively. Image (d) is for PLGA/PLA-GLU microsheets deposited with CaP crystals in a layer-by-layer (LBL) approach. Scale bars in (a-d) represent 200 nm, respectively.

Mineralization in osteons occurs under the function of glutamic-acid rich residues of bone sialoprotein and osteonectin [181, 182]. Therefore, peptides including polyglutamic acid sequences have been widely investigated to determine the interaction with nHA crystals. For example, Itoh et al. coated HA with the synthetic peptide

(E_7PRGDT), and seeded osteoblastic cells onto the surface. They demonstrated that the amount of E_7PRGDT peptide containing polyglutamic acid sequence bound to HA was higher than passively adsorbed RGD at all coating concentrations due to high affinity of polyglutamic acid peptide to nHA crystals [183]. In addition, Sarvestani et al. treated the surface of nHA particles with glutamic acid peptide (Ac-Glu6). It was indicated that the average density of elastically active chains in the PLEOF network increased significantly when nHA in the network were treated with the osteonectin-derived Ac-Glu6 [173]. Similar to others, in our previous study, conjugation of glutamic acid template peptide on NF significantly increased the CaP nucleation (Chapter 3). Thus, in this study we used the glutamic acid conjugated NF to nucleate the CaP crystals. 50 % CaP to fiber mass ratio (GLU-NF/CaP50) was used to fabricate the osteon-mimetic microtubes. The micro-tubuler structure of the biofabricated scaffolds ideally mimics the osteons structures in cortical bone [184].

The effect of the heat treatment on GLU-NF, GLU-NF/CaP30, GLU-NF/CaP50, and LBL/CaP200 microsheets porosity and density are shown in Figure 4.2c and 4.2d, respectively. The results indicated that the porosity of the CaP nucleated microsheets after heating decreased significantly for all the test groups. In addition, the appeareant density of different CaP containing GLU-NF microsheets was increased significantly for each test group after heat treatment. The tensile modulus of the microsheets before and after heat treatment is shown in Figure 4.2e. The heat treatment significantly increased the tensile modulus of the CaP nucleated GLU-NF microsheets. For example, the tensile modulus of GLU-NF/CaP50 microsheets increased from 539±3 MPa to 770±65 MPa. It was demonstrated that there was a significant increase in tensile modulus on GLU-

NF/CaP50 microsheets after heat treatment. These results indicated that the stiffness of GLU-NF/CaP50 microsheets was increased by heat-shrinking the microsheets. Similar with our results, it has been reported that with the increasing the apatite content in nanofibrous microsheets, the tensile modulus of the microsheets increases significantly [185]. In addition, incorporation of nHA crystals in polycaprolactone fibers increases the tensile modulus of fabricated electrospun NF [149]. Overall, nAP deposited GLU-cNF have the potential to provide higher structural support to progenitor cells compared to NF with no nAP content. It has been observed that increasing mineral content on NF significantly enhanced MSCs adhesion and differentiation [186].

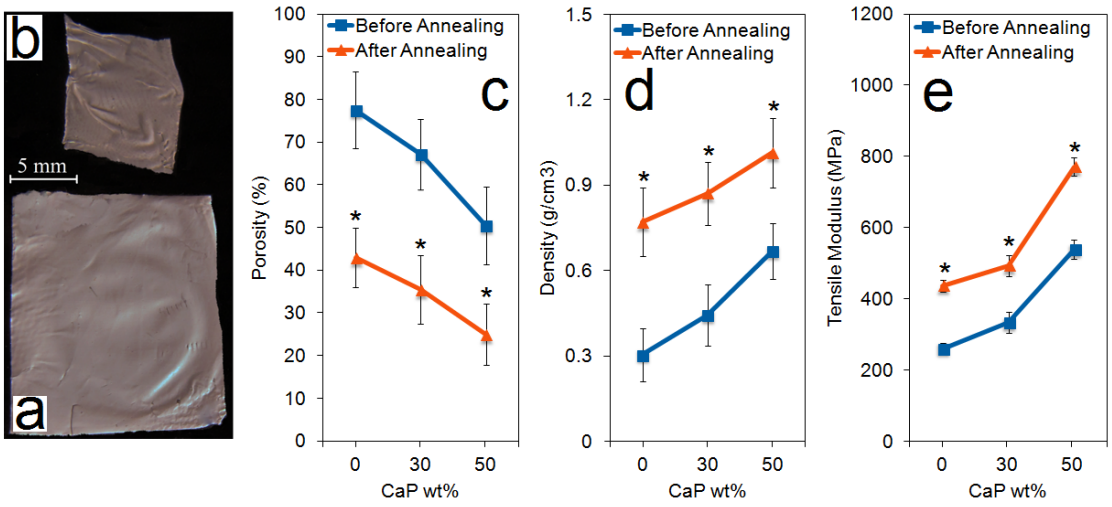

Figure 4.2 Effect of heat treatment on the aligned nanofiber microsheet shrinkage before heating (a) and after heating (b). The effect of heat shrinking on porosity(c), density(d) and tensile modulus(e). Experimental groups include GLU-NF, GLU-NF/CaP30, GLU-NF/CaP50, and GLU-NF/LBL200. One star indicates statistically significant difference (s.d.; $p<0.05$) between before annealing and after annealing for the same experimental group. Error bars correspond to means ± 1 SD for n = 3.

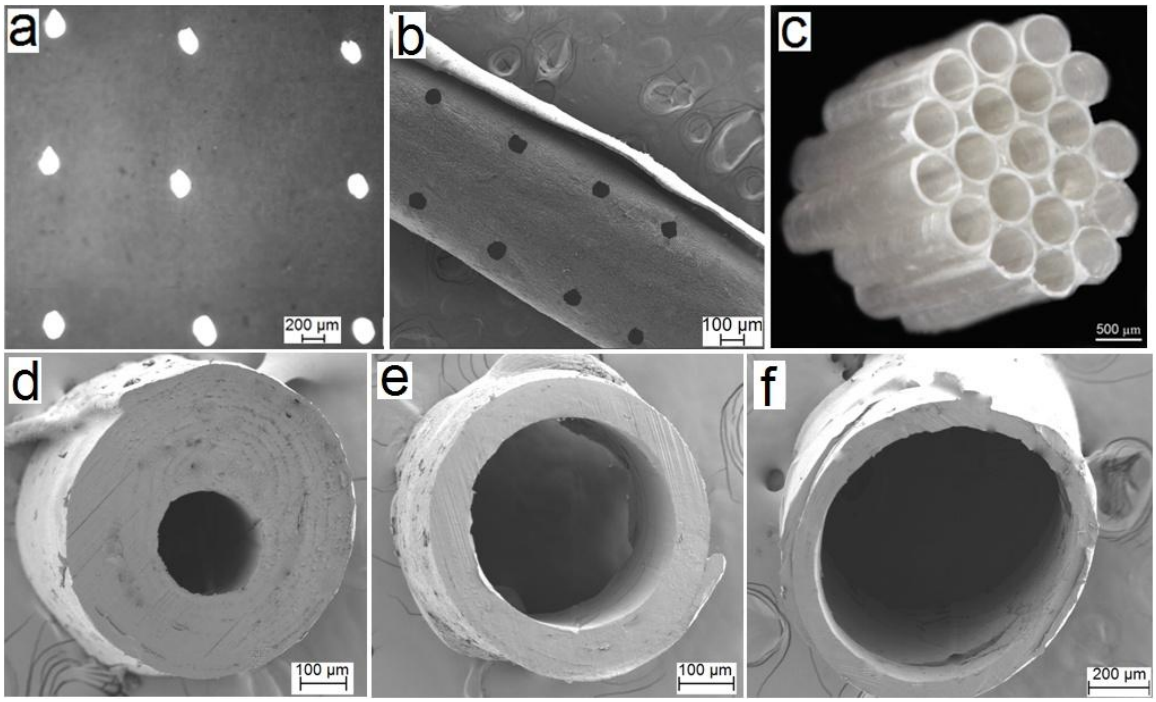

Figure 4.3 SEM image of CaP deposited nanofiber microsheet with array of circular macropores(a), SEM image of microtube fabricated by wrapping a perforated microsheet around a needle followed by heat treatment at 80 C^{o} for 10 min (b), and the image of perforated microtube bundles of twenty microtubes with the average microtube diameter of 450 µm (c), SEM images of different inner diameter microtubes 250 µm (d), 450 µm (e), and 800 µm (f).

The limitation of nanofibers fabrication with electrospinning is that it produces a relatively two dimensional fibrous scaffolds. In addition, the pore sizes are relatively smaller which does not allow cells to penetrate into the scaffold [177]. To overcome these problems, perforated nanofibrous microsheets were used to fabricate three dimensional microtubes with different diameters. This biofabrication technique could be a potential way to develop highly porous 3D nanofibrous scaffolds. The SEM images of micropores structures on the microsheets and microtubes after heat treatment are shown in Figure 4.3a and Figure 4.3b. The average size of the micropores was 180 µm. The microtubes were fabricated in different inner diameters by wrapping the perforated microsheets around different size needles. In figure 4.3, SEM images of different inner

diameter microtubes 250μm (d), 450 μm (e), and 800(f) are shown. The fabricated microtubes bundled together by annealing at 80 C^o for 10 min. Figure 4.3c shows the bundle of microtubes average individual tube size of 450 μm. This biofabrication technique of osteon-mimetic tubular scaffolds would enable to develop larger scale bone grafts with the nanofbirous structure and microscale osteon size.

4.3.2 OSTEOGENIC DIFFERENTIATION OF MSCs IN MINERALIZED MICROTUBES AND ON MICROSHEETS

The immunohistochemistry images of MSCs for Cd73, CD90, VE-cadherin, and CD-31 (PECAM-1) are shown in Figure 4.4a1-4.4a4. The results indicated that MSCs had strong CD73 and CD90 expression, whereas there was no VE-cadherin and CD-31 expression. Similar with our results, Gustafsson et al. and Valarmathi et al. demonstrated that isolated rat MSCs exhibited high expression of mesenchymal markers of CD73, and CD90 and negative expression for CD-31 and VE-cadherin[187, 188].

In order to observe the morphology of individual cells, MSCs were seeded on the microsheets at low density of 1500 cells/cm^2 and incubated in osteogenic medium. Fluorescent images (a-c) of cell nuclei (blue) and cytoskeletal actin filaments (red) in Figure 4.4b1-4.4b4 show morphology of the MSCs seeded on GLU-NF (a), GLU-NF/CaP30 (b), and GLU-NF/CaP50 (c) and LBL/CaP200 microsheets after two days of incubation. The images indicate that the seeded cells completely aligned with fiber direction irrespective with CaP nucleation. Inset images in Figure 4.4b1-4.4b4 show the SEM images of corresponding GLU-NF (a), GLU-NF/CaP30 (b), GLU-NF/CaP50 (c), and LBL/CaP200 microsheets.

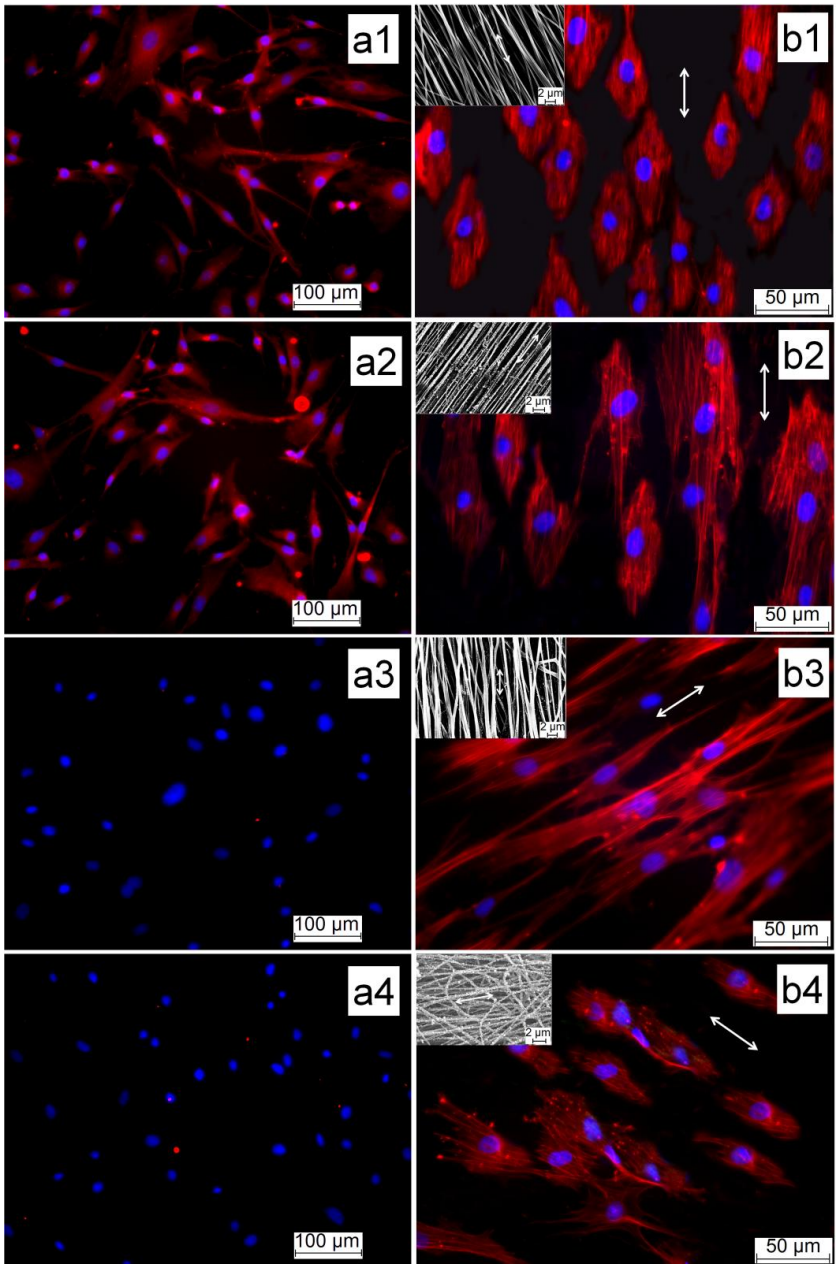

Figure 4.4 The immunohistochemistry images of MSCs stained with CD73(a1), CD90 (a2), VE-cadherin(a3) and CD-31(a4). Morphology of MSCs seeded on GLU-NF(b1), GLU-NF/CaP30(b2), GLU-NF/CaP50(b3), and GLU-NF/LBL200(b4) microsheets after seven days of incubation in osteogenic medium (scale bar is 100 µm). In the images, cell nuclei and cytoskeletal actin are stained with DAPI (blue) and phalloidin (red), respectively. The arrow in the images shows direction of the aligned nanofibers. The inset in each image shows the corresponding SEM images of the GLU conjugated nanofiber microsheets before (GLU-NF, a) and after incubation in m10SBF medium for 6h (GLU-NF/CaP30, b) and 24h (GLU-NF/CaP50, c) (scale bar is 2 µm).

MSCs differentiation into an osteogenic lineage occurs in a two-stage maturation process, where ALPase increases and peaks in the early stage of osteogenic differentiation and mineralization, and then decreases while calcium content starts to increase [151]. For both experimental groups, the DNA content after 7 days started to decrease gradually. It has been demonstrated that differentiation of MSCs osteogenic media significantly reduces the proliferation of MSCs [93, 189]. MSCs were seeded in 0.35 mm (MT, 0.35mm), and 0.8 mm (MT, 0.8 mm) diameter microtubes and cultured in osteogenic media for 28 days. DNA content, ALPase activity, calcium content, and total collagen content of the MSCs were analyzed as a function of incubation time. Figure 4.5a shows the DNA content of the MSCs 0.35 mm, and 0.8 mm diameter microtubes as a function of incubation time. The time points for osteogenic differentiation of MSCs were 7, 14, and 28 days. Since the cell seeding density kept constant for all experimental groups ($1x10^5$ cells/cm2), the DNA content in 0.35 mm microtubes was significantly lower than 0.8 mm microtubes and microsheets. In addition, it was indicated that the CaP deposited microsheets and formed microtubes did not have a toxic effect on the seeded cells.

ALPase activity of the MSCs in 0.8 mm, and 0.35 mm diameter microtubes as a function of incubation time is shown in Figure 4.5b. In the experimental groups, ALPase activity peaked after 14 days, then it started to decrease gradually for different size microtubes cultures. The results indicated that there was no significant difference between 0.8 mm and 0.35 mm microtubes on day 14. For example, the the peak value of ALPase activity of MSCs in 0.35 mm, and 0.8 mm microtubes 4370±654, and 5275±685 IU/mgDNA at day 14, respectively. ALPase activity of all other groups, incubated in

osteogenic medium, peaked after 14 days and returned to baseline level at day 28, consistent with previous reports [151]. These results indicated that the inner diameter of the microtubes did not affect on the ALPase activity of MSCs. It was demonstrated that ALPase activity of MC3T3-E1 preosteoblast cells on apatite coated poly (ε-caprolactone) (PCL) fibers was higher than uncoated PCL fibers [123]. In addition, it was reported that the presence of nHA on poly-caprolactone fibers enhanced the ALP activity of MC3T3-E1 preosteoblast cells [190]. This result is consistent with previous results that showed the calcium content of MSCs on aligned and random PLAA NF significantly increased with time [93]. High ALPase expression is a marker of maturation phase of MSCs, while high expression of OC and OP represents mineralization phase of osteogenic differentiation of MSCs [178]. In addition, it was demonstrated that ALPase expression decreases during the mineralization phase of MSCs [191].

Calcium content of the MSCs in microtubes (0.35mm and 0.8 mm) as a function of incubation time is shown in Figure 4.5c. The results indicated that there was no significant difference on the Ca content of 0.35 mm and 0.8 mm microtube groups on calcium content. For example, the calcium content in 0.35 mm microtubes were 453±59, and 0.8 mm microtubes were 635±41 mg Ca/mg DNA, respectively. All calcium measurements were subtracted from the amount at day 0 to remove the calcium due to CaP deposition prior to cell seeding. For all groups, extent of mineralization of the MSCs increased gradually from day 7 to 28 in osteogenic medium. This result is consistent with previous results that showed the calcium content of MSCs on aligned and random PLAA NF significantly increased with time [93].

The total collagen production in microtubes (0.35 and 0.8 mm) is showed in

Figure 4.5d. The secretion of newly formed collagen is important to enhance the stability of the mineralized microtubes and microsheets during the culture. For example, the total collagen production of MSCs in microtubes (0.35 and 0.8 mm) was 472±75, 821±95, and 983±127 μg Collagen/μg DNA after 28 days, respectively. There was no significant difference on collagen secretion between 0.35 mm and 0.8 mm microtubes. Moreover, the total collagen content gradually increased in both microtubes and microsheets culture with the increase of incubation time.

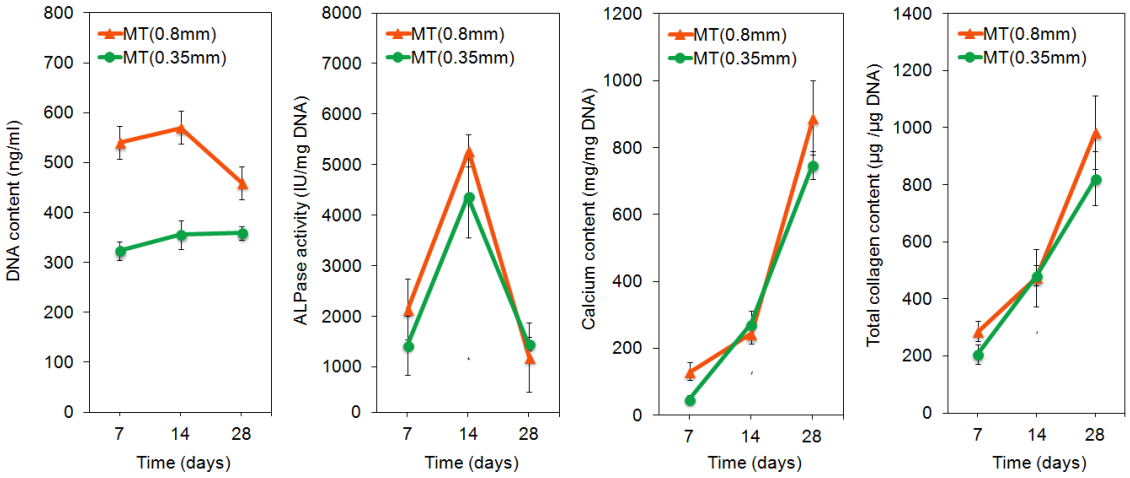

Figure 4.5 DNA content (a), alkaline phosphatase activity (b), calcium content (c), and total collagen amount (d) of MSCs seeded inside GLU-NF/CaP50 microtubes cultured in osteogenic media. Experimental groups include GLU-NF/CaP50 0.35 mm microtubes (green), and 0.8 mm diameter microtubes (red). Time points include 7, 14, 28 days. Error bars correspond to means ± 1 SD for n = 3.

The heat treatment of the microsheets improved the mechanical properties of the CaP nucleated GLU-NF microsheets. Our results indicate that the tensile modulus of GLU-NF increases by increasing the CaP content and heat treatment of the microsheets. This was consistent with the previously reported results showing that increasing the apatite amount on NF significantly increases the tensile modulus [185]. Moreover, it was

reported that incorporation of nHA crystals in polycaprolactone fibers increased the tensile modulus of fabricated electrospun NF [149]. Overall, the engineered microtubes from CaP nucleated GLU-NF have the potential to provide structural support to progenitor cells in bone tissue regeneration.

4.4 CONCLUSION

In this study, our objective was to investigate the effect of inner diameter of microtubes on osteogenic differentiation of rat MSCs. Extensive in vitro characterization indicated that the microtubular scaffolds are not only able to support cell attachment and proliferation, but also to provide an environment which improves the osteogenic differentiation of MSCs. This was confirmed by the increasing alkaline phosphatase activity, calcium phosphate deposition, and collagen content. In addition, the fabricated microtubes could be fused and larger scale tubular scaffolds for bone grafts application could be fabricated. It was also demonstrated that changing the inner diameter of the microtubes from 0.8 to 0.35 mm did not change the cytochemical results significantly. Present findings demonstrate that the 3D structure of microrubular scaffolds provide a promising microenvironment that enhances osteogenesis.

CHAPTER 5

VASCULOGENIC DIFFERENTIATION OF MARROW STROMAL CELLS (MSCs) and ENDOTHELIAL PROGENITOR CELLS (EPCs) IN OSTEON-MIMETIC MINERALIZED NANOFIBROUS MICROTUBES

5.1 INTRODUCTION

The cortical bone composed of osteons that have microtube like structures with a central vascular channel inside for ensuring suitable nutrient/waste transport to the bone tissue [11]. Laminated multilayers of CaP deposited collagen fibers forms the osteon microtubes. The development of three-dimensional (3-D) bone tissue in-vitro has been limited by the need to create a vascular network within the tissue to supply required oxygen and nutrients to maintain tissue viability and function [192]. Vascularization inside the scaffold enhances diffusion and provides optimal nutrient/waste transport for engineered scaffolds [193]. The combination of endothelial progenirator cells (EPCs) with marrow stromal cells and seeded into engineered bone grafts has been offered as a promising and efficient approach to enhance vascularization and promote successful bone formation at the graft site [194-196]. For instance, cocultures of EPCs with MSCs in poly(lactic-co-glycolic acid) [PLGA] have shown enhanced microvascular network formation [197]. Therefore, engineered bone grafts that can mimic the microstructure of bone and have pre-vascularized structures that induce nutrients transport would be a strong candidate for bone tissue engineering applications.

The physical configuration of the scaffolds, which mediate the cell-cell and cell-scaffold interactions, exert strong influence on the success of osteogenic and vasculogenic processes in vitro [174, 175]. The success of engineered scaffold mostly depends on how closely the cell-scaffold relationship mimics that natural tissue in vivo. The effect of the size of fabricated microtubes on EPCs/MSCs vasculogenic differentiation has not been studied yet. To this end, we hypothesized that 3D structure of microtubes with well-defined pores could potentially mimic the microstructure of osteons in cortical bone and induce vasculogenesis of MSCs and EPCs. In order to test this hypothesis, we investigated the vasculogenic differentiation potential of MSCs/EPCs when co-cultured and seeded into microtubes engineered from CaP deposited aligned nanofiber microsheets that have an array of macropores to enhance diffusion of nutrients. The microtube structure fabricated by wrapping CaP deposited nanofiber layers around the stainless steel needles upon application of heat energy to fuse by raising the temperature above PLGA glass transation temperature. Our results indicate that the 3-D microtubes provide a promising microenvironment that enhances vascularization of MSCs-EPCs co-culture.

5.2 MATERIALS AND METHODS

5.2.1 MATERIALS

N,*N*-Dimethylformamide (DMF), methylene chloride (DCM), *N*,*N* diisopropylethylamine (DIEA), *N*,*N*′-di- isopropylcarbodiimide , triisopropylsilane (TIPS), *N*,*N*-dimethylaminopyridine (DMAP), hydroxybenzotriazole (HOBt) and trifluoroacetic acid (TFA) were received from Acros Organics (Pittsburgh, PA). Diethyl ether and hexane were obtained from VWR (Bristol, CT). Piperidine, and triethylamine

(TEA) were purchased from Aldrich (Milwaukee, WI).The protected amino acids and Rink Amide NovaGel resin were purchased from EMD Biosciences (San Diego, CA). Dulbecco's phosphate-buffered saline (PBS) and Dulbecco's Modified Eagle's Medium (DMEM; 4.5 g/L glucose with L-glutamine and without sodium pyruvate) were obtained from Cellgro (Herndon, VA). Ethylenediamine- tetraacetic acid disodium salt (EDTA), penicillin, and paraformaldehyde were purchased from Sigma (St. Louis, MO). All other solvents and chemicals were used as received. QuantiChrom Calcium Assay Kit, and QuantiChrom ALPase assay kits were purchased from Bioassay Systems (Hayward, CA). Sircol Collagen Assay kit was purchased from Biocolor Life Science assays (Antrim, United Kingdom). Alexa Fluor® 594 phalloidin, Trypsin, and 4',6-diamidino-2-phenylindole (DAPI) were purchased from Invitrogen (Carlsbad, CA). All the antibodies for immunostaining were purchased from Santa Cruz Biotechnology (Santa Cruz, CA). The PLGA (*Durect Corporation, Pelham, AL*) sample was a 50/50 copolymer of D, L-lactide and glycolide monomers with intrinsic viscosity of 1.1 dL/g and weight average molecular weight of 105 kDa. 1, 1, 1, 3, 3, 3-hexafluoro-2-propanol (HFIP), was purchased from VWR (West Chester, PA). Reagent grade chemicals (Fisher Scientific) were used in the preparation of m10SBF solution: NaCl, KCl, $CaCl_2 \cdot H_2O$, $MgCl_2 \cdot 6H_2O$, NaH_2PO_4, $NaHCO_3$. Matrigel was purchased from BD Biosciences (San Jose, California). CellTracker™ (Red) and Calcein-AM (Green) were obtained from Invitrogen (Carlsbad, CA). EBM-2 medium and following growth factors and supplements of the media such as vascular endothelial growth factor (VEGF), human fibroblast growth factor-B (hFGF-B) R^3-insulin like growth factor (R^3-IGF-1), human epidermal growth

factor (hEGF), ascorbic acid hydrocortisone, gentamycin, and amphotericin B were purchased from Lonza (Hopkinton, MA).

5.2.2 FABRICATION OF MINERALIZED GLUTAMIC ACID TEMPLATED PEPTIDE CONJUGATED NANOFIBROUS MICROTUBES

The EEGGC peptide was synthesized manually on Rink Amide NovaGel^{TM} resins as described [100, 125, 126]. Briefly, rink amide NovaGel^{TM} resin (100g) was incubated in DMF (3 ml) for 30 min to swell completely. Then, the resin was washed with DMF (2×3 ml). Fmoc-protected amino acid derivative (6 eq.) and HOBt (12 eq.) were dissolved in dry DMF (3 ml). Next, DIC (6.6 eq.) as an accelerator was added to the mixture. Then, the resulting mixture was shaken 5-10 min and added to the resins. Then, 0.2 ml DMAP (0.05 M) was added to the mixture. The mixture was placed in an orbit shaker for 4-6 hr at 30°C. The reaction was tested using Kaiser reagents. If the test result was positive, the above coupling reaction would be repeated until a negative result was reached. After the reaction, the resins were washed with DMF (5×3 ml) and treated with 20% piperidine in DMF for 2 × 15 min in order to deprotect the F-moc groups of the amino acids. The subsequent amino acids were coupled using the same method. After peptide chain elongation, the resins were washed with 5 × DMF and 5 × DCM. The EEGGC peptide was cleaved from the resin by treating with 95% TFA/2.5% TIPS/2.5% water and precipitated in cold ether. After drying, the EEGGC peptide was conjugated to poly (lactide) acrylate (PLAA, MW=4000 Da) macromer by Michael's addition reaction between the acrylate group on the macromer and the cysteine's sulfhydryl group on the peptide to produce a PLAA-EEGGC conjugate. A mixture of the peptide and PLAA macromer (2:1 molar ratio) was dissolved in a 1:1 mixture of DMF:water, and allowed to

react at 30°C overnight in an orbital shaker. The mixture was dialyzed against DI water and lyophilized to obtain the dry product.

Electrospinning solutions of high molecular weight PLGA (10w%) and mixtures of PLAA conjugated EEGGC peptide (1.5% of PLGA amount) were prepared in HFIP. A programmable KDS100 syringe pump (KD Scientific, Holliston, MA) was used to pump the polymer solution, which was inside a 1 ml syringe (Norm-Ject, Henke Sass Wolf GmbH, Tuttingen, Germany) to the end of a 21 GTW needle (PrecisionGlide, 0.81 mm O.D., Becton-Dickinson, Franklin, NJ) at a specified flow rate of 1.0 ml/h. The 20 kV positively charged Pt electrode of a high voltage supply (ES40P-5W/DAM, Gamma High Voltage Research) was connected to the needle. A high-speed rotational wheel collector (custom built in the Machine Shop at University of South Carolina) was used to prepare glutamic acid template aligned nanofiber microsheets (GLU-NF). A grounded aluminum wheel (20 cm diameter and 5 mm thickness) powered by a high speed DC motor (2M0578, up to 5000 rpm, Dayton Electric, Niles, IL) was used to collect nanofibers and placed at 7.5 cm underneath the needle. The force generated by the high electric field between the needle and the rotating wheel overcame the surface tension of the polymer solution and stretched the accelerating jet as fibers toward the collector while the solvent evaporated during the process. The polymer jet, after deposition on the collector, was further stretched by the tangential force produced by the rotation of the wheel and formed aligned fibers on the edge of the wheel.

Mineralization of nanofiber microsheets was occurred by depositing the apatite crystals on nanofiber microsheets via using Lie et al.'s modified 10-fold-concentrated simulated body fluid (m10SBF(1). Briefly, the stock solution of 10SBF was prepared by

dissolving NaCl, KCl, $CaCl_2$• H_2O, $MgCl_2$• $6H_2O$ and NaH_2PO_4 in distilled deionized (DDI) water (10SBF stock solution pH=4.2). Next, in order to reach physiological pH of 7.4, 60 mM of $NaHCO_3$ was dissolved in the 10SBF stock solution prior to mineralization process. The impurities and formed large CaP crystals in the pH range of 5.9 to 7.4 were removed by filtering the solution through a 0.22 μm pore size filter system. Nanofiber microsheets were then immersed in m10SBF filled plastic beaker and kept at room temperature for 6h and 24h. The m10SBF was replaced with fresh m10SBF every 6 h over apatite growth cycle. After removal from m10SBF, the nanofiber microsheets were washed with DDI water three times and then dried at room temperature.

CaP nucleated elctrospun microsheets (5 cm length*1 cm witdh) wrapped around the 21 GTW needle (PrecisionGlide, 0.81 mm O.D., Becton-Dickinson, Franklin, NJ) and placed in pre-heated 80 C^o oven for 10 min in order to let the microsheets shrink and keep it's microtubalar structure by shape memory effect. Prior to wrapping the microsheets around the needle, uniform micropores were created by 29 GTV needle (PrecisionGlide, 0.34 mm O.D., Becton-Dickinson, Franklin, NJ) on the microsheets to induce diffusion of nutrients and oxygen during the cell culture period.

5.2.3 MSCs and EPCs ISOLATION, CHARACTERIZATION AND SEEDING

MSCs were isolated from the bone marrow of young adult male Wistar rats (6-8 weeks) [93, 100, 125, 176]. Cell isolations were performed under a protocol approved by the Institutional Animal Care and Use Committee of the University of South Carolina. Wistar rats were sacrificed, and femurs and tibias were aseptically removed. The marrow was flushed out with 20 ml of cell isolation medium which consisted of DMEM supplemented with 10% FBS, 100 μg/μL streptomycin, 100 units/mL penicillin, 20

µg/mL fungizone, and 50 µg/mL GS. The cell suspension was centrifuged at 200g for 5 min and the cell pellets were re-suspended in 12 ml of primary medium (DMEM supplemented with 10% FBS, 100 units/mL penicillin, 100 µg/mL streptomycin, 50 µg/mL GS, and 250 ng/mL fungizone), aliquoted into T-75 flasks and maintained in a humidified 5% CO2 incubator at 37 °C. Cultures were washed with PBS and replaced with fresh media at 3 and 7 days to remove unattached cells. Cells were rinsed with PBS, enzymatically lifted with 25 µL/cm^2 0.05% trypsin/ 0.53 mM EDTA and centrifuged at 200g for 5 min. The third passage cells were used for cell culture experiments. Cell attachment to the nanofiber mesh was done with undifferentiated MSCs cultured in the primary medium.

EPCs were isolated from the bone marrow of young male Wistar rats (6-8 weeks). After euthanasia, the femurs and tibias were aseptically excised from the hind limbs and washed in DMEM medium. To expose the marrow cavity, the distal end of tibia and proximal end of femur were cut off. Small holes were bored in the other end of bone with 18 gauge needle. Next, the bone marrow was flushed out by gently flushing the inside of the bones with Medium199 supplemented with 20% FBS, 1% Pen/Strep, 1% L-Glu, 1% sodium pyruvate and 22.5 µg/ml heparin. Cell clumps were broken up by repeatedly pipetting. The cell suspension was centrifuged at 200g for 5 min. Next, the cell pellet was re-suspended in the medium199 and plated on rat-derived fibronectin-coated 6-well plate (1µg/ml). After 24h, the non-adherent cell population supernatant was recovered and transferred to a new fibronectin-coated plate. After another 24h, this procedure was repeated to remove rapidly adherent hematopoietic cells or mature EC being possibly present in the aspirate. Only the non-adherent cell population harvested after 48 h was

evaluated further in all experiments.

MSCs and EPCs were characterized by immunostaining of specific surface markers. Isolated MSCs and EPCs were fixed with 4% paraformdehyde for 30 min, permeabilized with 0.1% Triton X-100 and 100 mM glycine in PBS (pH 7.4) for 1 h and blocked with blocking solution including 1.5% BSA and 0.5 mM glycine in PBS for 2 h. The primary antibodies used for MSCs characterization are CD73, CD90, VE-cadherin, and vWF. The primary antibodies used for EPCs characterization are VE-cadherin, vWF, PECAM-1, Flk-1, CD73, and CD90. The primary antibodies diluted in blocking solution for 1:100 and incubated with cells for 12–16 h at 4 °C. Secondary antibodies (Alexa fluor® 488, 593 obtained from Molecular Probes, Invitrogen) were used at 1:100 dilutions in blocking buffer for 2 h at room temperature in the dark. Nuclei were stained with DAPI (4, 6-diamidino-2-phenylindole, 100 ng/ml). Images of the cells were visualized by using a fluorescence microscope (Zeiss LSM 510 Meta CSLM). MSCs characterization results were presented in Figure 4.4.

The microtubes were sterilized by ultraviolet radiation for 12 h with a mercury UV lamp (Black-Ray, 365 nm, 100 W; UVP, Upland, CA), followed by immersing in 70% ethanol for 30 min and washing three times with sterile PBS. The microtubes were conditioned by immersion in primary culture media for 1 h prior to cell seeding. In order to form vasculogenesis, EPCs/MSCs were mixed (1:1) in Matigel (derived from a mouse sarcoma line)- PBS (1:1 mixture) and 5 µl of cell-matrigel suspension were injected inside the microtubes and cultured in EBM-2 medium containing vascular endothelial growth factor (VEGF), human fibroblast growth factor-B (hFGF-B), insulin like growth factor-1 (IGF-1), human epidermal growth factor (hEGF), ascorbic acid hydrocortisone,

gentamycin, amphotericin B and cultured in a humidified 5% CO_2 incubator for up to 12 days. Prior to experiment, EPCs were stained with cell tracer and MSCs were stained with Calcein-AM. After 12 days of culturing, construct images of the cells were visualized using a confocal microscope (Zeiss LSM 510 Meta CSLM).

5.2.4 VASCULOGENIC DIFFERENTIATION OF MSCs/EPCs IN MICROTUBES

The DNA and total collagen content in EPC/MSC seeded microtubes were measured after 3, 6, and 12 days of culture. At each time point, cell-seeded microtubes were washed with serum-free DMEM for 8 h to remove serum components, then washed with PBS, lysed with 10 mM Tris supplemented with 0.2% triton in PBS and used for the measurement of DNA content and total collagen content. The double-stranded DNA content of the samples was determined by using a Quant-it PicoGreen assay (Invitrogen, Carlsbad, CA) according to the manufacturer's instruction. An aliquot (100 µl) of the working solution was added to 100 µl of the cell lysate and incubated for 4 min at ambient conditions. The fluorescence was measured with a Synergy HT plate reader (Bio-Tek; Winooski, VT) at emission and excitation wavelengths of 485 and 528 nm, respectively. Collagen production was analyzed by SIRCOL collagen assay kit protocol (Biocolor, Newtownabbey, UK) in the supernatants after 7, 14 and 28 days of cell culture in microtubes. The collagen containing supernatant from the culture was mixed with 1 mL of Sircol dye for 30 min and centrifuged at 10,000 rpm for 5 min to precipitate the collagen–dye complex. After decanting the suspension, pellets were dissolved in 1 mL Sircol alkali reagent and vortexed. Subsequently, 100 µl of the acquired solution was read at 555 nm. The amount of collagen was calculated based on a standard curve of

Sircol Rat Collagen Reference Standard (Biocolor). Cell lysate solution was used as a negative control.

5.2.5 mRNA ANALYSIS OF MSCs/EPCs IN MICROTUBES

At each time point for vasculogenic differentiation samples, total cellular RNA was isolated using TRIzol (Invitrogen, Carlsbad, CA) plus RNeasy Mini-Kit (Qiagen, Valencia, CA) according to the manufacturer's instructions. The qualitative and quantitative analysis of the RNA samples was performed with NanoDrop 2000 (Thermo Scientific, Waltham, MA). A 1 μg quantity of the extracted total RNA was subjected to cDNA conversion using the Reverse Transcription System (Promega, Madison, WI). Primers for real-time PCR (RT-qPCR) analysis were designed and selected using the Primer3 web-based software as described elsewhere [125]. RT-qPCR was performed to analyze the differential expression of platelet/ endothelial cell adhesion molecule 1 (PECAM-1), von Willebrand homology (vWF), vascular endothelial-cadherin (VE-cadherin), and endothelial-specific receptor tyrosine kinase (Tie-2) genes with SYBR green RealMasterMix (Eppendorf, Hamburg, Germany) using a Bio-Rad iCycler machine (Bio-Rad, Hercules, CA) and iCycler optical interface version 2.3 software. The forward and reverse primers were synthesized by Integrated DNA technologies (Coralville, IA) and shown in Table 1. Quantification of gene expression was based on the crossing-point threshold value (CT; number of cycles required for the RT-qPCR fluorescent signal to cross the threshold) for each sample. This was evaluated by the Relative Expression Software Tool [198] as the average of three replicate measurements. The expression of glyceraldehyde-3- phosphate dehydrogenase (Gapdh) house-keeping gene was used as the reference. The relative gene expression level was compared to that at time zero using

2^-ddCT method [199].

Table 2 Forward and reverse sequences of the PCR primers.

Genes	Forward Primer	Reverse Primer
PECAM-1	5`-CGAAATCTAGGCCTCAGCAC-3`	5`-CTTTTTGTCCACGGTCACCT-3`
VE-cadherin	5`-GCACCAGTTTGGCCAATATA-3`	5`-GGGTTTTTGCATAATAAGCAGG-3`
vWF	5`-GCTCCAGCAAGTTGAAGACC-3`	5` -GCAAGTCACTGTGTGGCACT–3`
Tie-2	5`-CCGTGCTGCTGAACAACTTA-3`	5`-AATAGCCGTCCACGATTGTC-3`
GAPDH	5`-CGA CCT GGA AGT CCA ACT AC-3`	5`-ATC TGC TGC ATC TGC TTG-3`

5.2.6 STATISTICAL ANALYSIS

The results are presented as averages and standard errors. Significant differences between two groups were evaluated using a two-tailed Student's t-test. A value of $p < 0.05$ was considered statistically significant.

5.3 RESULTS AND DISCUSSION

The interconnected network of the cortical bone is composed of a set of microtubular osteons. In this study, the osteon structure was mimicked by fabricating the CaP nucleated NF based microtubes. The fabricated microtubes were evaluated with respect to the effect of scaffold morphology on vasculogenesis of MSCs/EPCs. The osteogenic and vasculogenic differentiation of MSCs and EPCs/MSCs on nanofibers were previously shown [93, 200]. However the effect of the morphology of the scaffold on vasculogenic differentiation has not yet been studied. Consequently, the objective of this study was to determine the in vitro vasculogenic potential of EPCs/MSCs in different diameter microtubes. The microtubuler structure of the biofabricated scaffolds ideally mimics the osteons structures of bone tissue [184].

The immunohistochemistry images of EPCs for specific positive and negative markers are shown in Figure 5.2. The results indicated that EPCs showed positive

expression of VE-cadherin, vWF, PECAM-1, and Flk-1. However, there was no expression of CD73 and CD90. These results are consistent with the previously reported results.

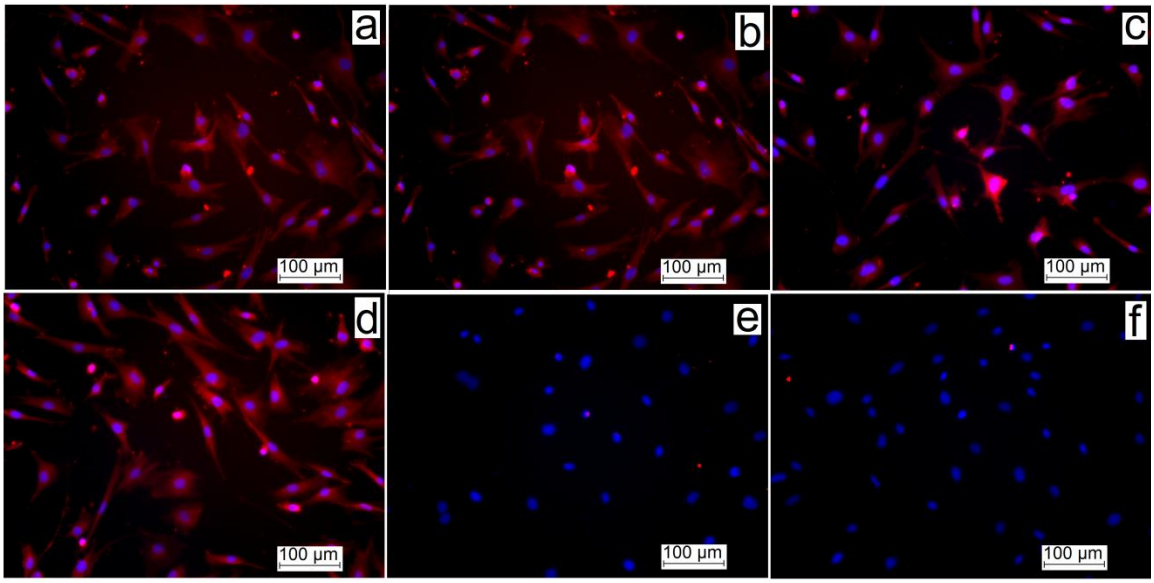

Figure 5.1 The immunohistochemistry images of EPCs stained with CD31 (a), VE-cadherin (b), Flk-1 (c), vWF (d), CD73 (e) and CD90 (f). Scale bar is 100 µm.

The effect of MSCs and EPCs co-culture on vascular structure formation was investigated. EPCs, MSCs, and EPCs/MSCs one to one ratio co-culture were encapsulated in Matrigel and cultured in vasculogenic media for 7 days. Figure 5.3a, 5.3b, and 5.3c shows the MSCs, EPCs, and MSCs/EPCs (1:1 co-culture), respectively. The results demonstrated that only MSCs/EPCs co-cultered formed vascular like structures when cultured in vasculogenic media for 7 days. These results are consistent with the previously reported results [194-196].

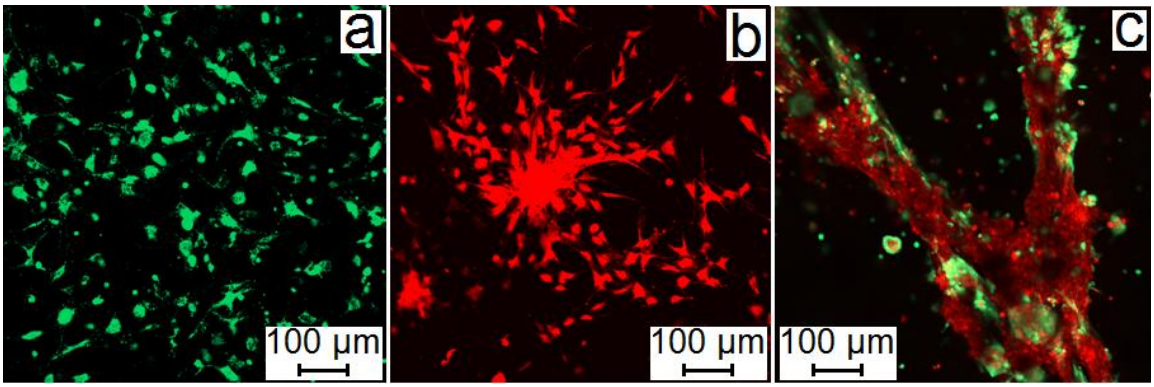

Figure 5.2 Confocal microscopic imagesof MSCs (a, green), EPCs (b, red), MSCs/EPCs cocultured in 1:1 ratio (c) encapsulated in Matrigel and cultured for 7 days in vasculogenic media. EPCs and MSCs initially stained with cell tracer and calcein AM. Blue, green and red represents cell nuclei, MSCs and EPCs, respectively.

EPCs/MSCs (1:1) were seeded in GLU-NF/CaP50 0.35 mm, and 0.8 mm microtubes by mixing (1:1) Matrigel/PBS and cultured in vasculogenic media for 12 days. DNA content and total collagen content of the EPCs/MSCs as a function of incubation time are shown in Figure 9a, and b. The time points for vasculogenic differentiation of EPCs/MSCs were 3, 6, and 12 days. The results indicated due to the lower surface area of the 0.35 mm microtubes, the DNA content was significantly lower than 0.8 mm microtubes. The total collagen production in 0.35 and 0.8 mm microtubes are shown in Figure 9b. The results indicated that the inner diameter of the microtubes did not affect the collagen secretion of MSCs/EPCs when seeded inside the microtubes significantly. Therefore, the expression levels of vasculogenic markers were only measured in 0.8 mm microtubes. For example, the collagen production of EPCs/MSCs in 0.35mm and 0.8 mm microtubeswas 132.1±7 and 130.1±9.7 µg Collagen/µg DNA after 12 days, respectively. In addition, the total collagen content was increased in different diameter microtubes with the increase of incubation time.

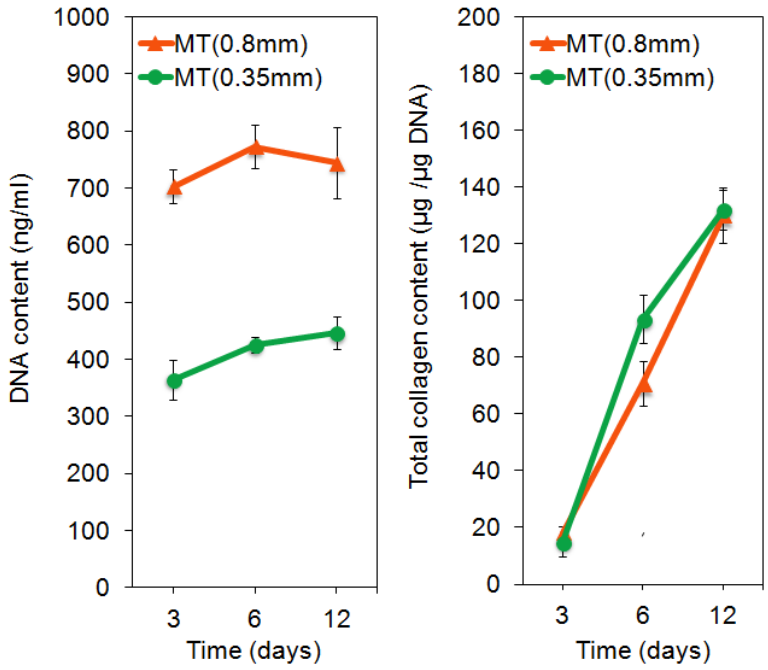

Figure 5.3 DNA content (a) and total collagen amount (b) of differentiating BMS+EPC cells seeded inside GLU-NF/CaP50 0.35 and 0.8 mm microtubes by mixing matrigel and cultured in vasculogenic media. Time points include 3, 6, and 12 days. Error bars correspond to means ±1 SD for n = 3.

A number of early and late stage markers associated with vasculogenic differentiation in vivo were used in this study to characterize the rat EPCs/MSCs at mRNA levels, which included CD31/Pecam1, VE-cadherin (CD144), Tie2, and von Willibrand factor (vWF). Platelet/endothelial cell adhesion molecule is a transmembrane protein expressed abundantly early in vascular development may mediate leukocyte adhesion and migration, angiogenesis, and thrombosis [201]. The other early-stage differentiation marker VE-cadherin, a member of the cadherin family of adhesion receptors, is a specific and constitutive marker of endothelial cell that plays an important role in early vascular assembly. Vascular markers that are expressed at a later stage include vWF and Tie2 [188, 202]. Tie2 is a receptor kinases that is vital for vascular

development and remodeling in the embryo and functions on maintenance and repair of vascular system [202]. In late phases of vasculogenesis, the mature endothelial cells will synthesize and secrete vWF homolog, a plasma protein that mediates platelet adhesion to damaged blood vessels and stabilizes blood coagulation factor VIII [203]. In order to investigate the expression pattern of key vasculogenic gene markers of EPCs/MSCs in microtubes, the expressions of Pecam1, Ve-cadherin, Tie-2 and vWF were analysed at mRNA level by real-time PCR. RT-qPCR results showed that vasculogenic differentiation of EPCs/MSCs in vasculogenic culture conditions for 12 days resulted in an increased expression of vasculogenic gene markers. The peak expression of vWF, Ve-cadherin and Tie-2 occurred around 12 days (over 350, 90 and 110 fold), indicating that the differentiating EPCs/MSCs gained the biosynthetic activity of differentiated and matured endothelial cells. The upregulation of Tie-2 after 3 days might indicate the development of the vasculogenic structure. Similar to our results, Valarmathi *et. al.* demonstrated that vasculogenic differentiation of MSCs in vasculogenic culture conditions when seeded and cultured in collagen microtubes for 28 days resulted in increased expression of Pecam1, Kdr, Tie-2 and vWF. They indicated that the peak expression of vWF around day 21 (over 400 fold) showing that the differentiating cells became matured endothelial cells and the upregulation of Tie-2 related to development of the microvessels [188]. Enhanced Pecam-1, VE-cadherin and Tie-2 expression levels in microtubes culture indicates that tubular formation of the scaffold supported vasculogenic formation of EPCs/MSCs in matrigel. These results were consistent with the collagen content results, where EPCs/MSCs in microtubes had increased amount of collagen content as a function of incubation time.

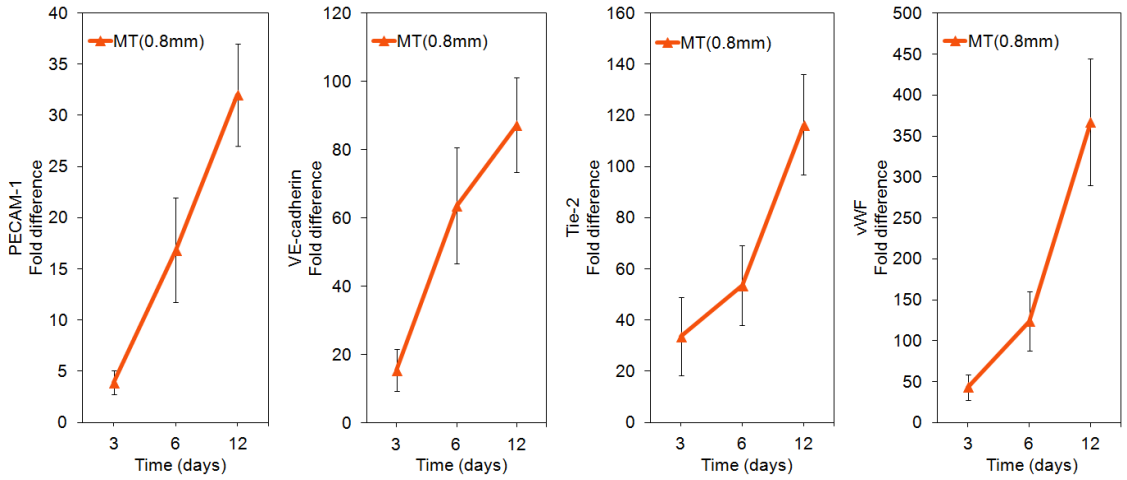

Figure 5.4 mRNA expression levels (as fold difference) of platelet endothelial cell adhesion molecule (a, pecam-1) (a), VE-cadherin (b), Tie-2 (c), and Von Willibrand factor (d, Vwf) of the MSCs/EPCs (1:1), cells seeded inside 0.8 mm microtubes by mixing matrigel and cultured in vasculogenic media.. Time points include 3, 6, and 12 days. Error bars correspond to means ±1 SD for n = 3.

5.4 CONCLUSION

In this study, our objective was to investigate the vasculagenic differentiation potential of MSCs/EPCs co-culture in different diameter microtubes fabricated via a novel biofabrication technique. Extensive in vitro characterization indicated that the microtubular scaffolds are not only able to support cell attachment and proliferation, but also to provide an environment which enables vasculogenic differentiation of MSCs/EPCs. This was confirmed by the enhanced collagen content and expression of principal vasculogenic genes. Present findings demonstrate that the 3D structure of microrubular scaffolds provide a promising microenvironment that enables vascularization. Overall, the comp;ete results in Chapter 4 and Chapter 5 demonstrates that the microtubular scaffolds can support osteogenesis and vasculogenesis of MSCs and

MSCs/EPCs co-culture. Therefore, these scaffolds can be a good candidate for bone tissue engineering applications.

CHAPTER 6

CONCLUDING REMARKS

The aim of this work is to fabricate osteon-mimetic nanocomposite scaffolds to be used as a suitable synthetic matrix in bone tissue engineering applications. The main goal of bone tissue engineering is to develop bone mimetic scaffolds seeded with mesenchymal stem cells to regenerate bone defects. Bone tissue engineering scaffolds required to have specific features such as easy to implant, appropriate physical and mechanical properties, biodegradable, osteoconductive, biocompatible and cost effective. Due to the reason that tissue engineered scaffolds will be used to treat the complex bone defects, these scaffolds should possess similar structural and functional properties of bone tissue. The cortical bone tissue composed of osteons that have microtube like structures with a central vascular channel inside for ensuring suitable nutrient/waste transport to the bone tissue. Laminated multilayers of apatite deposited collagen fibers forms the osteon microtubes. The apatite nanocrystals provide osteoconductivity and stiffness while the collagen fibers provide elasticity and a template for mineralization and maturation of osteoprogenitor cells. Unique factors that contribute to bone toughness are the aligned network of collagen fibers, apatite nanocrystals, and proteins in the bone extracellular matrix (ECM) that link the apatite crystals to the collagen fibers. In this work, calcium-phosphate nucleated polymeric nanofibers were used to mimic the morphology of the bone tissue and the effect of calcium phosphate (CaP) deposition on aligned nanofibers surface-modified with EEGGC glutamic acid peptide on osteogenic differentiation of rat

marrow stromal cells was investigated. In order to increase CaP to fiber ratio, a layer-by-layer approach was used to improve the diffusion of calcium and phosphate ions inside the microsheets. CaP to fiber ratio of the microsheets increased from 50% for a single fiber layer to 200% for the LBL microsheet with the same overall thickness when incubated in a modified SBF medium. Results demonstrate that surface modification of nanofibers with GLU peptide dramatically increased nucleation and growth of CaP nanocrystals on the fiber surface, leading to significantly higher differentiation of MSCs and mineralized matrix formation. Developed calcium-phosphate nucleated nanofiber microsheets with an array of macropores to enhance diffusion of nutrients were used to fabricate osteon-mimetic microtubular scaffolds. The microtubes fabricated by wrapping CaP deposited nanofiber layers around the stainless steel needles upon annealing above glass transation temperature (T_g). The osteogenic and vasculogenic differentiation potential of MSCs and MSCs/EPCs when seeded into microtubes were invetigated. Our results indicate that the 3-D microtubes provide a promising microenvironment that enhances osteogenesis and vascularization. Overall, apatite nucleated electrospun nanofibers and the microtubes fabricated out of these nanofiber microsheets shows promising results for clinical usage of these materials as an engineered scaffold. To continue this work, it is necessary to characterize the compressive mechanical properties of the fabricated microtubular bundles in order to determine the effective implantation sites. Furthermore, bone regeneration by using microubular scaffolds should be evaluated in vivo by animal model including femoral defect, cranial defect or subcutaneous implantation. To do that, the microtubular scaffolds should be cultured in a perfusion bioreactor after seeding with MSCs and implanted in a critical size bone defect. X-rays

and histomorphometric analysis can be used to further characterization of the forming bone tissue and quantitatively determine the osteoconductivity of the scaffolds. The potential of osteon-mimetic scaffolds for bone regeneration showed in this work will be beneficial for clinical development.

REFERENCES

1. Scheller EL, Krebsbach PH, Kohn DH. Tissue engineering: state of the art in oral rehabilitation. Journal of Oral Rehabilitation 2009 May;36(5):368-389.

2. Damien CJ, Parsons JR. Bone-Graft and Bone-Graft Substitutes - a Review of Current Technology and Applications. Journal of Applied Biomaterials 1991 Fal;2(3):187-208.

3. Kretlow JD, Young S, Klouda L, Wong M, Mikos AG. Injectable Biomaterials for Regenerating Complex Craniofacial Tissues. Advanced Materials 2009 Sep 4;21(32-33):3368-3393.

4. A. SETH GREENWALD, SCOTT D. BODEN, ROBERT L. BARRACK, MATHIAS P.G. BOSTROM, VICTOR M. GOLDBERG, MICHAEL J. YASZEMSKI, et al. THE EVOLVING ROLE OF BONE-GRAFT SUBSTITUTES. AMERICAN ACADEMY OF ORTHOPAEDIC SURGEONS; 2010; NEW ORLEANS, LOUISIANA; 2010.

5. Burg KJL, Porter S, Kellam JF. Biomaterial developments for bone tissue engineering. Biomaterials 2000 Dec;21(23):2347-2359.

6. Frohlich M, Grayson WL, Wan LQ, Marolt D, Drobnic M, Vunjak-Novakovic G. Tissue Engineered Bone Grafts: Biological Requirements, Tissue Culture and Clinical Relevance. Current Stem Cell Research & Therapy 2008 Dec;3(4):254-264.

7. Logeart-Avramoglou D, Anagnostou F, Bizios R, Petite H. Engineering bone: challenges and obstacles. Journal of Cellular and Molecular Medicine 2005 Jan-Mar;9(1):72-84.

8. Farhadi J, Jaquiery C, Haug M, Pierer G, Zeilhofer HF, Martin I. Bone and cartilage tissue engineering for facial reconstructive surgery. Ieee Engineering in Medicine and Biology Magazine 2006 Jan-Feb;25(1):106-109.

9. Stevens B, Yang YZ, MohandaS A, Stucker B, Nguyen KT. A review of materials, fabrication to enhance bone regeneration in methods, and strategies used engineered bone tissues. Journal of Biomedical Materials Research Part B-Applied Biomaterials 2008 May;85B(2):573-582.

10. Karageorgiou V, Kaplan D. Porosity of 3D biornaterial scaffolds and osteogenesis. Biomaterials 2005 Sep;26(27):5474-5491.

11. van Oers RFM, Ruimerman R, van Rietbergen B, Hilbers PAJ, Huiskes R. Relating osteon diameter to strain. Bone 2008 Sep;43(3):476-482.

12. Sarvestani AS, He X, Jabbari E. Osteonectin-derived peptide increases the modulus of a bone-mimetic nanocomposite. European Biophysics Journal with Biophysics Letters 2008 Feb;37(2):229-234.

13. Sarvestani AS, He XZ, Jabbari E. Effect of osteonectin-derived peptide on the viscoelasticity of hydrogel/apatite nanocomposite scaffolds. Biopolymers 2007 Mar;85(4):370-378.

14. Fujisawa R, Wada Y, Nodasaka Y, Kuboki Y. Acidic amino acid-rich sequences as binding sites of osteonectin to hydroxyapatite crystals. Biochimica Et Biophysica Acta-Protein Structure and Molecular Enzymology 1996 Jan 4;1292(1):53-60.

15. Fantner GE, Birkedal H, Kindt JH, Hassenkam T, Weaver JC, Cutroni JA, et al. Influence of the degradation of the organic matrix on the microscopic fracture behavior of trabecular bone. Bone 2004;35(5):1013-1022.

16. Beachley V, Wen XJ. Polymer nanofibrous structures: Fabrication, biofunctionalization, and cell interactions. Progress in Polymer Science 2010 Jul;35(7):868-892.

17. Xu CY, Inai R, Kotaki M, Ramakrishna S. Aligned biodegradable nanotibrous structure: a potential scaffold for blood vessel engineering. Biomaterials 2004 Feb;25(5):877-886.

18. Yoshimoto H, Shin YM, Terai H, Vacanti JP. A biodegradable nanofiber scaffold by electrospinning and its potential for bone tissue engineering. Biomaterials 2003 May;24(12):2077-2082.

19. Yu H-S, Jang J-H, Kim T-I, Lee H-H, Kim H-W. Apatite-mineralized polycaprolactone nanofibrous web as a bone tissue regeneration substrate. Journal of Biomedical Materials Research Part A 2009;88A(3):747-754.

20. Wei GB, Ma PX. Structure and properties of nano-hydroxyapatite/polymer composite scaffolds for bone tissue engineering. Biomaterials 2004 Aug;25(19):4749-4757.

21. Zhang Y, Zhang MQ. Three-dimensional macroporous calcium phosphate bioceramics with nested chitosan sponges for load-bearing bone implants. Journal of Biomedical Materials Research 2002 Jul;61(1):1-8.

22. Du C, Cui FZ, Zhang W, Feng QL, Zhu XD, de Groot K. Formation of calcium phosphate/collagen composites through mineralization of collagen matrix. Journal of Biomedical Materials Research 2000 Jun 15;50(4):518-527.

23. Martini FH. Fundamentals of Anatomy and Physiology. 4 ed. New Jersey: Prentice Hall, 1998.

24. tutorials As. AL's Web site, Departmant of Zoology, University of British Columbia. http://wwwzoologyubcca/~biomania/tutorial/bonets/anc01htm [cited 10/21/2009]; Available from:

25. Wiley J. http://www.cliffsnotes.com/WileyCDA/CliffsReviewTopic/topicArticleId-22032,articleId-21900.html. Cliff Notes [cited 21 Oct 2009; Available from:

26. Karaman O. A Novel Technique for Fabricating Aligned Nanofibers by Using Solution Electrospinning [Thesis and Dissertations]. Columbia: University of South Carolina; 2009.

27. Rod R. Seeley TDS, Philip Tate. anatomy&physiology. 5 ed. New York: McGraw-Hill, 2000.

28. Center BTE. Carnegie Mellon University http://www.btec.cmu.edu/reFramed/tutorial/mainLayoutTutorial.html. [cited 10/20/2009]; Available from:

29. Diana M. Yoon JPF. Polymeric Scaffolds for Tissue Engineering. In: John P. Fisher AGM, Joseph D.Bronzino, editor. Tissue Engineering: CRC Press, 2004.

30. Martin TA, Caliari SR, Williford PD, Harley BA, Bailey RC. The generation of biomolecular patterns in highly porous collagen-GAG scaffolds using direct photolithography. Biomaterials 2011 Jun;32(16):3949-3957.

31. Kakudo N, Shimotsuma A, Miyake S, Kushida S, Kusumoto K. Bone tissue engineering using human adipose-derived stem cells and honeycomb collagen scaffold. Journal of Biomedical Materials Research Part A 2008 Jan;84A(1):191-197.

32. Willerth SM, Sakiyama-Elbert SE. Approaches to neural tissue engineering using scaffolds for drug delivery. Advanced Drug Delivery Reviews 2007 May 30;59(4-5):325-338.

33. Radulescu D, Dhar S, Young CM, Taylor DW, Trost HJ, Hayes DJ, et al. Tissue engineering scaffolds for nerve regeneration manufactured by ink-jet technology. Materials Science & Engineering C-Biomimetic and Supramolecular Systems 2007 Apr;27(3):534-539.

34. Nair LS, Laurencin CT. Biodegradable polymers as biomaterials. Progress in Polymer Science 2007 Aug-Sep;32(8-9):762-798.

35. Kim MS, Kim JH, Min BH, Chun HJ, Han DK, Lee HB. Polymeric Scaffolds for Regenerative Medicine. Polymer Reviews 2011;51(1):23-52.

36. Cen L, Liu W, Cui L, Zhang WJ, Cao YL. Collagen tissue engineering: Development of novel biomaterials and applications. Pediatric Research 2008 May;63(5):492-496.

37. Lee CH, Singla A, Lee Y. Biomedical applications of collagen. International Journal of Pharmaceutics 2001 Jun 19;221(1-2):1-22.

38. Malafaya PB, Silva GA, Reis RL. Natural-origin polymers as carriers and scaffolds for biomolecules and cell delivery in tissue engineering applications. Advanced Drug Delivery Reviews 2007 May 30;59(4-5):207-233.

39. Yang CL, Hillas PJ, Baez JA, Nokelainen M, Balan J, Tang J, et al. The application of recombinant human collagen in tissue engineering. Biodrugs 2004;18(2):103-119.

40. Harley BA, Lynn AK, Wissner-Gross Z, Bonfield W, Yannas IV, Gibson LJ. Design of a multiphase osteochondral scaffold. II. Fabrication of a mineralized collagen-glycosaminoglycan scaffold. Journal of Biomedical Materials Research Part A 2010 Mar 1;92A(3):1066-1077.

41. Ciardelli G, Gentile P, Chiono V, Mattioli-Belmonte M, Vozzi G, Barbani N, et al. Enzymatically crosslinked porous composite matrices for bone tissue regeneration. Journal of Biomedical Materials Research Part A 2010 Jan;92A(1):137-151.

42. Dubey DK, Tomar V. Role of the nanoscale interfacial arrangement in mechanical strength of tropocollagen-hydroxyapatite-based hard biomaterials. Acta Biomaterialia 2009 Sep;5(7):2704-2716.

43. Xiao Y, Qian H, Young WG, Bartold PM. Tissue engineering for bone regeneration using differentiated alveolar bone cells in collagen scaffolds. Tissue Engineering 2003 Dec;9(6):1167-1177.

44. Chan BP, Hui TY, Wong MY, Yip KHK, Chan GCF. Mesenchymal Stem Cell-Encapsulated Collagen Microspheres for Bone Tissue Engineering. Tissue Engineering Part C-Methods 2010 Apr;16(2):225-235.

45. Venkatesan J, Kim SK. Chitosan Composites for Bone Tissue Engineering-An Overview. Marine Drugs 2010 Aug;8(8):2252-2266.

46. Di Martino A, Sittinger M, Risbud MV. Chitosan: A versatile biopolymer for orthopaedic tissue-engineering. Biomaterials 2005 Oct;26(30):5983-5990.

47. Hu QL, Li BQ, Wang M, Shen JC. Preparation and characterization of biodegradable chitosan/hydroxyapatite nanocomposite rods via in situ hybridization: A potential material as internal fixation of bone fracture. Biomaterials 2004 Feb;25(5):779-785.

48. Zhang Y, Venugopal JR, El-Turki A, Ramakrishna S, Su B, Lim CT. Electrospun biomimetic nanocomposite nanofibers of hydroxyapatite/chitosan for bone tissue engineering. Biomaterials 2008 Nov;29(32):4314-4322.

49. Teng SH, Lee EJ, Yoon BH, Shin DS, Kim HE, Oh JS. Chitosan/nanohydroxyapatite composite membranes via dynamic filtration for guided bone regeneration. Journal of Biomedical Materials Research Part A 2009 Mar 1;88A(3):569-580.

50. Thein-Han WW, Misra RDK. Biomimetic chitosan-nanohydroxyapatite composite scaffolds for bone tissue engineering. Acta Biomaterialia 2009 May;5(4):1182-1197.

51. Young S, Wong M, Tabata Y, Mikos AG. Gelatin as a delivery vehicle for the controlled release of bioactive molecules. Journal of Controlled Release 2005 Dec 5;109(1-3):256-274.

52. Tabata Y, Ikada Y. Protein release from gelatin matrices. Advanced Drug Delivery Reviews 1998 May 4;31(3):287-301.

53. Takahashi Y, Yamamoto M, Tabata Y. Osteogenic differentiation of mesenchymal stem cells in biodegradable sponges composed of gelatin and beta-tricalcium phosphate. Biomaterials 2005 Jun;26(17):3587-3596.

54. Xia Y, Mei F, Duan YL, Gao Y, Xiong Z, Zhang T, et al. Bone tissue engineering using bone marrow stromal cells and an injectable sodium alginate/gelatin scaffold. Journal of Biomedical Materials Research Part A 2012 Apr;100A(4):1044-1050.

55. He CL, Zhang F, Cao LJ, Feng W, Qiu KX, Zhang YZ, et al. Rapid mineralization of porous gelatin scaffolds by electrodeposition for bone tissue engineering. Journal of Materials Chemistry 2012;22(5):2111-2119.

56. Liu X, Smith LA, Hu J, Ma PX. Biomimetic nanofibrous gelatin/apatite composite scaffolds for bone tissue engineering. Biomaterials 2009 Apr;30(12):2252-2258.

57. Yamada K, Tabata Y, Yamamoto K, Miyamoto S, Nagata I, Kikuchi H, et al. Potential efficacy of basic fibroblast growth factor incorporated in biodegradable hydrogels for skull bone regeneration. Journal of Neurosurgery 1997 May;86(5):871-875.

58. Yamamoto M, Tabata Y, Hong L, Miyamoto S, Hashimoto N, Ikada Y. Bone regeneration by transforming growth factor beta 1 released from a biodegradable hydrogel. Journal of Controlled Release 2000 Feb 14;64(1-3):133-142.

59. Laurencin C, Khan Y, El-Amin SF. Bone graft substitutes. Expert Review of Medical Devices 2006 Jan;3(1):49-57.

60. Kricheldorf HR. Syntheses and application of polylactides. Chemosphere 2001 Apr;43(1):49-54.

61. Onose G, Ciurea AV, Rizea RE, Chendreanu C, Anghelescu A, Haras M, et al. Recent advancements in biomaterials for spinal cord injury complex therapeutics. Digest Journal of Nanomaterials and Biostructures 2007 Dec;2(4):307-314.

62. Liao SS, Cui FZ, Zhang W, Feng QL. Hierarchically biomimetic bone scaffold materials: Nano-HA/collagen/PLA composite. Journal of Biomedical Materials Research Part B-Applied Biomaterials 2004 May 15;69B(2):158-165.

63. Reed AM, Gilding DK. Biodegradable Polymers for Use in Surgery - Poly(Glycolic)-Poly(Lactic Acid) Homo and Co-Polymers .2. Invitro Degradation. Polymer 1981;22(4):494-498.

64. Lao LH, Wang YJ, Zhu Y, Zhang YY, Gao CY. Poly(lactide-co-glycolide)/hydroxyapatite nanofibrous scaffolds fabricated by electrospinning for bone tissue engineering. Journal of Materials Science-Materials in Medicine 2011 Aug;22(8):1873-1884.

65. Schnell E, Klinkhammer K, Balzer S, Brook G, Klee D, Dalton P, et al. Guidance of glial cell. migration and axonal growth on electrospun nanofibers of poly-epsilon-caprolactone and a collagen/poly-epsilon-caprolactone blend. Biomaterials 2007 Jul;28(19):3012-3025.

66. Shin M, Yoshimoto H, Vacanti JP. In vivo bone tissue engineering using mesenchymal stem cells on a novel electrospun nanofibrous scaffold. Tissue Engineering 2004 Jan-Feb;10(1-2):33-41.

67. Venugopal J, Vadgama P, Kumar TSS, Ramakrishna S. Biocomposite nanofibres and osteoblasts for bone tissue engineering. Nanotechnology 2007 Feb 7;18(5).

68. Salgado AJ, Coutinho OP, Reis RL. Bone tissue engineering: State of the art and future trends. Macromolecular Bioscience 2004 Aug 9;4(8):743-765.

69. Chen QZZ, Thompson ID, Boccaccini AR. 45S5 Bioglass (R)-derived glass-ceramic scaffolds for bone tissue engineering. Biomaterials 2006 Apr;27(11):2414-2425.

70. Ma PX. Biomimetic materials for tissue engineering. Advanced Drug Delivery Reviews 2008 Jan 14;60(2):184-198.

71. Elsdale T, Bard J. Collagen Substrata for Studies on Cell Behavior. Journal of Cell Biology 1972;54(3):626-&.

72. Hong YS, Legge RL, Zhang S, Chen P. Effect of amino acid sequence and pH on nanofiber formation of self-assembling peptides EAK16-II and EAK16-IV. Biomacromolecules 2003 Sep-Oct;4(5):1433-1442.

73. Ma PX, Zhang RY. Synthetic nano-scale fibrous extracellular matrix. Journal of Biomedical Materials Research 1999 Jul;46(1):60-72.

74. Xue YH, Wang HX, Yu DS, Feng LF, Dai LM, Wang XG, et al. Superhydrophobic electrospun POSS-PMMA copolymer fibres with highly ordered nanofibrillar and surface structures. Chemical Communications 2009(42):6418-6420.

75. Fang JA, Wang HX, Niu HT, Lin T, Wang XG. Evolution of Fiber Morphology During Electrospinning. Journal of Applied Polymer Science 2010 Dec 5;118(5):2553-2561.

76. Whitesides GM, Grzybowski B. Self-assembly at all scales. Science 2002 Mar 29;295(5564):2418-2421.

77. Silva GA, Czeisler C, Niece KL, Beniash E, Harrington DA, Kessler JA, et al. Selective differentiation of neural progenitor cells by high-epitope density nanofibers. Science 2004 Feb 27;303(5662):1352-1355.

78. Huang Z-M, Zhang YZ, Kotaki M, Ramakrishna S. A review on polymer nanofibers by electrospinning and their applications in nanocomposites. Composites Science and Technology 2003;63(15):2223-2253.

79. Shuguang Zhang FG, Xiaojun Zhaoc. Designer self-assembling peptide nanofiber scaffolds for 3D tissue cell cultures. Seminars in Cancer Biology 2005;15 (2005) 413–420.

80. Rajesh Vasita DSK. Nanofibers and their applications in tissue engineering. International Journal of Nanomedicine 2006;2006:1(1) 15–30.

81. Paul D. Dalton DK, Martin Moller. Electrospinning with dual collection rings. Polymer 2005;Vol. 46 (2005) 611-614.

82. Jie Yu YQ, Xiaoxiong Zha, Min Yu et al. Production of aligned polymer nanofibers by electrospinning. European Polymer Journal 2008;Vol. 44 (2008) 2838-2844.

83. Reneker JDaDH. Electrospinning Process and Applications of Electrospun Fibers. Journal of Electrostatics 1995;35 (1995) 151-160.

84. Chronakis IS. Novel nanocomposites and nanoceramics based on polymer nanofibers using electrospinning process. Journal of Material Processing Technology 2005;Vol. 167 (2005) 283-293.

85. Schauer JDSaCL. A Review: Electrospinning of Biopolymer Nanofibers and their Applications. Polymer Reviews 2008;Vol. 48(2008) 317-352.

86. Nasim Amiraliyan MN, Mohammad Haghighat Kish. Effects of Some Electrospinning Parameters on Morphology of Natural Silk-Based Nanofibers. Journal of Applied Polymer Sciences 2008;Vol. 113(2009) 226-234.

87. Li XR, Xie JW, Yuan XY, Xia YN. Coating Electrospun Poly(ε-caprolactone) Fibers with Gelatin and Calcium Phosphate and Their Use as Biomimetic Scaffolds for Bone Tissue Engineering. Langmuir 2008;24:14145-14150.

88. Whited BM, Whitney JR, Hofmann MC, Xu Y, Rylander MN. Pre-osteoblast infiltration and differentiation in highly porous apatite-coated PLLA electrospun scaffolds. Biomaterials 2011 Mar;32(9):2294-2304.

89. Zhang YZ, Reddy VJ, Wong SY, Li X, Su B, Ramakrishna S, et al. Enhanced Biomineralization in Osteoblasts on a Novel Electrospun Biocomposite Nanofibrous

Substrate of Hydroxyapatite/Collagen/Chitosan. Tissue Engineering Part A 2010 Jun;16(6):1949-1960.

90. Chua KN, Lim WS, Zhang PC, Lu HF, Wen J, Ramakrishna S, et al. Stable immobilization of rat hepatocyte spheroids on galactosylated nanofiber scaffold. Biomaterials 2005 May;26(15):2537-2547.

91. Schindler M, Ahmed I, Kamal J, Nur-E-Kamal A, Grafe TH, Chung HY, et al. A synthetic nanofibrillar matrix promotes in vivo-like organization and morphogenesis for cells in culture. Biomaterials 2005 Oct;26(28):5624-5631.

92. Kim HW, Lee HH, Knowles JC. Electrospinning biomedical nanocomposite fibers of hydroxyapaite/poly(lactic acid) for bone regeneration. Journal of Biomedical Materials Research Part A 2006 Dec 1;79A(3):643-649.

93. Ma JY, He XZ, Jabbari E. Osteogenic Differentiation of Marrow Stromal Cells on Random and Aligned Electrospun Poly(L-lactide) Nanofibers. Annals of Biomedical Engineering 2011 Jan;39(1):14-25.

94. Shin H, Jo S, Mikos AG. Biomimetic materials for tissue engineering. Biomaterials 2003 Nov;24(24):4353-4364.

95. Zhang JY, Beckman EJ, Piesco NP, Agarwal S. A new peptide-based urethane polymer: synthesis, biodegradation, and potential to support cell growth in vitro. Biomaterials 2000 Jun;21(12):1247-1258.

96. Wei Hea ZM, Thomas Yonga, Wee Eong Teoc, Seeram Ramakrishna. Fabrication of collagen-coated biodegradable polymer nanofiber mesh and its potential for endothelial cells growth. Biomaterials 2005;26 (2005) 7606–7615.

97. Cook AD, Hrkach JS, Gao NN, Johnson IM, Pajvani UB, Cannizzaro SM, et al. Characterization and development of RGD-peptide-modified poly(lactic acid-co-lysine) as an interactive, resorbable biomaterial. Journal of Biomedical Materials Research 1997 Jun 15;35(4):513-523.

98. Zhang RY, Ma PX. Poly(alpha-hydroxyl acids) hydroxyapatite porous composites for bone-tissue engineering. I. Preparation and morphology. Journal of Biomedical Materials Research 1999 Mar 15;44(4):446-455.

99. Hu YH, Winn SR, Krajbich I, Hollinger JO. Porous polymer scaffolds surface-modified with arginine-glycine-aspartic acid enhance bone cell attachment and differentiation in vitro. Journal of Biomedical Materials Research Part A 2003 Mar 1;64A(3):583-590.

100. He XZ, Ma JY, Jabbari E. Effect of Grafting RGD and BMP-2 Protein-Derived Peptides to a Hydrogel Substrate on Osteogenic Differentiation of Marrow Stromal Cells. Langmuir 2008 Nov 4;24(21):12508-12516.

101. Ma PX, Zhang RY, Xiao GZ, Franceschi R. Engineering new bone tissue in vitro on highly porous poly(alpha-hydroxyl acids)/hydroxyapatite composite scaffolds. Journal of Biomedical Materials Research 2001 Feb;54(2):284-293.

102. Marra KG, Szem JW, Kumta PN, DiMilla PA, Weiss LE. In vitro analysis of biodegradable polymer blend/hydroxyapatite composites for bone tissue engineering. Journal of Biomedical Materials Research 1999 Dec 5;47(3):324-335.

103. Thomson RC, Yaszemski MJ, Powers JM, Mikos AG. Hydroxyapatite fiber reinforced poly(alpha-hydroxy ester) foams for bone regeneration. Biomaterials 1998 Nov;19(21):1935-1943.

104. Muller L, Muller FA. Preparation of SBF with different HCO3- content and its influence on the composition of biomimetic apatites. Acta Biomaterialia 2006 Mar;2(2):181-189.

105. Kokubo T, Takadama H. How useful is SBF in predicting in vivo bone bioactivity? Biomaterials 2006 May;27(15):2907-2915.

106. Liu WY, Yeh YC, Lipner J, Xie JW, Sung HW, Thomopoulos S, et al. Enhancing the Stiffness of Electrospun Nanofiber Scaffolds with a Controlled Surface Coating and Mineralization. Langmuir 2011 Aug 2;27(15):9088-9093.

107. Cowan CM, Shi YY, Aalami OO, Chou YF, Mari C, Thomas R, et al. Adipose-derived adult stromal cells heal critical-size mouse calvarial defects. Nature Biotechnology 2004 May;22(5):560-567.

108. Alves NM, Leonor IB, Azevedo HS, Reis RL, Mano JF. Designing biomaterials based on biomineralization of bone. Journal of Materials Chemistry 2010;20(15):2911-2921.

109. Cai Q, Xu QQ, Feng QF, Cao XY, Yang XP, Deng XL. Biomineralization of electrospun poly(L-lactic acid)/gelatin composite fibrous scaffold by using a supersaturated simulated body fluid with continuous CO2 bubbling. Applied Surface Science 2011 Sep 15;257(23):10109-10118.

110. Kim HM, Miyaji F, Kokubo T, Nakamura T. Preparation of bioactive Ti and its alloys via simple chemical surface treatment. Journal of Biomedical Materials Research 1996 Nov;32(3):409-417.

111. Ngiam M, Liao SS, Patil AJ, Cheng ZY, Chan CK, Ramakrishna S. The fabrication of nano-hydroxyapatite on PLGA and PLGA/collagen nanofibrous composite scaffolds and their effects in osteoblastic behavior for bone tissue engineering. Bone 2009 Jul;45(1):4-16.

112. Murphy WL, Mooney DJ. Bioinspired growth of crystalline carbonate apatite on biodegradable polymer substrata. Journal of the American Chemical Society 2002 Mar 6;124(9):1910-1917.

113. Mooney JF. Disorders of bone and mineral metabolism. Arthroscopy: The Journal of Arthroscopic and Related Surgery 1992;8(3):415.

114. Athanasiou KA, Zhu CF, Lanctot DR, Agrawal CM, Wang X. Fundamentals of biomechanics in tissue engineering of bone. Tissue Engineering 2000 Aug;6(4):361-381.

115. Beachley V, Wen X. Polymer nanofibrous structures: Fabrication, biofunctionalization, and cell interactions. Progress in Polymer Science 2010;35(7):868-892.

116. Chen J-P, Chang Y-S. Preparation and characterization of composite nanofibers of polycaprolactone and nanohydroxyapatite for osteogenic differentiation of mesenchymal stem cells. Colloids and Surfaces B: Biointerfaces 2011;86(1):169-175.

117. Cai Q, Xu QQ, Feng QF, Cao XY, Yang XP, Deng XL. Biomineralization of electrospun poly(L-lactic acid)/gelatin composite fibrous scaffold by using a supersaturated simulated body fluid with continuous CO(2) bubbling. Applied Surface Science 2011 Sep 15;257(23):10109-10118.

118. Li CM, Vepari C, Jin HJ, Kim HJ, Kaplan DL. Electrospun silk-BMP-2 scaffolds for bone tissue engineering. Biomaterials 2006 Jun;27(16):3115-3124.

119. Thomas V, Dean DR, Jose MV, Mathew B, Chowdhury S, Vohra YK. Nanostructured biocomposite scaffolds based on collagen coelectrospun with nanohydroxyapatite. Biomacromolecules 2007 Feb;8(2):631-637.

120. Bao CY, Chen WC, Weir MD, Thein-Han W, Xu HHK. Effects of electrospun submicron fibers in calcium phosphate cement scaffold on mechanical properties and osteogenic differentiation of umbilical cord stem cells. Acta Biomaterialia 2011 Nov;7(11):4037-4044.

121. Yuan XY, Mak AFT, Li JL. Formation of bone-like apatite on poly(L-lactic acid) fibers by a biomimetic process. Journal of Biomedical Materials Research 2001 Oct;57(1):140-150.

122. Chen JL, Chu B, Hsiao BS. Mineralization of hydroxyapatite in electrospun nanofibrous poly(L-lactic acid) scaffolds. Journal of Biomedical Materials Research Part A 2006 Nov;79A(2):307-317.

123. Mavis B, Demirtas TT, Gumusderelioglu M, Gunduz G, Colak U. Synthesis, characterization and osteoblastic activity of polycaprolactone nanofibers coated with biomimetic calcium phosphate. Acta Biomaterialia 2009 Oct;5(8):3098-3111.

124. Wang Q, Wang XM, Tian LL, Cheng ZJ, Cui FZ. In situ remineralizaiton of partially demineralized human dentine mediated by a biomimetic non-collagen peptide. Soft Matter 2011;7(20):9673-9680.

125. Jabbari E, He XZ, Valarmathi MT, Sarvestani AS, Xu WJ. Material properties and bone marrow stromal cells response to in situ crosslinkable RGD-functionlized lactide-co-glycolide scaffolds. Journal of Biomedical Materials Research Part A 2009 Apr;89A(1):124-137.

126. He XZ, Jabbari E. Solid-phase synthesis of reactive peptide crosslinker by selective deprotection. Protein and Peptide Letters 2006;13(7):715-718.

127. He X, Ma J, Jabbari E. Effect of Grafting RGD and BMP-2 Protein-Derived Peptides to a Hydrogel Substrate on Osteogenic Differentiation of Marrow Stromal Cells. Langmuir 2008 Nov 4;24(21):12508-12516.

128. Kaiser E, Colescott RL, Bossinger CD, Cook PI. Color Test for Detection of Free Terminal Amino Groups in Solid-Phase Synthesis of Peptides. Analytical Biochemistry 1970;34(2):595-&.

129. Jabbari E, He XZ. Synthesis and characterization of bioresorbable in situ crosslinkable ultra low molecular weight poly(lactide) macromer. Journal of Materials Science-Materials in Medicine 2008 Jan;19(1):311-318.

130. Yang F, Murugan R, Wang S, Ramakrishna S. Electrospinning of nano/micro scale poly(L-lactic acid) aligned fibers and their potential in neural tissue engineering. Biomaterials 2005 May;26(15):2603-2610.

131. Walboomers XF, Croes HJE, Ginsel LA, Jansen JA. Contact guidance of rat fibroblasts on various implant materials. Journal of Biomedical Materials Research 1999;47(2):204-212.

132. He XZ, Jabbari E. Material properties and cytocompatibility of injectable MMP degradable poly(lactide ethylene oxide fumarate) hydrogel as a carrier for marrow stromal cells. Biomacromolecules 2007 Mar;8(3):780-792.

133. Shin US, Park JH, Hong SJ, Won JE, Yu HS, Kim HW. Porous biomedical composite microspheres developed for cell delivering scaffold in bone regeneration. Materials Letters 2010 Oct 31;64(20):2261-2264.

134. He X, Yang X, Jabbari E. Combined effect of osteopontin and BMP-2 derived peptides grafted to an adhesive hydrogel on osteogenic and vasculogenic differentiation of marrow stromal cells. Langmuir 2012;28(12):5387-5397.

135. Henderson JA, He XZ, Jabbari E. Concurrent differentiation of marrow stromal cells to osteogenic and vasculogenic lineages. Macromolecular Bioscience 2008 Jun 11;8(6):499-507.

136. Selvarnurugan N, Kwok S, Vasilov A, Jefcoat SC, Partridge NC. Effects of BMP-2 and pulsed electromagnetic field (PEMF) on rat primary osteoblastic cell proliferation and gene expression. Journal of Orthopaedic Research 2007 Sep;25(9):1213-1220.

137. Ciarmela P, Wiater E, Smith SM, Vale W. Presence, Actions, and Regulation of Myostatin in Rat Uterus and Myometrial Cells. Endocrinology 2009 Feb;150(2):906-914.

138. Schefe JH, Lehmann KE, Buschmann IR, Unger T, Funke-Kaiser H. Quantitative real-time RT-PCR data analysis: current concepts and the novel "gene expression's CT difference" formula. J Mol Med (Berl) 2006 Nov;84(11):901-910.

139. Livak KJ, Schmittgen TD. Analysis of relative gene expression data using real-time quantitative PCR and the 2(-Delta Delta C(T)) Method. Methods 2001 Dec;25(4):402-408.

140. Moeinzadeh S, Jabbari E. Mesoscale Simulation of the Effect of a Lactide Segment on the Nanostructure of Star Poly(ethylene glycol-co-lactide)-Acrylate Macromonomers in Aqueous Solution. Journal of Physical Chemistry B 2012 Feb 9;116(5):1536-1543.

141. Moeinzadeh S, Barati D, He XZ, Jabbari E. Gelation Characteristics and Osteogenic Differentiation of Stromal Cells in Inert Hydrolytically Degradable Micellar Polyethylene Glycol Hydrogels. Biomacromolecules 2012 Jul;13(7):2073-2086.

142. Hoogerbrugge PJ, Koelman JMVA. Simulating Microscopic Hydrodynamic Phenomena with Dissipative Particle Dynamics. Europhysics Letters 1992 Jun 1;19(3):155-160.

143. Espanol P, Warren P. Statistical-Mechanics of Dissipative Particle Dynamics. Europhysics Letters 1995 May 1;30(4):191-196.

144. Groot RD, Warren PB. Dissipative particle dynamics: Bridging the gap between atomistic and mesoscopic simulation. Journal of Chemical Physics 1997 Sep 15;107(11):4423-4435.

145. Sun H. COMPASS: An ab initio force-field optimized for condensed-phase applications - Overview with details on alkane and benzene compounds. Journal of Physical Chemistry B 1998 Sep 17;102(38):7338-7364.

146. Yang F, Wolke JGC, Jansen JA. Biomimetic calcium phosphate coating on electrospun poly (epsilon-caprolactone) scaffolds for bone tissue engineering. Chemical Engineering Journal 2008 Mar 15;137(1):154-161.

147. Ito Y, Hasuda H, Kamitakahara M, Ohtsuki C, Tanihara M, Kang IK, et al. A composite of hydroxyapatite with electrospun biodegradable nanofibers as a tissue engineering material. Journal of Bioscience and Bioengineering 2005 Jul;100(1):43-49.

148. Takeuchi A, Ohtsuki C, Miyazaki T, Tanaka H, Yamazaki M, Tanihara M. Deposition of bone-like apatite on silk fiber in a solution that mimics extracellular fluid. Journal of Biomedical Materials Research Part A 2003;65A(2):283-289.

149. Thomas V, Jagani S, Johnson K, Jose MV, Dean DR, Vohra YK, et al. Electrospun Bioactive Nanocomposite Scaffolds of Polycaprolactone and Nanohydroxyapatite for

Bone Tissue Engineering. Journal of Nanoscience and Nanotechnology 2006;6(2):487-493.

150. Kim HW, Song JH, Kim HE. Nanofiber Generation of Gelatin–Hydroxyapatite Biomimetics for Guided Tissue Regeneration. Advanced Functional Materials 2005;15(12):1988-1994.

151. Jaiswal N, Haynesworth SE, Caplan AI, Bruder SP. Osteogenic differentiation of purified, culture-expanded human mesenchymal stem cells in vitro. Journal of Cellular Biochemistry 1997;64(2):295-312.

152. Choi J-Y, Lee B-H, Song K-B, Park R-W, Kim I-S, Sohn K-Y, et al. Expression patterns of bone-related proteins during osteoblastic differentiation in MC3T3-E1 cells. Journal of Cellular Biochemistry 1996;61(4):609-618.

153. Gentsch R, Pippig F, Schmidt S, Cernoch P, Polleux J, Borner HG. Single-Step Electrospinning to Bioactive Polymer Nanofibers. Macromolecules 2011 Feb 8;44(3):453-461.

154. Sun XY, Nobles LR, Borner HG, Spontak RJ. Field-driven surface segregation of biofunctional species on electrospun PMMA/PEO microfibers. Macromolecular Rapid Communications 2008 Sep 1;29(17):1455-1460.

155. Urist MR. Fundamental and clinical bone physiology. 1st ed. Philadelphia: Lippincott Williams & Wilkins, 1980.

156. Li BH, Aspden RM. Composition and mechanical properties of cancellous bone from the femoral head of patients with osteoporosis or osteoarthritis. Journal of Bone and Mineral Research 1997 Apr;12(4):641-651.

157. Podsiadlo P, Qin M, Cuddihy M, Zhu J, Critchley K, Kheng E, et al. Highly Ductile Multilayered Films by Layer-by-Layer Assembly of Oppositely Charged Polyurethanes for Biomedical Applications. Langmuir 2009 Dec 15;25(24):14093-14099.

158. Podsiadlo P, Kaushik AK, Arruda EM, Waas AM, Shim BS, Xu JD, et al. Ultrastrong and stiff layered polymer nanocomposites. Science 2007 Oct 5;318(5847):80-83.

159. Li XR, Xie JW, Lipner J, Yuan XY, Thomopoulos S, Xia YN. Nanofiber Scaffolds with Gradations in Mineral Content for Mimicking the Tendon-to-Bone Insertion Site. Nano Lett 2009;9(7):2763-2768.

160. Kim K, Dean D, Mikos AG, Fisher JP. Effect of Initial Cell Seeding Density on Early Osteogenic Signal Expression of Rat Bone Marrow Stromal Cells Cultured on Cross-Linked Poly(propylene fumarate) Disks. Biomacromolecules 2009 Jul;10(7):1810-1817.

161. Zhou HZ, Weir MD, Xu HHK. Effect of Cell Seeding Density on Proliferation and Osteodifferentiation of Umbilical Cord Stem Cells on Calcium Phosphate Cement-Fiber Scaffold. Tissue Engineering Part A 2011 Nov;17(21-22):2603-2613.

162. Engler AJ, Sen S, Sweeney HL, Discher DE. Matrix elasticity directs stem cell lineage specification. Cell 2006 Aug 25;126(4):677-689.

163. Barradas AM, Yuan H, van Blitterswijk CA, Habibovic P. Osteoinductive biomaterials: current knowledge of properties, experimental models and biological mechanisms. Eur Cell Mater 2011;21:407-429; discussion 429.

164. Chatterjee K, Lin-Gibson S, Wallace WE, Parekh SH, Lee YJ, Cicerone MT, et al. The effect of 3D hydrogel scaffold modulus on osteoblast differentiation and mineralization revealed by combinatorial screening. Biomaterials 2010 Jul;31(19):5051-5062.

165. Engler AJ, Sen S, Sweeney HL, Discher DE. Matrix elasticity directs stem cell lineage specification. Cell 2006 Aug 25;126(4):677-689.

166. Lee JH, Rim NG, Jung HS, Shin H. Control of Osteogenic Differentiation and Mineralization of Human Mesenchymal Stem Cells on Composite Nanofibers Containing Poly [lactic-co-(glycolic acid)] and Hydroxyapatite. Macromolecular Bioscience 2010 Feb 11;10(2):173-182.

167. Wutticharoenmongkol P, Pavasant P, Supaphol P. Osteoblastic phenotype expression of MC3T3-E1 cultured on electrospun polycaprolactone fiber mats filled with hydroxyapatite nanoparticles. Biomacromolecules 2007 Aug;8(8):2602-2610.

168. Bhumiratana S, Grayson WL, Castaneda A, Rockwood DN, Gil ES, Kaplan DL, et al. Nucleation and growth of mineralized bone matrix on silk-hydroxyapatite composite scaffolds. Biomaterials 2011 Apr;32(11):2812-2820.

169. Damien CJ, Parsons JR. Bone graft and bone graft substitutes: A review of current technology and applications. Journal of Applied Biomaterials 1991;2(3):187-208.

170. Pham Q, Sharma U, Mikos AG. Electrospinning of polymeric nanofibers for tissue engineering applications: a review. Tissue Eng 2006;12(5):1197-1211.

171. Cai Q, Xu Q, Feng Q, Cao X, Yang X, Deng X. Biomineralization of electrospun poly(l-lactic acid)/gelatin composite fibrous scaffold by using a supersaturated simulated body fluid with continuous CO2 bubbling. Applied Surface Science 2011;257(23):10109-10118.

172. Huang ZM, Zhang YZ, Kotaki M, Ramakrishna S. A review on polymer nanofibers by electrospinning and their applications in nanocomposites. Composites Science and Technology 2003 Nov;63(15):2223-2253.

173. Sarvestani A, He X, Jabbari E. Osteonectin-derived peptide increases the modulus of a bone-mimetic nanocomposite. European Biophysics Journal 2008;37(2):229-234.

174. Even-Ram S, Yamada KM. Cell migration in 3D matrix. Current Opinion in Cell Biology 2005 Oct;17(5):524-532.

175. Bartold PM, McCulloch CAG, Narayanan AS, Pitaru S. Tissue engineering: a new paradigm for periodontal regeneration based on molecular and cell biology. Periodontology 2000 2000;24:253-269.

176. He X, Jabbari E. Material Properties and Cytocompatibility of Injectable MMP Degradable Poly(lactide ethylene oxide fumarate) Hydrogel as a Carrier for Marrow Stromal Cells. Biomacromolecules 2007 2007/03/01;8(3):780-792.

177. Holzwarth JM, Ma PX. 3D nanofibrous scaffolds for tissue engineering. Journal of Materials Chemistry 2011;21(28):10243-10251.

178. Yang F, Wolke JGC, Jansen JA. Biomimetic calcium phosphate coating on electrospun poly(…ð-caprolactone) scaffolds for bone tissue engineering. Chemical Engineering Journal 2008;137(1):154-161.

179. Smith LA, Liu XH, Hu J, Wang P, Ma PX. Enhancing Osteogenic Differentiation of Mouse Embryonic Stem Cells by Nanofibers. Tissue Engineering Part A 2009 Jul;15(7):1855-1864.

180. Hu J, Liu XH, Ma PX. Induction of osteoblast differentiation phenotype on poly(L-lactic acid) nanofibrous matrix. Biomaterials 2008 Oct;29(28):3815-3821.

181. Bolander ME, Young MF, Fisher LW, Yamada Y, Termine JD. Osteonectin Cdna Sequence Reveals Potential Binding Regions for Calcium and Hydroxyapatite and Shows Homologies with Both a Basement-Membrane Protein (Sparc) and a Serine Proteinase-Inhibitor (Ovomucoid). Proceedings of the National Academy of Sciences of the United States of America 1988 May;85(9):2919-2923.

182. Oldberg A, Franzen A, Heinegard D. The Primary Structure of a Cell-Binding Bone Sialoprotein. Journal of Biological Chemistry 1988 Dec 25;263(36):19430-19432.

183. Itoh D, Yoneda S, Kuroda S, Kondo H, Umezawa A, Ohya K, et al. Enhancement of osteogenesis on hydroxyapatite surface coated with synthetic peptide (EEEEEEEPRGDT) in vitro. Journal of Biomedical Materials Research 2002 Nov;62(2):292-298.

184. Schulz A. Bone-Structure and Remodeling Dynamics in Osteopathies. Zeitschrift Fur Rheumatologie 1988 Jul-Aug;47(4):309-310.

185. Liu W, Yeh Y-C, Lipner J, Xie J, Sung H-W, Thomopoulos S, et al. Enhancing the Stiffness of Electrospun Nanofiber Scaffolds with a Controlled Surface Coating and Mineralization. Langmuir 2011 2011/08/02;27(15):9088-9093.

186. Li X, Xie J, Lipner J, Yuan X, Thomopoulos S, Xia Y. Nanofiber Scaffolds with Gradations in Mineral Content for Mimicking the Tendon-to-Bone Insertion Site. Nano Letters 2009 2012/11/09;9(7):2763-2768.

187. Gustafsson Y, Haag J, Jungebluth P, Lundin V, Lim ML, Baiguera S, et al. Viability and proliferation of rat MSCs on adhesion protein-modified PET and PU scaffolds. Biomaterials 2012 Nov;33(32):8094-8103.

188. Valarmathi MT, Davis JM, Yost MJ, Goodwin RL, Potts JD. A three-dimensional model of vasculogenesis. Biomaterials 2009 Feb;30(6):1098-1112.

189. Marolt D, Augst A, Freed LE, Vepari C, Fajardo R, Patel N, et al. Bone and cartilage tissue constructs grown using human bone marrow stromal cells, silk scaffolds and rotating bioreactors. Biomaterials 2006 Dec;27(36):6138-6149.

190. Wutticharoenmongkol P, Sanchavanakit N, Pavasant P, Supaphol P. Preparation and characterization of novel bone scaffolds based on electrospun polycaprolactone fibers filled with nanoparticles. Macromolecular Bioscience 2006 Jan 5;6(1):70-77.

191. Choi JY, Lee BH, Song KB, Park RW, Kim IS, Sohn KY, et al. Expression patterns of bone-related proteins during osteoblastic differentiation in MC3T3-E1 cells. Journal of Cellular Biochemistry 1996 Jun 15;61(4):609-618.

192. Garvin KA, Dalecki D, Hocking DC. Vascularization of Three-Dimensional Collagen Hydrogels Using Ultrasound Standing Wave Fields. Ultrasound in Medicine & Biology;37(11):1853-1864.

193. Sun JX, Wang YL, Qian ZY, Hu CB. An approach to architecture 3D scaffold with interconnective microchannel networks inducing angiogenesis for tissue engineering. Journal of Materials Science-Materials in Medicine 2011 Nov;22(11):2565-2571.

194. Rozen N, Bick T, Bajayo A, Shamian B, Schrift-Tzadok M, Gabet Y, et al. Transplanted blood-derived endothelial progenitor cells (EPC) enhance bridging of sheep tibia critical size defects. Bone 2009;45(5):918-924.

195. Seebach C, Henrich D, Kahling C, Wilhelm K, Tami AE, Alini M, et al. Endothelial Progenitor Cells and Mesenchymal Stem Cells Seeded onto beta-TCP Granules Enhance Early Vascularization and Bone Healing in a Critical-Sized Bone Defect in Rats. Tissue Engineering Part A 2010 Jun;16(6):1961-1970.

196. Rouwkema J, Westerweel PE, de Boer J, Verhaar MC, van Blitterswijk CA. The Use of Endothelial Progenitor Cells for Prevascularized Bone Tissue Engineering. Tissue Engineering Part A 2009 Aug;15(8):2015-2027.

197. Wang DS, Miura M, Demura H, Sato K. Anabolic effects of 1,25-dihydroxyvitamin D-3 on osteoblasts are enhanced by vascular endothelial growth factor produced by osteoblasts and by growth factors produced by endothelial cells. Endocrinology 1997 Jul;138(7):2953-2962.

198. Pfaffl MW. A new mathematical model for relative quantification in real-time RT-PCR. Nucleic acids research 2001;29(9):e45.

199. Muller PY, Janovjak H, Miserez AR, Dobbie Z. Processing of gene expression data generated by quantitative real-time RT PCR (vol 32, pg 1378, 2002). Biotechniques 2002 Sep;33(3):514-514.

200. Xu CY, Inai R, Kotaki M, Ramakrishna S. Aligned biodegradable nanofibrous structure: a potential scaffold for blood vessel engineering. Biomaterials 2004;25(5):877-886.

201. Albelda SM, Muller WA, Buck CA, Newman PJ. Molecular and Cellular Properties of Pecam-1 (Endocam/Cd31) - a Novel Vascular Cell Cell-Adhesion Molecule. Journal of Cell Biology 1991 Sep;114(5):1059-1068.

202. Bautch VL, Redick SD, Scalia A, Harmaty M, Carmeliet P, Rapoport R. Characterization of the vasculogenic block in the absence of vascular endothelial growth factor-A. Blood 2000 Mar 15;95(6):1979-1987.

203. Sadler JE. Biochemistry and genetics of von Willebrand factor. Annual Review of Biochemistry 1998;67:395-424.